2022

Monitoring of State Transitions in Extreme Environment Application Materials Using Fiber Bragg Grating Sensors

Sabuj Khadka

Monitoring of State Transitions in Extreme Environment Application Materials Using Fiber Bragg Grating Sensors

_____

A

Dissertation

Presented to

the Faculty of the Daniel Felix Ritchie School of Engineering and Computer Science

University of Denver

_____

In Partial Fulfillment

of the Requirements for the Degree

Doctor of Philosophy

_____

by

Sabuj Khadka

March 2022

Advisor: Dr. Maciej Kumosa

Author: Sabuj Khadka
Title: Monitoring of State Transitions in Extreme Environment Application Materials Using Fiber Bragg Grating Sensors
Advisor: Dr. Maciej Kumosa
Degree Date: March 2022

Abstract

By embedding both a single fiber Bragg grating (FBG) sensor and a thermocouple (TC) during the manufacturing for extreme environment applications of certain classes of materials such as metals and polymers, a novel in-situ approach was developed to precisely monitor their entire manufacturing processes. This novel monitoring technique was able to identify many characteristic points during the curing of room and high-temperature epoxies and the solidification processes of metal alloys composed of tin and bismuth which were selected in this research purely for verification purposes. Some of the characteristic points identified for the epoxies were: (i) the gel point, (ii) the start of cure, (iii) the end of cure, (iv) the end of the manufacturing cycle, etc. For the tin/bismuth alloys, the technique was used for the first time to (i) identify the beginning and end of solidification and (ii) to construct the phase diagram of the alloys. It was demonstrated that the FBG sensor-based technique is better suited than the existing TC-based technique to detect the phase transitions of the alloys. The solidification process of water was also monitored and compared to the solidification process of the metals. The water solidification research was subsequently extended to simulate ice formation on transmission line conductors and to determine if the newly proposed FBG/TC method could be used as an ice monitoring method in service.

A novel heat balance approach was presented to identify the degree of cure for the epoxies and to estimate the end of solidification in the alloys. The heat balance approach was verified using the Flory-Stockmayer theory for identifying the gel point in polymers. By using the FBG measurements and a combination of linear elastic models, a novel, yet straightforward approach was presented to determine the residual stresses in a single fiber/polymer composite. Further, multiple factors that impact the calculation of axial strain evolution using fiber Bragg grating (FBG) sensors were thoroughly investigated and verified by analyzing the cooling of the epoxies, the tin/bismuth alloys, and ice.

The proposed monitoring technique could significantly improve the current capability to (i) measure the degree of cure of polymers, (ii) determine the residual strains and stresses in single fiber composites with polymer and metal matrices, (iii) assess the strain evolution during the solidification of metals, (iv) recreate the phase diagrams of metal alloys, (v) estimate stresses in solidified metal parts, (vi) monitor icing and deicing on transmission lines, and many others. Since the specimen preparation is straightforward, the proposed method can be routinely practiced, and the measurements can be completely automated. The techniques could provide a much-needed tool for rapid but accurate assessment of materials for extreme environment applications.

Acknowledgments

I would like to express sincere gratitude to my Ph.D. advisor, Professor Maciej Kumosa for supporting me during these past five plus years. I am very grateful to him for his scientific advice and knowledge and many insightful discussions and suggestions.

I also would like to acknowledge Dr. Joseph Hoffman for his ongoing collaborations that resulted in five joint international publications, and one submitted paper that form the basis for this dissertation. His scientific and mathematical intuition was critical in establishing many of the techniques developed in this research.

I am very thankful to Professor Emeritus Paul Predecki. He has provided support and constructive criticisms numerous times during my graduate school career. I would also like to thank the members of my Ph.D. committee, Professors Yun Bo Yi, Ali Azadani, and Iwona Jasiuk for their extensive professional and personal suggestions. I extend my sincere thanks to Dr. Paul Horn for chairing the defense committee and for facilitating the examination process.

I also thank my friends (too many to list here but you know who you are!) for providing the support and friendship that I needed. I am grateful to all of those with whom I have had the pleasure of working together on the projects. Nobody has been more important to me in the pursuit of this degree than the members of my family. I would like to thank my parents, and brother, whose love and guidance are with me in whatever I pursue. They are my ultimate role models, and I would not have made it this far without them.

Table of Contents

List of Figures

List of Tables

Monitoring of State Transitions in Extreme Environment Application Materials Using Fiber Bragg Grating Sensors

1.0 Introduction

Extreme environments can involve temperature and heat flux extremes, extreme chemical environments, large and complex stress/strain fields, corrosive environments, large radiation fluxes, and especially combinations or other complex interactions of these extremes. Under extreme conditions, materials can behave in unexpected and unpredictable ways. Understanding the effect of extreme environments on material behavior is critical to assuring the safety and reliability of materials.

Monitoring the manufacturing of materials for extreme applications is important because it can provide valuable information regarding their lifetime, reliability, and performance specifications. A challenge of monitoring materials for extreme environments is the complexity associated with their manufacturing processes. Polymers such as epoxies, metal alloys, and ice are considered extreme environment application materials because of complex and unpredictable reactions, phase changes, and extreme temperatures (very high or very low) involved during manufacturing and under in-service conditions. These materials could be under extreme environments either because of the naturally inherent complexities associated with the manufacturing process or through externally subjected loads. Either way, upon exposure to extreme environmental conditions, these materials may undergo a change in microstructure, physical state, mechanical and thermal properties,

chemical properties, etc. The relationships between these variables and materials properties that dictate performance are not always well understood or easy to elucidate.

It is difficult to independently control various aspects of curing characteristics in epoxies, solidification of alloys, crystallization of ice, and the mechanisms that determine microstructural changes in these materials. Moreover, the physical state evolution during manufacturing of an extreme environment application material is also often difficult to model. Existing techniques to monitor the materials and structures in extreme environments can be painstaking, often requiring specialized apparatus and long time periods. In addition, there are often numerous variables that may contribute to a particular property of interest, including test conditions, initial composition, rate of reaction, cooling rates, and material microstructure and/or processing. Many of these variables are difficult to control independently, and characterization and quantification may be challenging as well, especially for microstructural variables. However, designing a monitoring technique for extreme environment application materials is required to expand the capabilities of technologies ranging from nuclear reactors to high voltage transmission lines to many others.

Further, the capability to monitor the manufacturing process of materials can significantly enhance the understanding of the manufacturing process, improve the mold/die design, help reduce residual stresses, and produce a better product/part. In situ monitoring during manufacturing of various materials is important as it provides valuable information such as the curing state in polymers [1], [2], [3] phase changes in alloys [4], strains/stresses in metals [5], [6], [7], [8], [9], [10] ice accumulation/thickness in

transmission lines, etc. Fiber Bragg grating (FBG) sensor-based techniques can provide this information as the sensors can be embedded inside of the materials without significantly influencing their physical properties [1], [2], [3], [4], [5].

In this dissertation, a novel FBG sensor-based method is presented for monitoring the manufacturing of several purposely chosen materials, namely room temperature (RT) and higher temperature (HT) epoxies, tin/bismuth alloys, and crystallization of ice. A thorough analysis of the factors that need to be considered in converting wavelength readings to strain measurements in various types of materials was conducted. To show how differing mechanical properties of the matrix and geometric properties of the FBG fibers and samples can impact the FBG readings, the materials presented include two epoxies, seven tin/bismuth alloys, and ice (water). The information obtained from the embedded FBG fiber in the matrices was analyzed to characterize the various characteristic points associated with the curing in epoxies, solidification in the alloys, and crystallization in the ice. Further, the strain and stress fields of the matrices are also determined.

2.0 Fiber Bragg Gratings Sensor

2.1 Background/Principle

This section provides a brief introduction to FBG sensors. An FBG sensor is an optical sensor that consists of a fiber core with gratings produced by laterally exposing the core of single-mode fiber to a periodic pattern of intense laser energy [11], [12]. A glass cladding and a protective coating are added to the fiber core to facilitate the total internal reflection of light and to protect the fiber, respectively. The protective coating can be made of acrylate, polyimide, or other materials, depending on the application of interest. FBGs work on the principle of Bragg's law [13], [11] which was proposed by Lawrence Bragg and his father William Lawrence Bragg in 1913. At each grating, a specific wavelength of light is reflected that satisfies the Bragg condition [14]. The reflected Bragg wavelength depends on the thermal as well as the mechanical loads, and a review of the reflected wavelength can identify the stress/strain state of the material. The Bragg condition is given as [14], [15]:

$$\lambda = 2\eta_{eff}\Lambda \tag{1}$$

where λ is the Bragg wavelength, η_{eff} is the effective refractive index of light in the fiber, and Λ is the grating period.

In the early stages of FBG development, FBGs were produced by two main processes: interference and masking. Both processes involve 'inscribing' a variation of refractive index into the core of an optical fiber using an ultraviolet laser. Lately, many more FBG

fabrication processes have been developed such as sequential writing, point by point, continuous core scanning, etc. [16]. The method that is preferable depends on the type of grating to be manufactured. Mostly, the germanium doped silica fibers are preferred for the fiber core as they are photosensitive and the refractive index of the core changes with exposure to UV light. However, depending on the application requirements, polymer-based fibers can also be used.

The interference based FBG manufacturing technique involves exposing the photosensitive fiber to an interference fringe pattern in UV light. The exposure creates changes in the refractive index along the fiber. The refractive index change depends on the intensity of the UV light to which the fiber was exposed. Similarly, a grating in the optical fiber can be created by placing a photomask between the photosensitive fiber and the UV light source. In this technique, the shadow of the photomask determines the grating structure based on the transmitted intensity of light striking the fiber. Further, a point-by-point method can be used to fabricate FBG sensors where a single narrow UV beam can be used to write the gratings on the fiber.

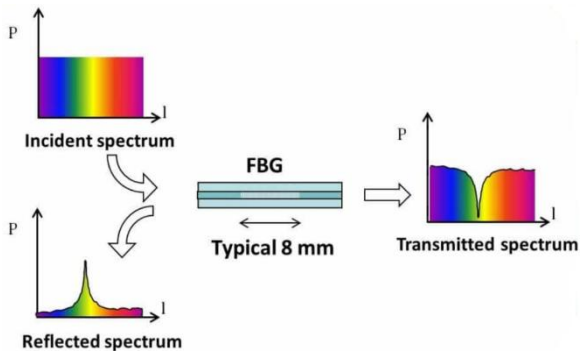

Figure 1: Principle of FBG Sensor [12]

The first demonstration of fabrication of FBG sensors by producing a permanent grating structure was achieved by Hill and Meltz in 1978 [15]. By launching high-intensity Argon-ion laser radiation into a germanium doped fiber, they observed a permanent narrowband Bragg grating filter created in the exposed area [12], [17], [18], [16].

The FBG principle is illustrated in Figure 1. The applied light wave from the Interrogator propagates through the fiber core with negligible attenuation. An interrogator is an optoelectronic instrument, which allows the reading of FBG sensors in static and dynamic monitoring applications. An interrogator can measure a large sensing network composed of various types of sensors (such as for strain, temperature, displacement, acceleration, tilt, etc.) connected along multiple fibers, by acquiring data simultaneously and at different sampling rates. During data acquisition, the interrogator measures the wavelength associated with the light reflected (wavelengths that match the Bragg condition) by the optical sensors and then converts it into engineering units. The ability to accurately preset and maintain the grating wavelength is an important feature and benefit of fiber Bragg gratings. The central wavelength of the reflected component fulfills the Bragg relation provided by equation 1. Because the parameters in equation 1, i.e., periodicity of the grating (Λ) is sensitive to strain while the effective refractive index (n_{eff}) is sensitive to strain as well as to temperature, the reflected wavelength will also change as a function of mechanical and thermal loads. This temperature and strain dependency of the FBG sensors can be used to measure the effect of the thermal and mechanical loads.

The FBG core is made of silica. The index of refraction in silica, which is a dielectric material, is a function of the applied strain and temperature. The structural loads and

temperature variations applied to optical fibers induce optical anisotropy, changing the index of refraction [19]. Because the dielectric constant is a function of the index of refraction, the strain/temperature-induced optical anisotropy affects the propagation of the light wave in the dielectric material. Optical anisotropy induced by external loads and temperature variations causes changes in the spectral response of FBGs. Considering ε_1 as the axial strain and equal transverse strains ($\varepsilon_2 = \varepsilon_3$), we can evaluate the shift of the Bragg wavelength due to uniformly applied strain and temperature changes in a fused silica glass FBG using the following expression [20]:

$$\frac{\Delta\lambda}{\lambda} = \varepsilon_1 - \frac{n^2}{2}\left[P_{12}\varepsilon_1 + (P_{11} + P_{12})\varepsilon_2 - \{\frac{2}{n^3}\frac{dn}{dT} + (P_{11} + 2P_{12})\alpha_f\}\Delta T\right] \quad (2)$$

where P_{11} (0.121) and P_{12} (0.27) are Prockel's coefficients, n (1.46) is the refractive index coefficient, α_f (2e-6/K) is the coefficient of thermal expansion of the glass fiber, dn/dT (10e-6/K) is thermo-optic coefficient, and ΔT is the change in temperature [15], [16].

For a uniaxial mechanical loading condition (Poisson's ratio, $\nu = -\varepsilon_2/\varepsilon_1$) with no thermal change ($\Delta T=0$), the applied strain ε_1 can be derived through measuring the wavelength shift (i.e., $\Delta\lambda$) according to the relation:

$$\frac{\Delta\lambda}{\lambda} = (1\text{-}P_e)\varepsilon_1 \quad (3)$$

where P_e is the effective strain-optic coefficient and is given as:

$$P_e = \frac{n^2}{2}[P_{12} - \nu(P_{11} + P_{12})]$$

As seen in equation 2, the Bragg shift is dependent on both the strain and the temperature. However, the sensitivities to strain and temperature are significantly different. Typical strain and temperature sensitivities were reported to be 1.2 pico-meter/$\mu\varepsilon$ and 13.7

pico-meter/ºC, respectively [12], [15]. The Bragg temperature sensitivity value underscores the need to back out or compensate for temperature impacts to find the actual strain in the materials.

The FBG sensor is a powerful tool to perform online, in-situ monitoring of structures and materials. FBGs are lightweight and small. The diameter of the core (waveguide) is usually around 9 microns. However, the glass cladding and buffer coatings are usually provided to the core to get total internal reflection and to protect the FBG sensor, respectively. A typical diameter of a regular FBG sensor is around 250 microns including the buffer coating. Without the buffer, the diameter reduces to about 125 microns. The grating lengths are typically 5-8 mm but can be tailored depending on the type and need of the application. The small size of the FBG sensor makes it a great candidate for not just surface strain monitoring but also for internal strain monitoring of structures since they can be embedded inside of the structure without significantly altering the elastic and physical properties of the materials/structure. Further, FBG sensors are immune to electromagnetic interference and have very high chemical and temperature resistance. These properties make them ideal for monitoring the manufacturing as well as the in-service condition of the materials.

Evaluating the data from an FBG fiber embedded inside a material is challenging as there are many factors that need to be considered. Many studies utilizing embedded FBG sensors [1], [2], [3], [4], [21], [22], [23], [24] implicitly assumed radial strains equal to the Poisson's ratio contraction in stress/strain calculations. However, if the FBG fiber is being subjected to multi-axial loads, then this assumption could be erroneous as both axial and

radial strains in an optical fiber impact its effective refractive index. The axial and radial strains in the fiber and therefore the wavelength changes are also sensitive to the elastic properties of the matrix, the aspect ratio (length/diameter) of the fiber, and the relationship of the matrix to fiber volumes. Thus, to fully realize the advantages of in situ monitoring of the manufacturing of materials, care needs to be taken in the interpretation of the FBG measurements.

3.0 Experimental Design of Proposed FBG Based Technique

In this section, a thorough analysis of the factors that need to be considered in converting wavelength readings to strain measurements as well as several analyses pertaining to the fundamentals of the single fiber composite using various types of matrix materials are considered and analyzed. To show how differing mechanical properties of the matrix and geometric properties of the FBG fibers and samples can impact the FBG readings, the materials presented include two epoxies, seven tin/bismuth alloys, and ice (water).

From the analyses performed for the material systems used in this research, the following observations were made:

i) The critical fiber length (shown in Figure 2 below) of the FBG fiber is 3.5 mm.

ii) The impact of radial strain on the Bragg shift measurement is insignificant for the materials with the small Young's modulus (1-2 GPa). However, for the materials with large stiffness (>10 GPa), the radial strain impact is significant and should be considered when calculating the axial strain.

iii) It was observed that the FBG sensor measurement is affected by the aspect ratio of the fiber. A small aspect ratio of the fiber was found to have a huge influence on the FBG strain measurement, and the effect waned as the aspect ratio increased.

iv) The volume (diameter) ratio of the fiber to the matrix was also found to influence the FBG strain measurements. For the material system used in this research, it was observed that the material diameter should be at least 100 times the diameter of the fiber to minimize the effect.

v) The numerical study of the strain interaction between the FBG fiber and the thermocouple (TC) revealed that the center-to-center distance (d) between the two sensors should be at least 4 mm to avoid the influence of the TC on the FBG strain measurement.

Based on these observations, the experimental setup as shown in Figure 2 is proposed. The details of the analysis can be found in the subsequent sub-sections.

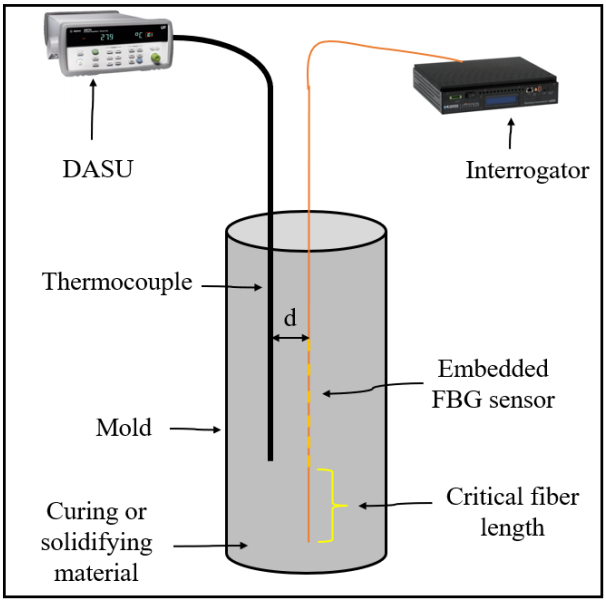

Figure 2: Sketch of a proposed experimental setup

3.1 Shear lag analysis/Fiber ineffective length

To embed the FBG sensor inside a matrix material, the FBG fiber was cut off at one end near the sensor while the other end was connected to an interrogator. Cox [25] first developed a one-dimensional equation for analyzing the stress transfer between the fiber and the matrix and called it a Shear Lag model. Further, it was also demonstrated that the axial stress in the embedded fiber is not constant and varies along the length of the embedded fiber. Cox observed that the stress transfer in the fiber is very small at the end of fiber length and rapidly increases towards the middle of the fiber, being a maximum at the middle of the fiber. The length of the fiber where the stress was zero to the length where the stress was almost equal to the stress at the middle of the fiber was called the critical length (see Figure 2). Hence, in this research, a shear lag analysis was conducted to determine the critical length of the FBG sensor so that the location of the FBG sensor is outside of the effect of critical length. The pictorial depiction of shear lag analysis is provided in Figure 3a-b, and Figure 4a-b.

Usually, the modulus of the matrix is much smaller than that of the fiber and hence it strains more. This occurs at a distance from the fiber but right next to the fiber, the strain is rather small because of the presence of fiber. For a composite under tension, shear stress develops in the matrix that pulls uniformly over the area of the fiber. This makes the stress on the fiber be minimum at the ends and maximum in the middle. To observe that maximum stress, a certain length after the sensor must be kept while cutting off the fiber end so that the FBG sensor reads the accurate stress while the matrix achieves the maximum shear strength.

The main assumption is that the force due to the shear stress τ_i at the interface is balanced by the force due to the variation of axial stress $d\sigma_f$ in the fiber such that [25], [26]:

$$2\pi r dx \tau_i = -\pi r^2 d\sigma_f$$

$$\frac{d\sigma_f}{dx} = -\frac{2\tau_i}{r} \tag{4}$$

Here, σ_f is axial stress on fiber, τ_i is interfacial shear stress between fiber and matrix, and r is the radius of the fiber.

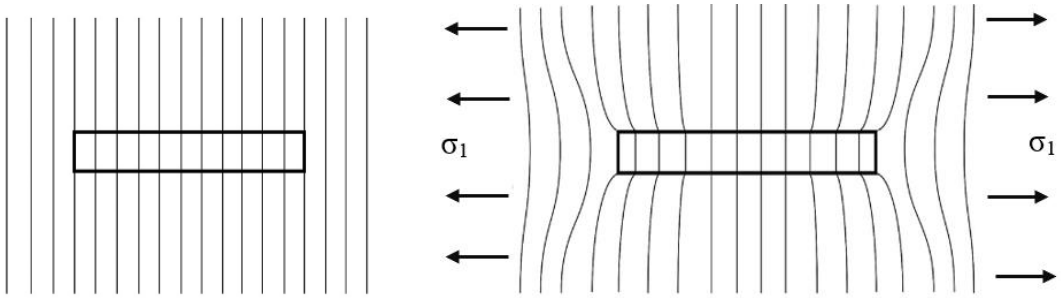

Figure 3: Deformation patterns for a discontinuous high-modulus fiber in a low-modulus polymer matrix. (a) the situation before deformation, and (b) the effect of the application of tensile stress, σ_1, parallel to the fiber axis

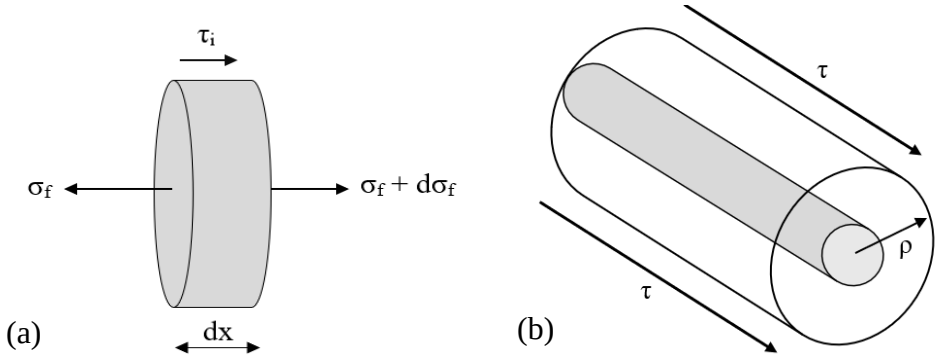

Figure 4: (a) Balance of stresses acting on an element of the fiber of thickness dx in the composite (b) model of a fiber undergoing deformation within a resin used in shear-lag theory. The shear stress acts at an arbitrary radius ρ from the fiber center

It is assumed in the theory that the fiber is surrounded by a cylinder of resin extending to an arbitrary radius ρ from the fiber center, as shown in Figure 4. In this model, it is assumed that both the fiber and matrix deform elastically, and that the fiber-matrix interface remains intact. If u is the displacement of the matrix in the fiber axial direction at a radius ρ, then the shear strain at that position is given by

$$\gamma = \frac{\mathrm{d}u}{\mathrm{d}\rho}$$

The shear modulus of the matrix is defined as $G_m = \tau/\gamma$, hence it follows that

$$\gamma = \frac{\mathrm{d}u}{\mathrm{d}\rho} = \frac{\tau}{G_m} \tag{5}$$

The shear force per unit length carried by the matrix cylinder surface is transmitted to the fiber surface through the layers of resin, and so the shear stress at radius ρ is given by

$$2\pi\rho\tau\mathrm{d}x = 2\pi r\tau_i\mathrm{d}x \tag{6}$$

where τ is the shear stress on the matrix, $\tau_f = \tau_i$ is the shear stress on the fiber.

$$\tau = \frac{r}{\rho}\tau_i \tag{7}$$

Substituting τ in equation 5 gives:

$$\frac{\mathrm{d}u}{\mathrm{d}\rho} = \frac{\tau}{G_m} = \frac{\tau_i}{G_m}\frac{r}{\rho} \tag{8}$$

It is possible to integrate this equation using the limits of the displacement at the fiber surface (i.e., at ρ= r) of $u=u_r$ and the displacement at the matrix surface (i.e., at ρ= R) of $u=u_R$,

$$\int_{u_r}^{u_R}\mathrm{d}u = \frac{\tau_i r}{G_m}\int_r^R \frac{\mathrm{d}\rho}{\rho}$$

$$u_R - u_r = \frac{\tau_i r}{G_m} \ln\left(\frac{R}{r}\right) \tag{9}$$

Combining equation 4 and equation 9,

$$\frac{d\sigma_f}{dx} = -\frac{2\,G_m\,(u_R - u_r)}{r^2 * \ln\left(\frac{R}{r}\right)} \tag{10}$$

Now, strains on the fiber and overall composite strain are as follows:

$$\frac{du_r}{dx} = \varepsilon_f = \frac{\sigma_f}{E_f}$$

$$\frac{du_R}{dx} = \varepsilon_m = \varepsilon_1$$

Here, ε_f is the strain on the fiber and ε_1 is an overall composite strain. Differentiating equation 10 with respect to dx yields:

$$\frac{\partial^2 \sigma_f}{\partial x^2} = -\frac{2\,G_m\left(\varepsilon_1 - \frac{\sigma_f}{E_f}\right)}{r^2\,\ln\left(\frac{R}{r}\right)}$$

$$\frac{\partial^2 \sigma_f}{\partial x^2} = \frac{2\,G_m\,(\sigma_f - \varepsilon_1 E_f)}{r^2\,\ln\left(\frac{R}{r}\right)E_f} \tag{11}$$

Let, $n^2 = \frac{2\,G_m}{\ln\left(\frac{R}{r}\right)E_f}$, then

$$\frac{\partial^2 \sigma_f}{\partial x^2} = \frac{n^2}{r^2}(\sigma_f - \varepsilon_1 E_f) \tag{12}$$

The solution of second-order differential equation 12 is given as:

$$\sigma_f = E_f\varepsilon_1 + B\mathrm{Sinh}\left(\frac{nx}{r}\right) + D\mathrm{Cosh}\left(\frac{nx}{r}\right) \tag{13}$$

Applying boundary conditions

$\sigma_f = 0$ @ $x = \pm L_f$

Here, L_f is fiber half-length

$$\sigma_f = E_f\varepsilon_1\left[1 - \mathrm{Cosh}\left(\frac{nx}{r}\right)\mathrm{Sech}(ns)\right] \tag{14}$$

where $s = \frac{L_f}{r}$

Equation 14 is called the shear lag equation. The shear lag analysis was performed to determine the critical fiber length for the bare glass fiber (i.e., after stripping the acrylate coatings) and for the glass fiber with acrylate coating (see Figure 5a, and Figure 5b). In both cases, it was assumed in the theory that the fiber is surrounded by a cylinder of resin extending to a certain radius from the fiber center [27].

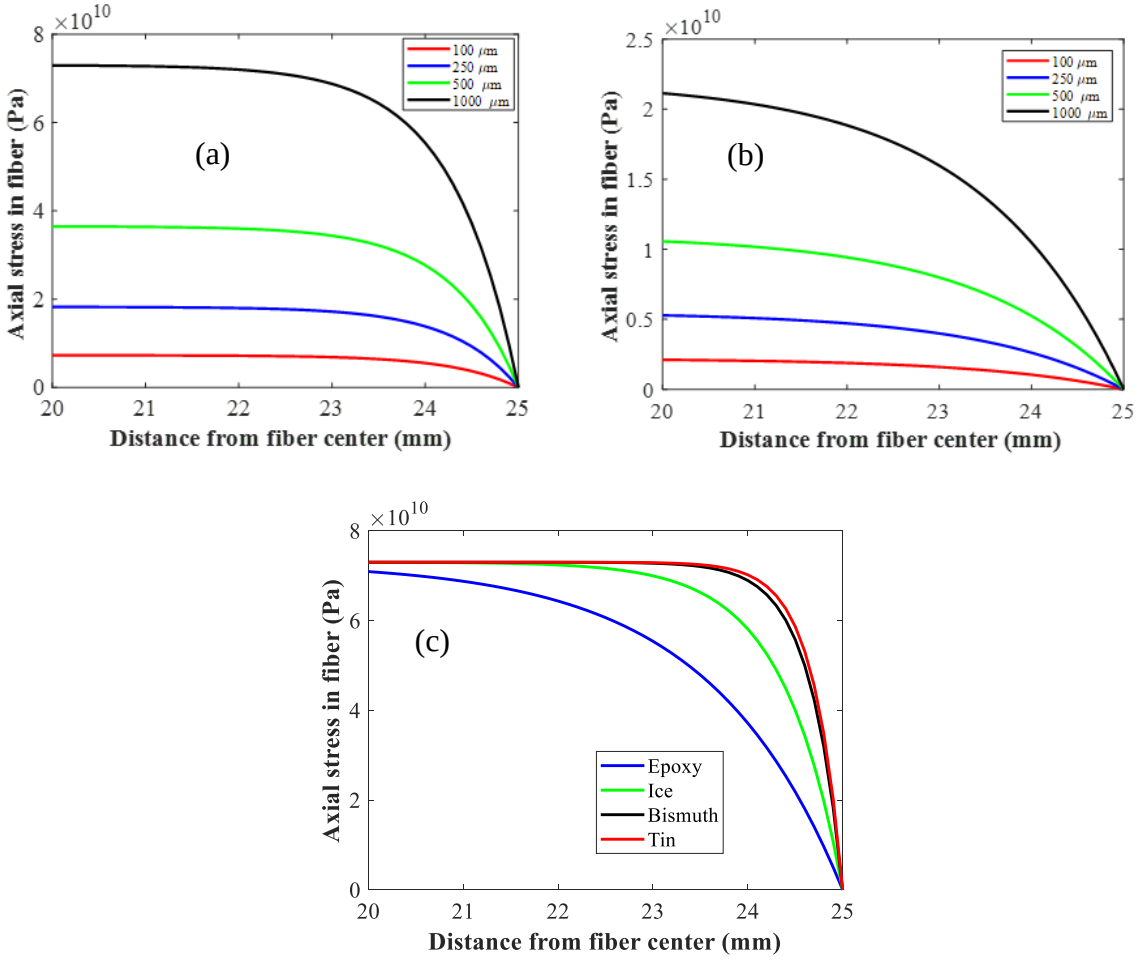

Figure 5: Shear lag analysis for fibers of various diameters, a) for bare glass fiber in polymer, b) for acrylate coated fiber in polymer, c) for bare glass fiber embedded in various matrix materials

From the shear lag analysis, it was observed (see Figure 5a and Figure 5b) that the critical length of the fiber (ineffective fiber length) is ~3.5 mm for fiber with and without acrylate coating. i.e., at least 3.5 mm of FBG fiber should be left after the sensor to eliminate the end effect. It was also observed that with an ineffective fiber length of 3.5 mm, the sensor was able to pick more than 99 percent of the stress developed. Further, it was observed that the ineffective fiber length decreases with the increase in the matrix stiffness (see Figure 5c).

3.2 Impact of radial strains and aspect ratio

The simplified relation between the peak wavelength ($\Delta\lambda$) shift of an FBG sensor to the refractive index of the waveguide and the thermal and axial mechanical strain in the fiber is often presented as [2], [12], [16]:

$$\frac{\Delta\lambda}{\lambda} = k\varepsilon_m + k\alpha_f\Delta T + \alpha_\partial\Delta T \tag{15}$$

where, λ is the base FBG wavelength, k (0.78) is the elasto-optic constant, ε_m is the axial mechanical strain, α_f (2e-6/K) is the coefficient of thermal expansion (CTE) of the glass fiber, α_∂ (6.5e-6/K) is the thermo-optic constant, and ΔT is the change in temperature. This equation can be obtained by partially differentiating equation 1 with respect to temperature and strain and then combining them.

Equation 15, even though widely used in the FBG community [1], [2], [28], [29], [30], [31], [32], [21], [22], is precise only when the radial strains are equal to the longitudinal strain multiplied by the negative of the Poisson's ratio of the fiber. For all other cases, the

effect of radial strain on the Bragg shift needs to be considered. Hence, the following more accurate governing equation might need to be applied [14], [15], [33]:

$$\frac{\Delta\lambda}{\lambda} = \varepsilon_1 - \frac{n^2}{2}\left[P_{12}(\varepsilon_1 + \varepsilon_2) + P_{11}\varepsilon_2 - \left(\frac{2}{n^3}\frac{dn}{dT} + (P_{11} + 2P_{12})\alpha_f\right)\Delta T\right] \quad (16)$$

where, ε_1 and ε_2 are the principal axial and radial strains in the fiber, respectively, and other variables are as defined previously.

It was previously reported in [1] and [2] that the impact of radial strain on wavelength shift is in fact insignificant when the FBG fiber is embedded in a polymer matrix with a low Young's modulus. The results, however, could be very different when an FBG fiber is embedded in a matrix which has a much higher stiffness compared to that of the polymer. Further study to observe whether the simplification of the governing equation would have significant consequences on the measured axial strains is necessary. Hence, the following theoretical analysis of a fiber embedded in four different matrices was performed:

I. *Using the Eshelby approach* [27], [34] *the principal axial (ε_1) and radial (ε_2) strains in the fiber due to an applied strain to each solid matrix were calculated*

The technique of equating stresses in actual and equivalent homogenous inclusions (Eshelby approach) leads to [27], [34] the following equations:

$$\mathbf{C_f}(\varepsilon^C + \varepsilon^A) = \mathbf{C_m}(\varepsilon^C - \varepsilon^T + \varepsilon^A) \quad (17)$$

$$[\mathbf{C_f}S - \mathbf{C_m}(S - I)]\varepsilon^T = \mathbf{C_m}\varepsilon^A - \mathbf{C_f}\varepsilon^A$$

$$\varepsilon^T = [\mathbf{C_f}S - C_m(S - I)]^{-1}(\mathbf{C_m}\varepsilon^A - \mathbf{C_f}\varepsilon^A)$$

$$\varepsilon^T = [\mathbf{C_f}S - \mathbf{C_m}(S - I)]^{-1}(\mathbf{C_m} - \mathbf{C_f})\varepsilon^A \quad (18)$$

where, $\varepsilon^c = S\varepsilon^T$ is the constrained strain, ε^T is the transformative strain, ε^A is the applied strain in the matrix, S is the Eshelby tensor, I is an identity matrix, ε is the strain in the

FBG fiber, $\mathbf{C_f}$ and $\mathbf{C_m}$ are the compliance matrices of the glass fiber and the matrix, respectively.

The material properties utilized in this analysis are indicated in Table 1. Now, the strain in the matrix material is the difference between the strain in the FBG fiber (ε) and the constrained strain, i.e.,

$$\varepsilon^A = \varepsilon - \varepsilon^C \tag{19}$$

$$\varepsilon = \varepsilon^C + \varepsilon^A$$

$$\varepsilon = S\varepsilon^T + \varepsilon^A$$

$$\varepsilon = S[\mathbf{C_f}S - \mathbf{C_m}(S - I)]^{-1}(\mathbf{C_m}\varepsilon^A - \mathbf{C_f}\,\varepsilon^A) + \varepsilon^A \tag{20}$$

Table 1: Elastic, thermal, and geometrical properties of the FBG fiber and the materials used in this study

Properties	FBG fiber	Epoxy	Tin	Bismuth	Ice
Young's Modulus (GPa)	73.00	2.00	42.00	33.00	10.00
Poisson's ratio	0.17	0.32	0.31	0.31	0.33
Measured CTE (10-6/K)	2.00	72.06	23.74	12.55	48.00
Diameter (mm)	0.125	18.00	15.00	15.00	200.00
Length (mm)	45.00	50.00	45.00	45.00	600.00

Let us assume an arbitrary applied matrix strain of ε^A = [-0.01 -0.01 -0.01 0 0 0] and no temperature change. The calculated axial (ε_1) and radial (ε_2) fiber strains for four materials using equation 20 as a function of the fiber aspect ratio are provided in Figure 6a, and 6b, respectively. For all four materials, it was observed that the strain in the fiber is a function of the aspect ratio. For a small aspect ratio fiber, the axial strain expected in the fiber is smaller than the applied matrix strain. However, as the aspect ratio increases, the axial strain produced in the fiber converges to the applied matrix strain. On the other

hand, the radial strains are expected to be more compressive with a stiffer matrix material and become slightly less compressive (or even tensile in the case of the polymer) and converge to an asymptotic value as the aspect ratio of the fiber increases.

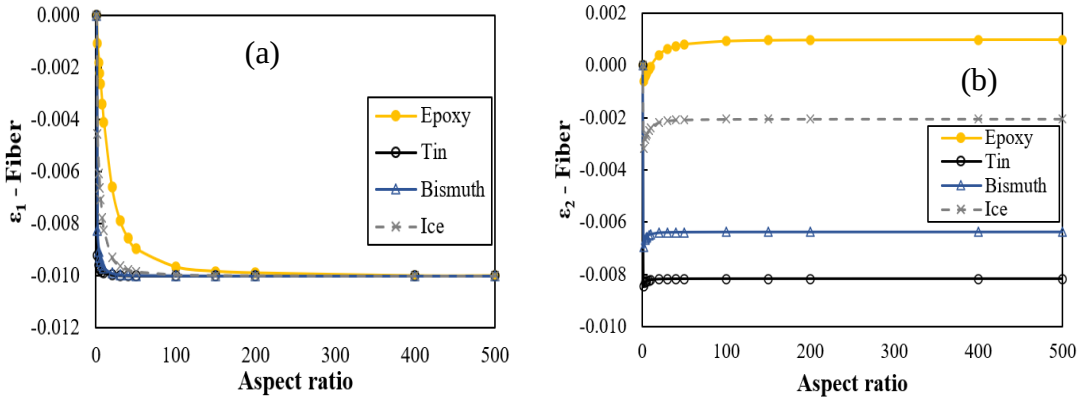

Figure 6: (a) ε_1 and (b) ε_2 of fiber as a function of aspect ratio for various materials

II. The *calculated axial (ε_1) and radial (ε_2) strains were used to compute the expected shift in Bragg wavelengths using (A) ε_1 only (eq 21) and (B) both ε_1 and ε_2 (eq 22*)

For an applied mechanical load at a constant temperature, the FBG wavelength shift is related to the strains as:

Case A: Considering axial strains only

$$\frac{\Delta\lambda}{\lambda} = k\varepsilon_1 \tag{21}$$

Case B: Considering both axial and radial strains

$$\frac{\Delta\lambda}{\lambda} = \varepsilon_1 - \frac{n^2}{2}[P_{12}(\varepsilon_1 + \varepsilon_2) + P_{11}\varepsilon_2] \tag{22}$$

where all the variables and constants are as defined previously.

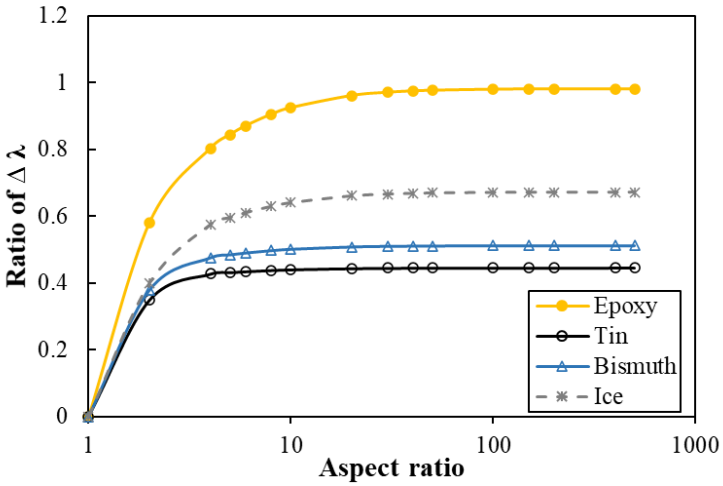

Figure 7: Ratio of shift in wavelength as calculated including both axial and radial strains (Eq. 22) to only including axial strain (Eq. 21) as a function of fiber aspect ratio for various materials

Using equations 21 and 22, and by using the strain measures from Figure 6a, and Figure 6b, the change in the Bragg shifts were calculated considering both cases A and B. The ratios of the shift in the Bragg wavelength calculated including both axial and radial strains to those including axial strain only for four different materials investigated in this study are presented in Figure 7. As can be seen, for a single fiber polymer composite with a large aspect ratio fiber, the ratio of the Bragg shift is very close to 1, i.e., the difference in the Bragg shift obtained by including and excluding radial strain in the calculation is very small. However, for other materials investigated, the ratio decreases as the matrix stiffness increases. In other words, the change in the Bragg shift calculated including and excluding the radial strains becomes more and more different as the matrix stiffness increases. Therefore, for a matrix with large stiffness, the impact of the radial strains on the Bragg shift ($\Delta\lambda$) is significant and should not be neglected during strain estimation.

III. *Ratio of $\varepsilon_2/\varepsilon_1$ was calculated for various applied matrix strains and matrices*

For an aspect ratio of 300, which is similar to that of the fibers used in the experiments, various matrix strains were applied to the developed theoretical model to calculate the ratio $Z = \varepsilon_2/\varepsilon_1$ for each material and to confirm that it is constant regardless of the applied hydrostatic strain. Z heavily depends on the elastic properties of the matrix and the fiber. While the elastic properties of the FBG fiber are constant (the same type of fiber is used in all the experiments), the elastic properties of the matrix vary with materials and alloy composition. Using the stiffnesses of tin and bismuth in Table 1, the Young's moduli of the other alloys were interpolated using the rule of mixtures, a simple approach that produces values very close to the more complicated Hashin-Shtrikman method [35].

It was also found that for a given material and geometry, Z is constant regardless of the applied strain. Hence, for further analyses, equation 16 is used and is modified to incorporate $\varepsilon_2 = Z\varepsilon_1$. Further the impact of temperature on the CTE of the fiber has been subtracted from equation 16 to obtain the total strain producing equation 23. The reason for subtracting the thermal impact on the CTE of the fiber will be discussed in chapter 9.

$$\frac{\Delta\lambda}{\lambda} = \varepsilon_1 - \frac{n^2}{2}\left[P_{12}(\varepsilon_1 + Z\varepsilon_1) + P_{11}Z\varepsilon_1 - \frac{2}{n^3}\frac{dn}{dT}\Delta T\right] \tag{23}$$

3.3 Impact of elastic properties of matrix

Figure 8 shows the axial strains estimated including and excluding the radial strains as a function of the matrix to fiber stiffness ratio. The range of Poisson's ratios shown in the figure was based on the Poisson's ratios of the materials investigated in this research. The assumed aspect ratio of the fiber was large (>300), and the material ratio (matrix

diameter/fiber diameter) was also considered to be large (>100) to match the experimental setup.

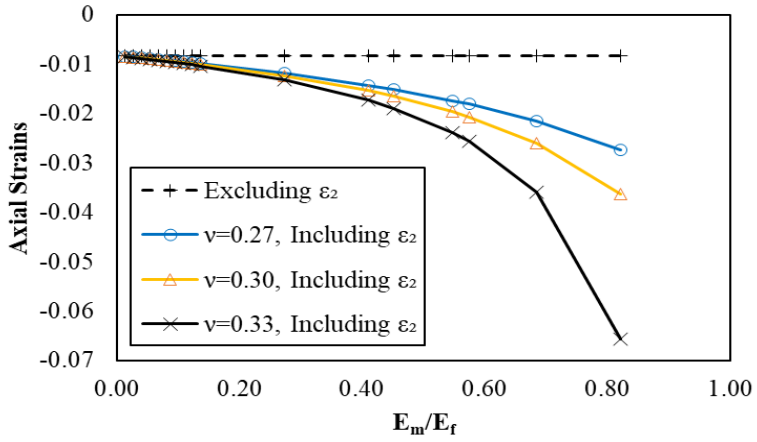

Figure 8: Axial fiber strains calculated for various matrix to fiber stiffness ratios and matrix Poisson's ratios for an arbitrary 1% hydrostatic matrix contraction

The difference in axial strains estimated including and excluding radial strains becomes higher as the matrix stiffness increases. When the radial strain was considered in the calculation, the effect of Poisson's ratio on the axial strains was found to be small for matrices with low Young's moduli. However, the effect became significant for materials with large stiffnesses. When rearranging the simplified equation 15 to estimate axial strains, the relative stiffnesses of the matrix and the fiber are not considered. The stiffness of the polymers is in the range of 2-3 GPa and hence, for polymer matrices, the difference caused by excluding the radial strains in the calculations is minimal. Thus, for materials with small stiffnesses, the simplified equation can be used to convert the measured Bragg shift into the axial strains [2]. However, for materials with high stiffness properties such as tin, bismuth, aluminum, etc., the error caused by excluding the radial strain in the

calculation is significant and is also dependent on the Poisson's ratio of the matrix and hence the use of the simplified equation to estimate the axial strain would be erroneous.

3.4 Evaluation of diameter (volume) effect on actual wavelength changes

Using elasticity theory, a model was developed to relate the expected Bragg measurements to the material and geometrical properties of the matrix and the fiber. In this model, the stresses in the fiber, σ_{zz} and σ_{rr}, need to be calculated either numerically from finite element (FE) model or analytically. A schematic of a single fiber composite model is shown in Figure 9, where 'a' and 'b' represents the radius of the fiber and the matrix, respectively.

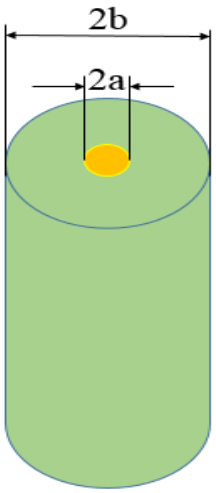

Figure 9: Single fiber composite model

These stresses are of course dependent on the geometry of the system and the fiber and matrix elastic properties. When both mechanical and thermal loads are present on a glass fiber, the axial and radial strains are expressed as:

$$\varepsilon_1 = \varepsilon_1^M + \varepsilon_1^T \quad (24a)$$

$$\varepsilon_2 = \varepsilon_2^M + \varepsilon_2^T \quad (24b)$$

where, ε_1^M is axial mechanical strain, ε_2^M is radial mechanical strain, ε_1^T is axial thermal strain and ε_2^T is radial thermal strain. From the theory of elasticity, the axial, and the radial mechanical strains in a fiber in cylindrical coordinates are provided as [36]:

$$\varepsilon_1^M = \frac{1}{E_f} * (\sigma_{zz}^f - \nu_f \sigma_{rr}^f - \nu_f \sigma_{\theta\theta}^f) \quad (25a)$$

$$\varepsilon_2^M = \frac{1}{E_f} * (\sigma_{rr}^f - \nu_f \sigma_{zz}^f - \nu_f \sigma_{\theta\theta}^f) \quad (25b)$$

where, σ_{rr}^f, $\sigma_{\theta\theta}^f$, σ_{zz}^f are the radial, hoop, and axial stresses in a fiber, respectively. E_f and ν_f is the Young's modulus and Poisson's ratio of the glass fiber, respectively.

Similarly, the thermal strains are expressed as:

$$\varepsilon_1^T = \alpha_f * \Delta T \quad (26a)$$

$$\varepsilon_2^T = \alpha_f * \Delta T \quad (26b)$$

Considering $\sigma_{rr}^f = \sigma_{\theta\theta}^f$, and combining equations 24a, 24b, 25a, 25b, 26a, 26b, and substituting in 16 yields:

$$\frac{\Delta\lambda}{\lambda} = \frac{1}{E_f}\left[\left\{\left(1 - \frac{n^2}{2}(P_{12} - (P_{12} + P_{11})\nu_f)\right\}\sigma_{zz}^f - \left\{2\nu_f + \frac{n^2}{2}(1 - \nu_f)P_{11} + (1 - 3\nu_f)P_{12}\right)\right\}\sigma_{rr}^f\right] + \left(\frac{1}{n}\frac{dn}{dT} + (P_{11} + 2P_{12})\alpha_f\right)\Delta T \quad (27)$$

where all the constants and the variables have been defined previously.

Equation 27 is the relationship between the Bragg shift and the elastic material properties of the fiber. σ_{rr}^f and σ_{zz}^f can be obtained either numerically or analytically using the approach presented in section 6.

From Figure 10, it can be observed that for a larger matrix radius (b/a>100), the Bragg shift converges to a limit for each matrix material (i.e., depending on the material elastic

properties). The effective behavior of the matrix-fiber assembly will be now more representative of the matrix as the ratio of matrix volume to fiber volume increases. Hence, the matrix diameter should be at least 100 times larger than the fiber diameter to avoid the impact of the size of the sample on the FBG measurements for the materials considered in this study.

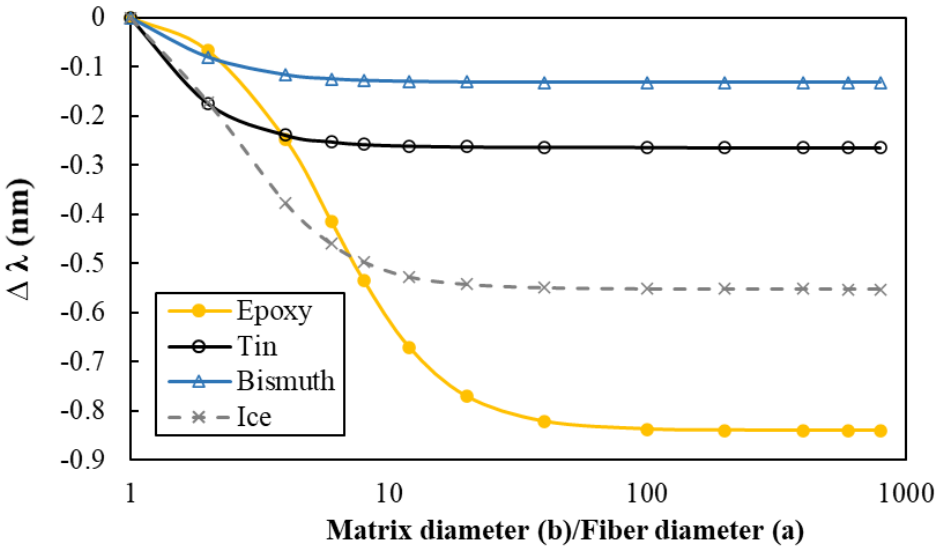

Figure 10: Volume effect on Bragg shift for various materials

3.5 FBG fiber – thermocouple interaction

It is understood that a TC is highly recommended in monitoring of extreme application materials such as polymers and metals, as the temperature inside the sample could be significantly different than that of the ambient condition. This allows for the proper temperature compensation of FBG sensors to help in determining various manufacturing characteristics associated with polymers, metal alloys, and ice such as the beginning and

end of curing, the gel point, the magnitude of the residual curing stresses, solidification temperature, beginning and end of solidification/crystallization etc. However, for the correct application of a TC, its position within a matrix in which it is being embedded must be carefully analyzed to reduce undesirable FBG - TC interactions which could negatively affect the FBG measurements.

To determine the strain interaction between the FBG and TC sensors, 3D linear elastic FE models were built in COMSOL 5.5a by placing an FBG fiber in the middle of the substrate (epoxy, alloys, and ice) while the TC was placed a certain distance from the center. The diameter of the TC (1 mm) was several orders of magnitude larger than the diameter of the FBG fiber (0.125 mm). Therefore, a careful evaluation of the FBG-TC strain interaction had to be performed. In this model, the substrate, FBG fiber, and TC were assumed to be isotropic. Elastic, thermal, and geometrical properties of the substrate and the fiber are provided in the Table 1. The Young's modulus, Poisson's ratio and CTE of the TC were 200 GPa, 0.30, and 7e-6/K, respectively. The analysis was performed for various diameters of the TC, 0.5, 1, 2, and 4 mm.

The entire substrate-fiber-TC assembly was numerically cooled down by 100 °C and a parametric analysis was performed (i) to observe the effect of center-to-center distance (s) of the TC from the FBG fiber and (ii) to investigate the TC diameter's (D) effect on the buildup of cooling strains in the FBG fiber.

From the result from the FE analysis, it was concluded that, for all substrate conditions, the center-to-center distance between the FBG and TC should be at least 3 TC diameters to negate the effect of the FBG-TC strain interaction. It is observed that, for the center-to-

center distance of two TC diameters, the strain is affected by less than 1%. Therefore, in all the work performed in this dissertation, the TC (Diameter, D = 1 mm) was kept at least 4 mm away from the FBG sensors.

Monitoring of Single Fiber Polymer Composites Using FBG Sensors

4.0 Introduction

Fully cured epoxies exhibit an excellent range of mechanical and thermal properties such as ease of processing, stability at high temperature, high strength, and good adhesive characteristics that justify their use in high-performance products [37] [38]. Hence, epoxy resins have found their use in many industrial applications such as surface coatings, adhesives, and as matrices in fiber-reinforced composites [37], [39], [40] [41].

The curing process is usually carried out at an elevated temperature depending on the nature of the epoxy and the curing agent [42] [43] [44] [45] [46] [47]. The curing phenomenon in epoxy is exothermic in nature, which means that heat is generated during the cure. In the early part of the curing process, the polymer doesn't have a defined skeleton structure formed just yet, hence, the epoxy resin behaves as a viscoelastic liquid which can relieve stress by viscous flow. However, as the curing process continues, a critical point in network formation is reached and is exemplified by the formation of a 3D skeleton structure. This critical point is known as gelation. At the gel point, a continuous network, which is characterized by having a measurable equilibrium modulus, is formed. After gelation, the epoxy resin continues to react, forming a highly crosslinked solid.

Cure monitoring can aid in optimizing the cure cycle of epoxies and composites [48] [49] [50] [51] [52] [53] [54] [55]. Understanding and identifying the stages of curing can allow manufacturers to optimize the cure cycle and manufacturing process thereby

improving the quality control and facilitating reliable manufacturing of composite products [48] [49] [50] [51] [52] [53] [54]. The curing system plays a significant role in the manufacture of epoxy-based composites. Generally, the theoretical strength of the epoxy resin is much greater than the actual strength, and one of the reasons for this is residual stress in the cured epoxy resin. Residual stresses are produced in the epoxies because of the curing and manufacturing process that leads to different cooling conditions and different cooling rates which are detrimental to the ultimate performance of the epoxies and epoxy-based composites [39], [40] [41]. To understand the evolution of residual stresses in epoxy resins during curing, manufacturing, and in-service condition, it is necessary to study the curing process as well as the physical and mechanical behavior of fully cured epoxy resins.

A single glass fiber, such as a single optical fiber containing an FBG sensor [41] [42] [43] [44] [45] [46], placed in the curing mixture will initially strain according to its CTE as the temperature changes. Eventually, the gel point is reached when there is enough of a skeletal structure to allow strain transfer, provided an interface is also established [56]. As the reaction continues, the polymer will be subject to thermal expansions and contractions and the curing process will usually lead to an overall shrinkage as the covalent bonds are formed. The strain transfer to the fiber from the thermoset, combined with curing shrinkage and the mismatch in the CTEs, will lead to residual stresses and strains.

4.1 Degree of cure

The degree of cure (DOC) in a polymer is a numerical representation of how far the chemical crosslinking process has advanced. Mathematically, it is defined as a number between 0 and 1 (or 0% and 100%), where 0 is the beginning of the cure and 1 represents the end of the cure. Most of the mechanical properties of the epoxy improve with the increase in the DOC [57] [58] [59] [60]. Similarly, under-curing can lead to under-strength adhesion between fiber layers, not fully formed elastic properties, potential geometric distortions, etc. The DOC value can provide insight about whether the polymer is still a liquid, has become a gelled highly viscous semi-solid, or has fully solidified [57] [58].

Figure 11 shows the progression of the DOC during a typical epoxy curing cycle. As an increasing number of chemical crosslinks are formed, the DOC value increases towards 1. Progression of the DOC during the curing process is well documented in [61] and summarized as follows:

1. (DOC 0 or close to 0) Initially, the resin is comprised of short monomers before polymerization and flows like a liquid.
2. With time and the addition of heat, the curing reaction begins. The monomers start to polymerize together to form longer polymer chains. Further, crosslinking between the polymer chains starts to occur.
3. (DOC around 0.5-0.7) The curing reaction rate is at its highest and the 3D skeleton structure starts to form. This restricts the resins' ability to flow. For a bi-functional monomer and tri-functional cross-linkers, at about a DOC 0.7 [62] [63] the resin

reaches a gelled state (gelation) where resin flow stops, and the resin behaves like a semi-solid gel material.

4. The epoxy resin has transformed into a solid material that cannot flow anymore. The curing reaction slows down as most of the crosslinks have formed.

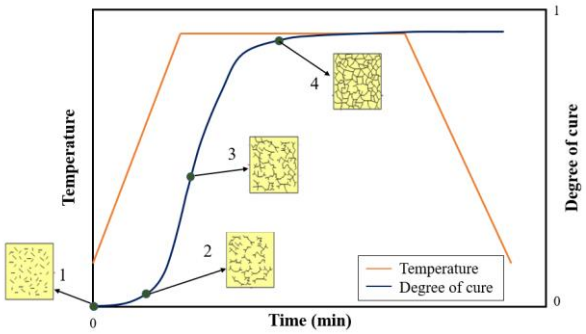

Figure 11: Illustration of DOC in polymers [57]

DOC of polymers can be evaluated using various techniques, for example, Fourier transform infrared (FTIR) spectroscopy, rheometer, differential scanning calorimetry (DSC), etc. The analysis method and measurement device are chosen based on the phenomena occurring during the adhesive curing process.

In DOC evaluation with a rheometer, changes in the viscosity of a sample are studied. The changes in viscosity due to reactivity are continuously measured to check cure behavior. However, solids with a high shear modulus cannot be measured, making it difficult to measure the end of the reaction in some epoxies [57] [58] [59] [60]. Hence, this method is mainly used to evaluate the initial process during which a solid begins to form.

Evaluation of DOC using an FTIR spectrophotometer involves the observation of the changes in the functional group i.e., shifts in the number of functional groups are checked

under determined curing conditions. The curing conditions are obtained by assuming that curing is complete when there is no further change in the functional groups [58].

DSC uses the concept of thermal heat balance to evaluate the DOC. This technique provides information about the properties of a polymer such as the glass transition temperature (T_g), the extent of polymerization, the enthalpy of reaction, etc. [64], [65], [66], [30], [67]. In this technique, the changes in the heat transfer between two calorimetric cells (one of them being a reference cell) as a function of time or temperature are compared from before, during, and after the reaction under determined curing conditions. In either case, the required curing conditions are obtained by assuming that curing is completed when the heating value reaches zero [59].

DSC is typically used in laboratories under ideal conditions. Although DSC typically is not used in practical applications, it provides excellent information about the reaction kinetics of materials. With the ongoing research about the use of in-situ cure monitoring methods, Raman spectroscopy has been thought to have a good potential in the real world since Raman spectroscopy is a non-destructive monitoring method [68].

McIlhagger et al. [69], Kim and Lee [70], and Bang et al. [71] developed a dielectric system for the in-situ cure monitoring of composites. Using the parameters derived from dielectric measurements such as the resistance, capacitance, and dissipation factor, the transitions in the resin such as gel point, vitrification, and full cure were identified.

Lots of research work has been performed to develop an in-situ cure monitoring system based on dielectric measurements. Almost all the experimental work involving dielectric measurements, however, was carried out under non-isothermal conditions. It has been

stated that to observe the cure through the thickness of composite materials, sensors for the dielectric system must be implanted within the matrix. This effort, however, has been reported to adversely affect the mechanical performance of the parts [68].

In this section, a short review of existing DOC monitoring techniques was presented. As reviewed, numerous methods have been developed to monitor the cure progress of epoxies/polymers and Polymer Matrix Composites (PMCs) [59], [60], [62], [63], [64], [65], [66], [67], [68], [72]. Most of these methods, however, are destructive or typically are not practiced for in-situ cure monitoring because they are only performed in the laboratories under ideal conditions. Some of the methods can be utilized to monitor the curing process in real-time [68], [69], [71]. Any in-situ cure monitoring technique must be non-destructive so that the manufacturing process and materials are not influenced or even disturbed.

The in-situ DOC measurement techniques also suffer from a lack of accuracy and can be extremely expensive, tedious, and time-consuming [72]. Hence, in this dissertation, a novel Fiber Bragg Grating (FBG) sensing-based technology has been proposed to evaluate the DOC for epoxies. The cure behavior of a commercially available room temperature (RT) and higher temperature (HT) epoxy resin systems obtained from Fibre Glast Corp. [73] and Duralco Corp. [74], respectively, were characterized. The cure kinetics of the epoxy systems were characterized by using embedded FBG sensors.

4.2 Residual stress/strains

Residual stresses in the epoxies are those stresses that exist in the epoxies even after the removal of any external loads and are most likely the result of the manufacturing

process. In this section, the methods used to measure residual stresses in epoxy resins and PMCs by previous researchers are presented.

4.2.1 Residual stresses in epoxy resins

Numerous methods such as the use of strain gages, interferometry, layer removal, beam bending, etc. have been used to measure residual stresses in epoxies [38]. Volumetric change that takes place during the manufacturing process is a primary source of residual stress in composites. Volumetric change is a combination of the chemical shrinkage and the thermal expansion/contraction due to temperature change. The relative contribution of chemical shrinkage and temperature changes to the final residual stress has been the subject of debate [75]. It has been well established that the thermal contraction of the resin upon cooling from the curing temperature has a huge effect on the residual stresses in resins. The change in temperature and the difference in CTEs between the matrix and the fiber leads to the formation of the residual stresses in PMCs. The presence of a stiff mold might act as a constraint and further contribute to the magnitude of the residual stress. In a traction-free environment, an epoxy resin might develop residual stress because of the differential cooling of the epoxy, especially when the temperature range of interest includes the glass transition temperature T_g.

Many researchers have measured very small residual stresses (< 5 MPa) in composites due to the curing shrinkage and deemed them insignificant when compared to the magnitude of the residual stress caused by the cooling process [75]. During the curing process, the stiffness of the epoxy resin is not fully developed. Hence, it was assumed that the stress developed because of the shrinkage is relieved by viscoelastic relaxation.

However, in some papers [76], it was argued that the effect of chemical shrinkage on the residual stress is significant and should not be ignored. Further, it must be acknowledged that the PMCs might be under a high degree of constraints by the large stiffness as well as the orientation of the fiber, the geometry of the mold, etc. These geometrical constraints might contribute further to making the magnitude of the residual stress even larger.

Asamoah et al. [77] used photo-thermoelastic and finite element methods to evaluate the residual stress formation and distribution in fiber-reinforced polymers (FRP). They found that with an increase in fiber volume fraction, the residual stresses in the material also increased. Others have also investigated the stress distribution in ~~the~~ epoxy resin/FRPs subjected to a volumetric constraint and found similar results [78] [79].

Mechanical and physical properties such as modulus, CTE, T_g, etc. of the resin have a direct influence on the magnitude as well as the development process of the residual stress. It has been concluded that an epoxy resin with higher T_g is likely to develop larger residual stress upon cooling [42]. Further, it was observed that a larger Young's modulus and CTE result in larger residual stress.

4.2.2 Effect of residual stresses

Many failures in composites are associated with residual stresses [80]. The presence of residual stresses in PMCs significantly deteriorates the interface and contributes to the debonding between the fiber and the matrix [80], [81] [82]. The presence of residual stress could also foster matrix cracking, crack propagation, reduced dimensional stability, and lower yield strength, etc. [82], [83], [84], [85], [86]. Further, failures such as fatigue, creep, stress corrosion cracking, fracture, buckling, etc. are also either caused or augmented by

the presence of residual stress [85], [86]. Residual stresses at the fiber-matrix interface, lamina, laminate, and structural levels all influence the strength of the component. Therefore, it is necessary to be aware of the presence of the residual stresses as they are likely to be a failure factor.

4.2.3 The importance of residual stress measurement

It has been demonstrated that the magnitude of the residual stress can be estimated easily if the shrinkage contribution on the residual stress is neglected [85], [86], [87], [88], [89], [90], [91], [92]. The estimation of shrinkage contribution to the total residual stress in the epoxy/composites is a challenge. Some researchers, however, were able to calculate the total residual stress without neglecting the shrinkage contribution [86]. It has been demonstrated that the magnitude of the residual stress whether estimated with or without considering the shrinkage contribution is significant when compared to the yield and tensile strength of the epoxy matrix. If these stresses are not precisely measured and understood, the stress state of the whole composite might be misrepresented [93], [94], [95], [96], [97]. The misrepresentation of the stress state could have a significant influence on the safety factor of the design, potentially leading to under-design and ultimately to untimely and catastrophic failure of composite structures. If residual stresses are not considered throughout the structural design phase, a higher safety factor should be considered for the structure, potentially resulting in overweight and over-designed structures [91].

4.2.4 Measurement of residual stresses

The accurate measurement of residual stress in epoxy resins and composites is very challenging as the composite manufacturing process is complex. During the manufacturing

of composites, the materials go through complex processes and have nonlinear changes of properties, phase transformations, material discharges, mechanical and thermal problems, etc. Hence, the predictive models and experimental methods are challenging to build. Experimentally, residual stress can be measured by destructive and nondestructive methods. The destructive methods [98], [99], [100], [101], [102], [103], [104], [105] involve destroying the specimen in some way. The destructive methods render the composites unusable after testing. They all involve taking a portion out of the specimen to create a free surface and release the stresses on the surface. The limitations associated with destructive methods are not enough spatial resolution, not accurate strain reading, not being able to measure the stress in thick laminates, etc.

Nondestructive methods on the other hand use techniques such as X-ray diffraction, strain gauges, neutron diffraction, etc. Although the nondestructive methods are more favorable for mechanical testing, the existing nondestructive methods for residual stress measurement are somewhat limited. X-ray diffraction measures strain in the crystal lattice of polycrystalline materials by examining variations in the inter-planar spacing [106], [107]. Residual stresses up to a maximum depth of about 0.05 mm can be measured. For deeper measurement, layer removal such as etching is required, making this method a form of destructive testing. Cox et al. [107] applied this technique to measure the residual stresses in silicon-carbide reinforced titanium alloys.

In [108], [109], [110] embedded aluminum inclusions randomly distributed between the plies and subjected to X-ray diffraction were successfully utilized to monitor high-temperature polymer matrix composites for the onset of internal cracking during

manufacturing [111]. In this method, X-ray diffraction was utilized to measure the residual stress of composites by including metal filler particles in the matrix material. The issue with this technique is that the filler materials are distributed throughout the composite and hence influence the elastic and physical properties of the composites globally. In addition, the relationship between residual stress and the results from X-ray diffraction needs to be carefully correlated to obtain meaningful information.

There are various other methods that have been tried and tested to measure the residual stresses. Some of these methods are the cure referencing method, acoustic wave method, interferometry method, Raman spectroscopy, photo-elastic method, etc. [60-74], [112], [113], [114]. This section attempted to provide a brief introduction to the widely used methods for measuring the residual stress in the composites. It was shown that a considerable number of such methods have been tried, based on different properties related to these stresses. There seems to be considerable scope for future research in this field of study.

4.3 FBG sensor for strain measurements in polymers/composites

Encouraged by the excellent properties of the FBG sensor, the composites community has started measuring the strains in composite structures either by adhering FBG sensors on the surface or by embedding sensors inside of the composite structure. Lawrence et al. [115] measured the internal strain of a graphite/epoxy composite during processing using the embedded FBG sensor and thermocouples. They embedded a Fabry-Perot interferometer, an FBG sensor, and a TC in a laminate before cure. The specimens were

cured in a press and the internal strains developed during the manufacturing process were monitored.

Kang et al. [23] performed a simultaneous measurement of strain and temperature during the cure of an asymmetric cross-ply composite laminate using fiber optic sensors. They used Fiber Bragg grating/extrinsic Fabry-Perot interferometric (FBG/EFPI) hybrid sensors to measure the strains and temperatures. They identified the thermal behavior of the asymmetric laminate by measuring two-directional strains. Through these experiments, FBG/EFPI sensors were proven to be an efficient choice for monitoring composite structures.

Chen et al. [24] used FBG sensors and ultrasonic measurement techniques to monitor the evolution of material properties during the cure by measuring the chemical and mechanical properties of the curing composites. The measurement from the FBG was validated against DSC measurements. They successfully demonstrated that the FBG sensor can be used to monitor the process-induced strains in 16 ply graphite/epoxy composites.

Wang et al. [116], [117] proposed an integrated technique to measure critical mechanical properties of polymeric materials using an FBG sensor. By curing a polymer of interest around an FBG sensor and by measuring the Bragg wavelength shift as the polymerization occurs, they developed a combination of experimental and theoretical models to estimate chemical shrinkage, CTE, and modulus in an integrated manner. They argued that this technique would provide a much-needed tool for rapid and accurate assessment of polymer properties, which, in turn, would enhance the accuracy of predictive stress/strain modeling of polymer encapsulated components. In the extension of their work,

they successfully demonstrated a novel technique to measure the effective chemical shrinkage progression and modulus evolution of advanced polymers during polymerization [98]. By embedding FBG sensors in two uncured cylindrical polymer specimens with different configurations, a theoretical relationship was derived between the Bragg wavelength shifts and the evolution of the properties, and an inverse numerical procedure to determine the properties from the Bragg wavelength shifts was established. Further, they validated the consistency of their work by performing two independent verification experiments: a self-consistency test to verify the measurement accuracy of raw data and a warpage measurement test of a bi-material strip to verify the accuracy of evolving mechanical properties.

Further research on the foundation built by Wang was performed by Sun, and Han [98], [118]. They proposed an FBG based experimental method to measure the elastic properties of epoxy molding compound (EMC) from a single specimen configuration. They embedded the FBG sensor in the center of a cylindrical EMC specimen, and by assuming that the FBG sensor deforms together with the EMC during compressive and hydrostatic loadings, the Young's modulus and bulk modulus are determined from the BW shifts using the relationships between the elastic constants and the BW shift. Further, they also estimated the shear modulus and Poisson's ratio from the measured constants to provide a complete set of elastic properties of EMC.

As discussed in section 4.2, there are various methodologies that could be used to measure the residual strains and stresses. However, these techniques all come with their own shortcomings. For example, some methods cannot be performed in-situ, some are

intrusive and affect the mechanical and physical properties of the sample, some don't work in an electromagnetic environment, and some are just very expensive. Hence, many researchers have shifted their focus towards FBG sensors which alleviates most of those shortcomings. Various existing techniques involving FBG sensors are used in composite technologies as a surface sensor to measure the process-induced strains on the surface of the composite structure. A few researchers have embedded FBG sensors inside laminated composites and successfully demonstrated their use in measuring the strains. However, as far as this author is aware, no research has been reported regarding the in-situ monitoring of single fiber/epoxy composites for residual stresses not only in the fiber but also in the matrix.

During the curing and manufacturing of epoxy-based composites, the epoxy resin goes through various characteristic points such as the gel point, the end of the cure, the end of manufacturing, etc. DSC, DMA, etc. have been used in the past by various researchers to understand the cure behavior. The disadvantage of the existing techniques lies in the fact that they can be extremely time-consuming for specimen preparation, very expensive, cannot be done in-situ, and it can be difficult for non-experts to practice routinely. Hence, there is a need for a novel in-situ measurement technique that can effectively monitor the curing behavior of epoxy resins and composites.

With consideration to all the above aspects, a novel technique that can monitor the cure behavior for gel point, end of the cure, etc., and measures the process-induced residual strains and stresses in the fiber and the matrix is highly desired. In this work, FBG sensors were used to:

- Detect the gelation point (fiber/matrix interface formation)
- Identify the beginning and the end of the cure (i.e., DOC)
- Determine residual curing and manufacturing strain in the fiber and the matrix
- Determine residual curing and manufacturing stresses in the fiber and the matrix
- Monitor in service as well as degradation of single fiber polymer composites

5.0 Experimental Setup

5.1 Materials and experimental methods

In this research, two types of epoxies were tested as the matrix material. The two epoxies were Fibre Glast 1000 epoxy/1025 hardener and Duralco 4460 from Fibre Glast Corp. and Duralco Corp., respectively. The recommended curing temperatures for Fibre Glast 1000 epoxy was room temperature (RT) for 24 hours and for Duralco 4460 higher temperature (HT) epoxy, 121 ºC for 4 hours. Further, the manufacturers' recommended epoxy hardener mixing ratio for RT epoxy was 100:17 and for HT epoxy was 100:80 parts by weight. The experimental sketch and the actual setup used for this research is shown in Figure 12a, and Figure 12b, respectively.

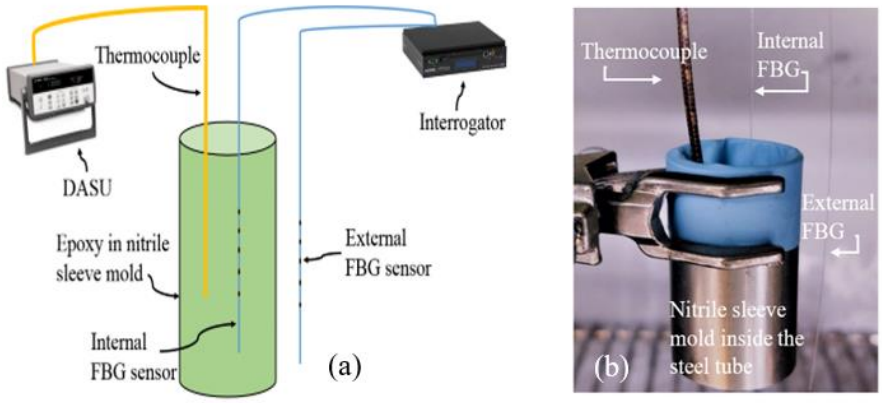

Figure 12: (a) Schematic of experimental setup (b) Experimental setup

5.2 Methodology

To create each single fiber composite based on the RT and the HT epoxy, a Corning SMF 28 optical fiber with an FBG sensor from Technica SA was placed in the middle of a flexible nitrile sleeve mold as shown in Figure 12. A steel tube was used in each case to support the nitrile sleeve. The nitrile sleeve mold, which was free to expand and contract, did not contribute to any stress during the manufacturing process. A K-type wire TC was also placed inside the molds to monitor the temperature inside the curing samples. The TC was placed at least 4 mm away from the FBG sensor to avoid the strain interaction with the FBG sensor. Another free-standing FBG sensor was placed near the surface of the molds to monitor the temperature of the oven.

The optical fiber was stripped of its acrylate coating to ensure effective strain transfer from the epoxy to the waveguide containing the FBG. The epoxy was mixed in a 100:17.5 and 100:80 (epoxy: hardener) ratio by weight for RT and HT epoxies respectively and stirred for about two minutes according to manufacturer instructions. For certain experiments, the stirring time was extended up to 10 min to evaluate the effect on potential temperature and strain variations. After a rest period of one minute to allow for settling of the mixture, it was poured into the nitrile sleeve.

After completing the specimen preparation process, the oven was turned on and the temperature was gradually increased to specified ambient temperatures. For RT epoxy, the curing experiments were conducted at ambient oven temperatures of 30 °C, 50 °C, and 70 °C. Similarly, the experiment was run 3 times for HT epoxy at an ambient oven temperature of 121 °C. The isothermal experimental temperature was maintained until the epoxy was

fully cured and the temperature of the epoxy had returned to that of the oven. The whole system was then cooled down to room temperature. A Micron Optics Hyperion si155 interrogator was used to collect peak FBG wavelength readings and an HP 34970A Data Acquisition Unit (DASU) collected TC readings, both every 10 seconds. After the curing process was complete and the sample temperature reached the ambient oven temperature, the oven was turned off and the sample was allowed to cool back down to room temperature.

5.3 Effect of acrylate coating on measurements / Removal of acrylate coatings

Generally, manufacturers coat optical fibers with polymers or metals to protect them from damage [79], [91]. For all of the experiments in this dissertation, a fiber with an acrylate buffer was selected. The diameter of the FBG glass core with the cladding is 125 microns and the total diameter with the polymer/acrylate coating is 250 microns. Initial trials of the experiment showed some unexpected patterns (rapid rises) in the measured wavelengths for acrylate coated fibers as seen in Figure 13a. Experiments were therefore conducted to determine the effect of acrylate coatings on the wavelength measurements from FBGs. A MS1-08S-40-FS Micro-Strip fiber coating removal tool was used to strip the acrylate coatings from the FBG sensors.

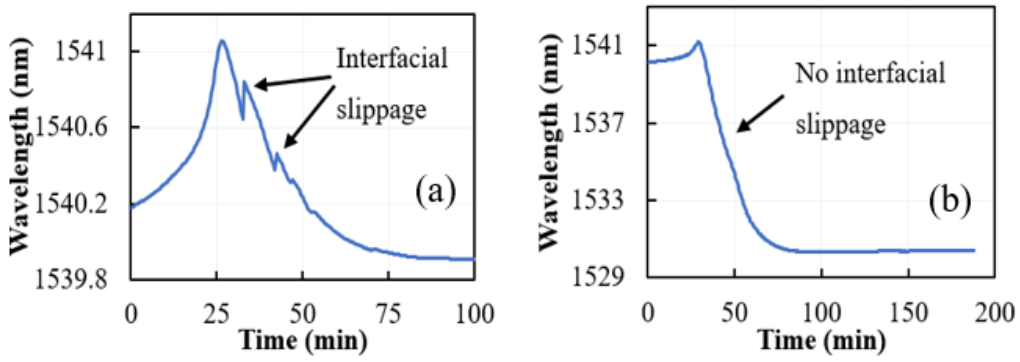

Figure 13: Peak wavelengths from (a) acrylate coated FBG sensor and (b) from coating removed FBG sensor

Initial measurements (Figure 13a) show that an FBG with acrylate coating does not necessarily reflect the true strains of the epoxy during curing in the single fiber composites. The measured shift in peak wavelengths of acrylate coated and bare fiber FBG sensors are shown in Figure 13a, and Figure 13b respectively. The multiple spikes observed in the acrylate coated FBG sensor sample are likely due to slippage at the interface between the FBG sensor and the cured epoxy. These slips which are a result of imperfect bonding might be responsible for hindering the strain transfer from the matrix to the fiber. The FBG sensors with the coating removed, on the other hand, formed better bonding and showed no sign of slips as evidenced by the smooth wavelength profile.

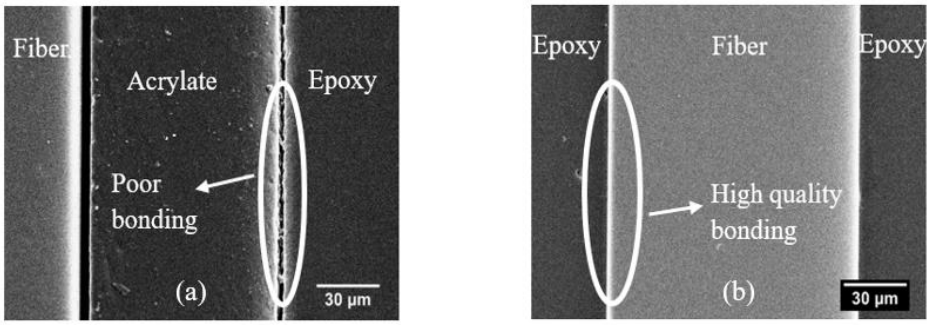

Figure 14: SEM images of (a) low-quality bonding between acrylate and epoxy and (b) high-quality bonding between FBG glass fiber and epoxy

To support this hypothesis, scanning electron microscope (SEM) images of samples with acrylate coated and coating removed FBG sensors were produced to see the bonding between the FBG fiber and the epoxy. In acrylate coated FBG fibers, a significant gap was observed between the FBG fiber cladding and the acrylate coating (Figure 14a). A gap was also observed between the acrylate coating and the cured epoxy. This gap could reduce the strain transfer from epoxy to the FBG sensors. Stripped FBG sensors on the other hand showed excellent bonding with the cured epoxy (Figure 14b) and hence better strain transfer compared to the acrylate coated FBG sensors.

Additionally, the relaxation of the soft acrylate coating may hinder the transfer of stress from the matrix to the fiber. Therefore, for all the experimental work done in this research, stripped FBG sensors were used.

6.0 Experimental Results

6.1 Calculations of ambient temperature and residual strains in FBG sensors

It was previously established in section 3 that, for the matrices with small Young's modulus, the impact of radial strain on the FBG measurement is negligible. Hence, for the epoxy section of this research, a simplified formula was used to make the necessary calculations.

Using the reflected wavelength of the freestanding external FBG that has only thermal impact, equation (15), and the CTE of the optical fiber, α_f, the change in temperature in the ambient environment can be calculated. From eq. 15:

$$\frac{\Delta\lambda}{\lambda} = k\alpha_f \Delta T_A + \alpha_\delta \Delta T_A \tag{28}$$

$$\frac{\Delta\lambda}{\lambda} = (k\alpha_f + \alpha_\delta)\Delta T_A \tag{29}$$

$$\Delta T_A = \frac{\Delta\lambda/\lambda_0}{(k\alpha_F + \alpha_\delta)} \tag{30}$$

where T_A is the ambient temperature measured by the FBG sensor.

The residual strain at any point in time is defined for this research to be the difference between the actual strain in the fiber and the strain that the fiber would have undergone due to thermal expansion in the absence of the mechanical interaction with the epoxy. Thus, to determine the axial residual strain in the fiber, start with

$$\Delta\lambda_{int}/\lambda_{0int} = k\varepsilon_{int} + \alpha_\delta \Delta T_{int} \quad (31)$$

$$k\varepsilon_{int} = \Delta\lambda_i/\lambda_{0int} - \alpha_\delta \Delta T_{int} \quad (32)$$

$$\varepsilon_{int} = \frac{\Delta\lambda_{int}/\lambda_{0int} - \alpha_\delta \Delta T_{int}}{k} \quad (33)$$

where $\Delta\lambda_{int}$ is the change in the measured peak wavelength of the internal FBG, λ_{0int} is the starting peak wavelength for the internal fiber, ε_{int} is the total axial strain in the internal embedded fiber, ΔT_{int} is the change in the internal temperature as measured by the embedded thermocouple, and the other terms are defined as before.

Then, the axial residual strain (ε_{res}) is:

$$\varepsilon_{res} = \varepsilon_{int} - \alpha_f \Delta T_{int} \quad (34)$$

$$\varepsilon_{res} = \frac{\Delta\lambda_{int}/\lambda_{0int} - \alpha_\delta \Delta T_{int}}{k} - \alpha_f \Delta T_{int} \quad (35)$$

6.2 Temperature profiles of epoxy curing

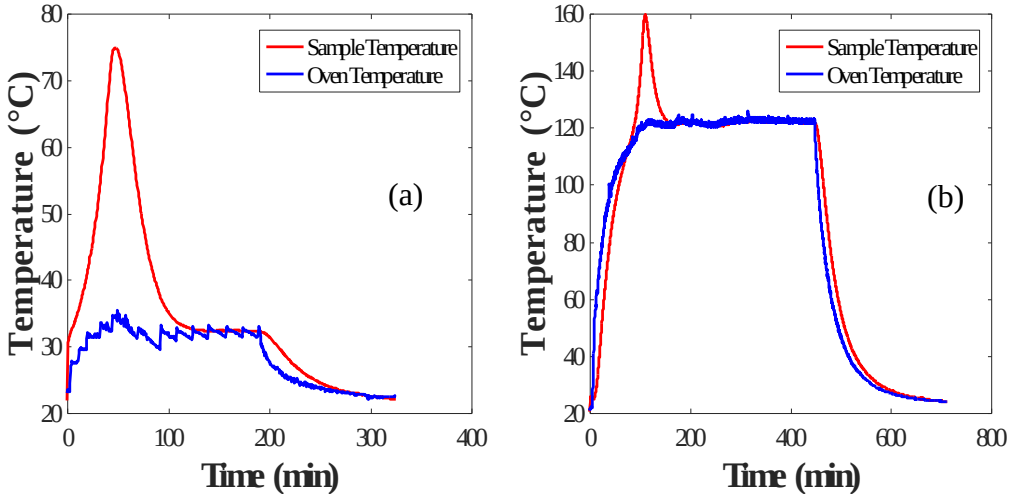

Figure 15: Sample and ambient temperature profiles from embedded TC and external FBG sensor for RT (a) and HT (b) epoxies

An embedded thermocouple and a freestanding FBG sensor were used to measure the internal and oven temperatures respectively. Figure 15 shows examples of the disparities in measured temperature profiles between the external free standing FBG sensor and the embedded thermocouples for RT (Figure 15a) and HT epoxies (Figure 15b). The temperatures measured by the two temperature probes are significantly different for both types of epoxies as the external free standing FBG is not subjected to the heat of reaction of the epoxy. The curing reaction between epoxy and hardener is exothermic in nature which releases a significant amount of heat. As the reaction takes place, the exothermic heat increases the temperature of the epoxy. This increase in temperature accelerates the curing process producing more heat which further increases the temperature of the system. Eventually, the reactant supply is diminished, the reaction slows down, and the temperature of the system starts to drop towards the experimental oven temperature as much of the curing is complete.

For room temperature epoxy, the embedded (Trial 1) temperature overtakes the ambient (see Figure 15a) as soon as the hardener is mixed with the resin, as the polymerization reaction begins immediately, and the temperature of epoxy exceeds the 30 °C target oven temperature. For the higher temperature epoxy however, ambient temperature exceeds the embedded temperature initially, as the polymerization reaction for this higher temperature epoxy begins only when the temperature of the epoxy is close to the curing temperature recommended by the manufacturer (121 °C). Once, the temperature inside the epoxy approaches the advised curing temperature, the curing reaction begins,

and the embedded (Trial 1) temperature overtakes the ambient temperature as shown in Figure 15b.

6.3 Room temperature and high temperature cure epoxy

The raw wavelength and the temperature profiles obtained from curing of RT epoxy at 30 ºC, 50 ºC, and 70 ºC are presented Figure 16, and Figure 17, respectively. Similarly, Figure 18 provides the wavelength and temperature profiles of three independent tests as measured by the embedded FBG sensor and the internal thermocouple for HT epoxy cured at 121 ºC. Figure 19 depicts an example of the progression of the peak wavelengths at the target temperature of 50 °C and, using equation 35, the calculated axial residual strain on the optical fiber during the experimental process. In Figure 19, arrow 1 indicates the end of cure identified using equation 41 and arrow 2 indicates an arbitrary point in cooling process. The conductivity factor (described in detail in section 6.4) is optimized between these two points indicated by arrows 1 and 2.

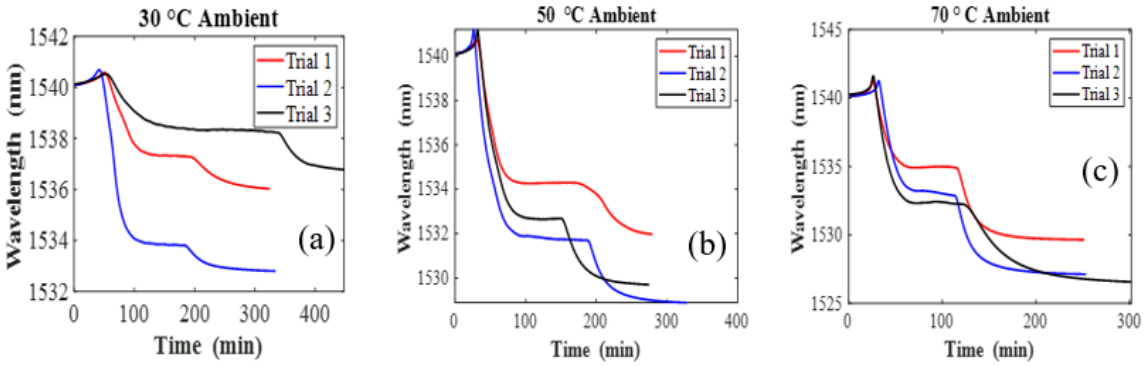

Figure 16: Wavelength profiles of RT epoxy cured at (a) 30 ºC, (b) 50 ºC, and (c) 70 ºC

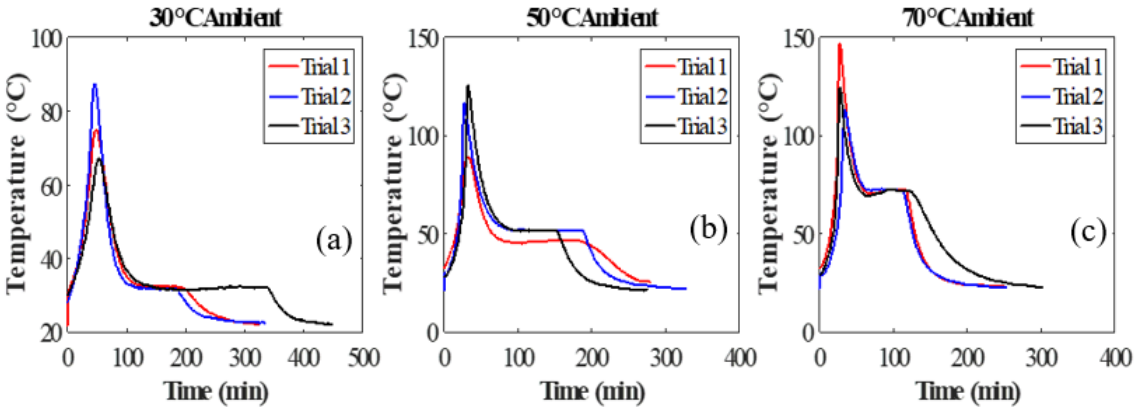

Figure 17: Measured sample temperatures of RT epoxy cured at (a) 30 ºC, (b) 50 ºC, and (c) 70 ºC

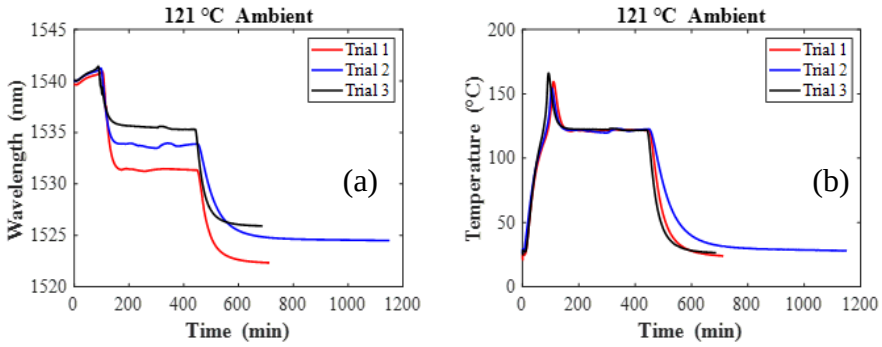

Figure 18: Wavelength (a) and temperature (b) profiles obtained from curing of HT epoxy at 121 ºC

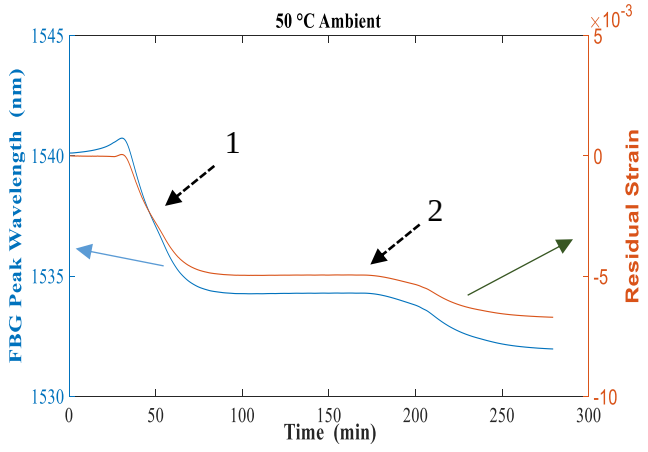

Figure 19: FBG peak wavelengths and determined residual strains for a typical experiment.

In each case there is an initial rise in the temperature, a peak temperature driven by the exothermic reaction, a cooling to the ambient temperature and a final cooling to room temperature. Figure 16 and Figure 18a illustrate the wavelengths for all twelve trials. In general, a higher oven temperature produced a larger shift in the wavelengths and potentially a larger axial residual strain at the end of the manufacturing cycle. Further discussion on the residual strains is provided in section 6.6.

6.4 Degree of cure

6.4.1 RT epoxy

6.4.1.1 Determination of end of curing for RT epoxy

Using the temperature readings of the embedded thermocouple (see Figure 17), an approach was developed to identify the completion of cure. In a perfect experiment with continuous temperature measurements, the following relation could be applied:

$$dT_{int}/dt = \Delta H/C_P - k_c(T_{int} - T_A) \quad (36)$$

where t is time, ΔH is the instantaneous heat generated by the exothermic curing reaction at each time step, k_c is the convective cooling rate, C_p is the heat capacity of the sample (assumed to be constant within each individual trial), and the other terms are defined as before. For this model, the heat lost to the ambient environment is proportional to the difference in temperatures of the sample and the environment. Then the curing would

be complete when no more heat is generated, i.e., at the point at which $\Delta H(t)=0$, and in this case equation 36 becomes

$$dT_{int}/dt = -k_c(T_{int} - T_A) \tag{37}$$

From this time forward, the internal temperature would follow a smooth cooling curve between the dotted arrows 1 and 2 shown in Figure 19. After the second dotted arrow (2), the cooling of the entire system commences until room temperature is reached.

A modified approach was used to determine the time by which a specified percentage of the total heat was generated, 99.8% for this study. The temperature measurements were discretized into thirty second time intervals. At each time step (n), the internal temperature and ambient temperature were measured by the embedded thermocouple and, using equation 30, by the external FBG sensor. Like the continuous case, in each time step, the change in the internal sample temperature is governed by the heat capacity of the sample, the heat generated from the exothermic reaction, and the heat lost to the ambient environment. Thus,

$$T_{int}(n) = T_{int}(n-1) + \frac{\Delta H(n)}{C_p} - K_C[T_{int}(n-1) - T_A(n-1)] \tag{38}$$

where $T_{int}(n)$ and $T_A(n)$ are the internal and ambient oven temperatures at the n^{th} step, $\Delta H(n)$ is the heat generated by the curing reaction in the n^{th} step, K_C is time step length dependent conductivity factor, and C_p is as defined before. Since the temperature is not constant in each time step, the formula is refined to use the average temperature of the starting and ending points of the sample:

$$T_{int}(n) = T_{int}(n-1) + \frac{\Delta H(n)}{C_p} - K_C\left(\frac{T_{int}(n)+T_{int}(n-1)}{2} - \frac{T_A(n)+T_A(n-1)}{2}\right) \tag{39}$$

which leads to

$$\frac{\Delta H(n)}{C_p} = T_{int}(n) - \left[T_{int}(n-1) - K_C\left(\frac{T_{int}(n)+T_{int}(n-1)}{2} - \frac{T_A(n)+T_A(n-1)}{2}\right)\right] \quad (40)$$

Therefore, in this model, the heat generated in a time step is proportional (by the factor C_p) to the difference between the current sample temperature and the temperature the sample would have cooled to in that step in the absence of any generated exothermic heat. The part of the formula inside the brackets in equation 40 is termed for the purposes of this research as the stepped-cooling temperature (expected zero enthalpy cooling temperature). Figure 20 illustrates the calculation of $\Delta H(n)/C_p$ using equation 40. The stepped-cooling temperature is indicated in the bottom right of the figure.

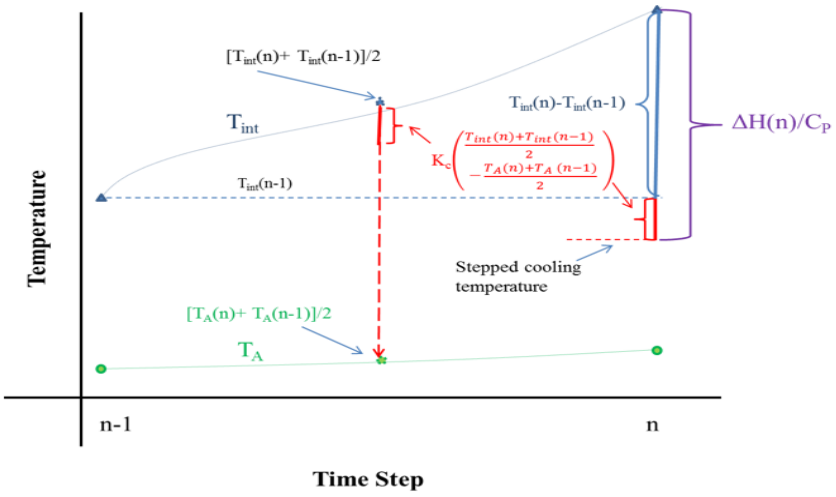

Figure 20: Schematic showing determination of $\Delta H/C_P$ as the sum of temperature increase during step n and cooling that would have occurred in absence of any exothermic reaction

Taking the sum of ΔH(n) across the timeline of the experiment gives the total heat generated. Thus, to determine the completion of curing, when 99.8% of the heat is generated, the following equation needs to be solved for N':

$$\frac{\sum_{n=1}^{N'} \Delta H(n)/C_P}{\sum_{n=1}^{N} \Delta H(n)/C_P} = \frac{\sum_{n=1}^{N'} \Delta H(n)}{\sum_{n=1}^{N} \Delta H(n)} = 99.8\% \quad (41)$$

where N is the total number of time steps measured across the entire experiment. A further refinement is made due to the volatility of the temperature readings, so that negative exothermic heat is not allowed. Thus, ΔH(n) is always set at a minimum of zero.

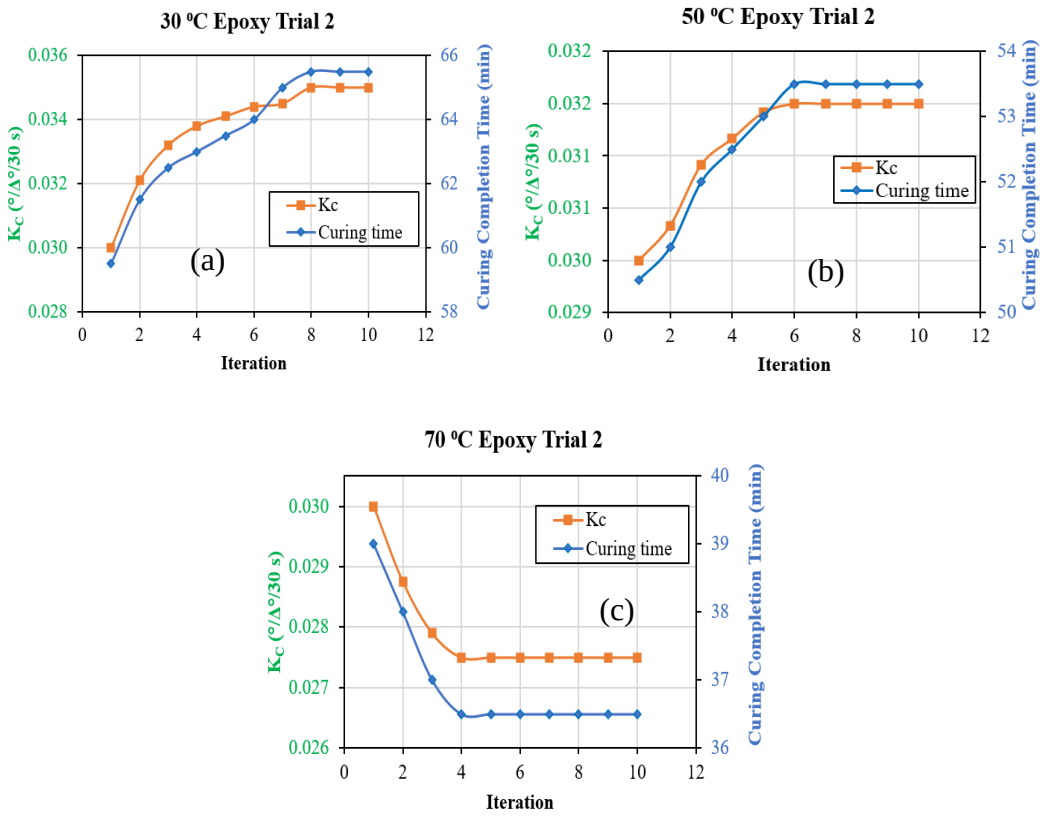

Figure 21: Convergence of K_c for RT epoxy cured at (a) 30 ºC, (b) 50ºC and (c) 70 ºC

Because K_c is not known a priori and may depend upon the position of the thermocouple inside the sample, a trial K_c (of 0.03/30s) was first used. Then the 99.8% completion point was calculated using equation 41. Next, the parameter K_c was optimized by best fitting a cooling curve between the identified curing completion point and the second dotted arrow in Figure 19 to the actual temperature profile. This was done by using equation 41 with 0 substituted for $\Delta H(n)/C_p$. The process of determining the completion point and optimizing K_c was iteratively run 10 times and it was checked that K_c converged to an optimized value. The optimization of K_c can have significant effects on the calculated curing completion time and the convergence can be quick or can take up to the ten steps (see Figure 21).

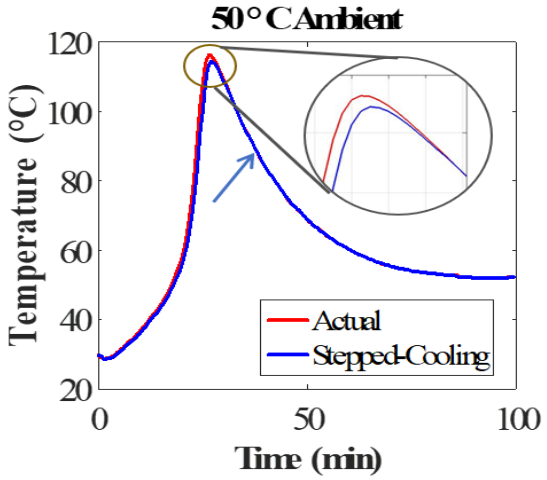

Figure 22: Actual and stepped-cooling curves for one sample at 50 °C

Table 2: Curing completion times and optimized cooling rate factor

		Curing Time (minutes)			K_C (°/Δ°/30 s)		
	Target Temperature	**30 °C**	**50 °C**	**70 °C**	**30 °C**	**50 °C**	**70 °C**
Trial	1	69	47.5	41.0	0.0250	0.030	0.0327
	2	65.5	53.5	37.5	0.0350	0.0318	0.0275
	3	66.5	41.0	40.0	0.0312	0.0312	0.0312
	Average	**67.0**	**47.3**	**39.5**			

Figure 22 shows the actual internal temperature and the stepped cooling curve for one of the 50 °C trials calculated by the heat balance algorithm for the time until the second dotted arrow. While the exothermic curing reaction was occurring, the actual temperatures were above the stepped cooling points. After the curing completion point was reached, the two curves were nearly identical as no further heat was generated. The second dotted arrow indicates the end of curing as determined by the algorithm. Table 2 lists the times to reach curing completion for all nine trials and the optimized conductivity factors. As expected, thermal energy from higher temperatures led to faster curing completion times. Variations in the thermal cooling rate factor could be attributed to slightly different positioning of the thermocouple within the samples.

6.4.2 HT epoxy

6.4.2.1 Determination of start of cure for HT epoxy

As noted previously, the RT epoxy starts to react with the curing agent as soon as they are mixed. Hence the start of cure for RT epoxy would be the time when the resin and the hardener are mixed.

For the higher temperature curing epoxy, convective heat is supplied until the sample reaches the temperature at which polymerization begins and continues until the polymerization is complete. The manufacturer advised temperature for the polymerization reaction to occur for this higher temperature epoxy system is 121 °C.

The heat balance model discussed in the previous section can be used to determine the DOC of an epoxy system. In this model, a heat balance equation is utilized to calculate the exothermic heat generated in each 30 second time step during the curing process:

$$\Delta H(n) = Cp\left\{T_{int}(n) - \left[T_{int}(n-1) - K_c\left(\frac{T_{int}(n)+T_{int}(n-1)}{2} - \frac{T_A(n)+T_A(n-1)}{2}\right)\right]\right\} \quad (42)$$

where, all the constants and variables are as defined previously.

The temperature measurements are from the thermocouple and the free-standing FBG sensor. In the ideal case, the expected epoxy temperature in the absence of exothermic heat, $T_{int}(n-1) - K_c\left(\frac{T_{int}(n)+T_{int}(n-1)}{2} - \frac{T_A(n)+T_A(n-1)}{2}\right)$, is equal to the measured epoxy temperature $T_e(n)$ until the polymerization begins. The start of cure would be the first point when ΔH becomes positive, i.e., the first time when $T_e(n)$ would be higher than $T_{int}(n-1) - K_c\left(\frac{T_{int}(n)+T_{int}(n-1)}{2} - \frac{T_A(n)+T_A(n-1)}{2}\right)$.

This theoretically correct concept however has been modified to accommodate the noise in the measured data in this experiment. The DOC through an arbitrary number of time steps N' is

$$\frac{\sum_{n=1}^{N'} \frac{\Delta H(n)}{C_P}}{\sum_{n=1}^{N} \frac{\Delta H(n)}{C_P}} = \frac{\sum_{n=1}^{N'} \Delta H(n)}{\sum_{n=1}^{N} \Delta H(n)} \quad (43)$$

Where, N represents the total number of time steps and C_P is the heat capacity of the

sample. This approach can be extended to determine the start of the cure in higher temperature epoxies by identifying the time by which the DOC as defined by this formula reaches some minimal value, for example 1%:

$$\frac{\sum_{n=1}^{N'} \Delta H(n)}{\sum_{n=1}^{N} \Delta H(n)} = 1\% \tag{44}$$

Therefore, the start of cure for this research is defined as the time when 1 % of the total heat has been generated, i.e., solve for N' such that

$$\sum_{n=1}^{N'} \Delta H(n) = 0.01 * \sum_{n=1}^{N} \Delta H(n) \tag{45}$$

6.4.2.2 Determination of end of cure for HT Epoxy

The approach used in section 6.4.1 to determine the end of cure for RT epoxy can be used to determine the end of cure for HT epoxy. The method calculates the time taken by the epoxy system to achieve 99.8% of cure, i.e., solve for N'' such that

$$\sum_{n=1}^{N''} \Delta H(n) = 0.998 * \sum_{n=1}^{N} \Delta H(n) \tag{46}$$

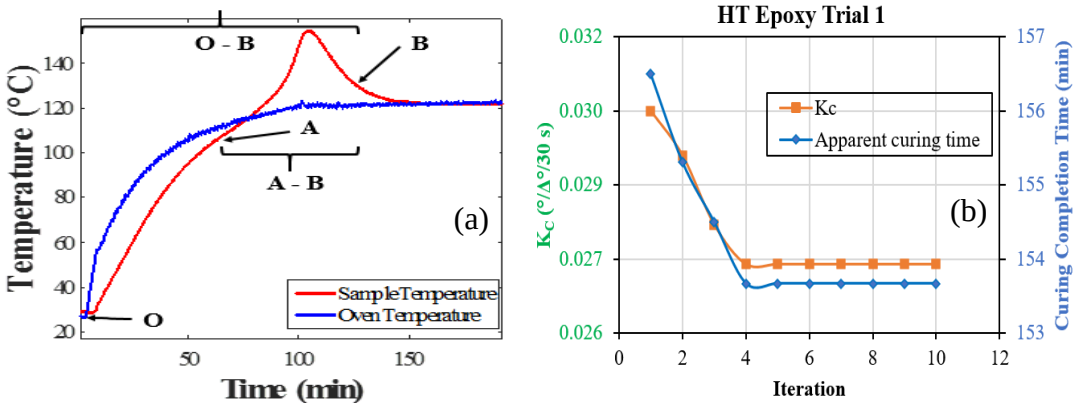

Figure 23: (a) Curing cycle in HT epoxy. O is the start of the experiment, A is the start of the polymerization reaction, and B is the end of the reaction. (b) convergence of K_C for HT epoxy cured at 121 ºC

In the case of the HT epoxy, the time calculated by equation 46 is termed the apparent curing time since the time before the actual start of polymerization reaction is not relevant to the actual time taken by the epoxy system to cure. The actual curing time for the HT epoxy is the time from the beginning of the polymerization reaction to its completion. In this research, that is defined as the time from when the epoxy system achieves 1 % of the total heat to when it reaches 99.8 % of the total heat. Therefore, the start of cure time as determined from equation 45 must be subtracted from the end of cure time determined from equation 46 to get the actual time taken by the higher temperature epoxy to cure. In Table 3, apparent curing time is the time from the beginning of the experiment to the time to reach end of cure (section O-B in Figure 23a). Actual curing time is the time from the start of cure point to the end of cure point (section A-B in Figure 23a). Figure 23b shows the optimization of K_c, using the same techniques as in section 6.4.1. Similar to RT epoxy, K_c is observed to have significant effects on the curing completion time.

Table 3: Start and end of cure for HT epoxy

Trial Number	**Apparent curing time (O-B) (min)**	**Strat of cure (A) (min)**	**Actual curing time (A-B) (min)**
1	153.67	52.33	101.34
2	147.00	49.50	97.50
3	151.33	48.50	102.83
Average	**150.67**	**50.11**	**100.56**

6.5 Determination of gel point

6.5.1 RT epoxy

Initially, the curing epoxy was a liquid and thus no strain was transferred to the internal optical fiber, in spite of any thermal expansion of the liquid resin. Polymer chains were growing through the crosslinking process, but there was still insufficient interaction between the growing sets of strands to strain the fiber. As the curing reaction progressed, the gel point was reached and strain could be transferred to the fiber through the van der Waals and hydrogen bonds [24] between the epoxy and the glass at the interface.

In a perfect experiment, the axial residual strain curve is determined by equation 35 and there would be zero residual strain until the gel point is reached (Figure 24a). Then there would be positive residual strain as the exothermic reaction heats the sample causing thermal expansion of the epoxy. Partially offsetting this expansion would be chemical curing shrinkage and relaxation from viscoelasticity, so the sensor is strained by the net effect. Eventually, the reaction rate slows and a point with the peak positive residual strain is reached when the heat generated by the exothermic reaction is offset by the heat lost to the ambient environment. From that point the epoxy begins to shrink from both curing and cooling. Figure 24 shows an example of a perfect curve (Figure 24a) as well as actual results from a typical experiment at 70 °C (Figure 24b) as an example.

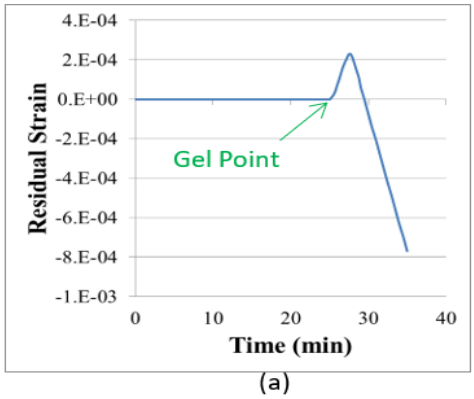

(a)

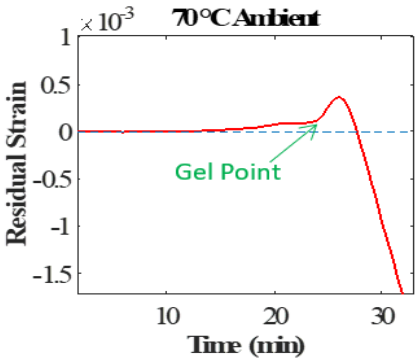

(b)

Figure 24: Expected residual strain curve in a perfect experiment (a) and a typical actual experiment (b)

A method was created in this study to identify the gel point mathematically and overcome the volatility in point-to-point residual strains. First, a moving time series of the slopes of the best fit linear regression of five points on the residual strain curve was calculated from the beginning of the experiment to the peak of the residual strain curve. In other words, the first slope was calculated for the first five points and the next one was calculated for points two through six and so on until the peak point (Figure 25a) was the last point of the five used in the slope calculation. Then, the curvature, κ, at each point was calculated using numerical differentiation and the following numerical adaption of the standard calculus formula for curvature, $\frac{y''}{(1+(y')^2)^{3/2}}$ [119]:

$$\kappa(n) = \frac{\text{Slope}(n+1) - \text{Slope}(n)}{(1 + \text{Slope}(n)^2)^{1.5}} \tag{47}$$

where Slope (n) is the slope of the linear regression of the set of five points. The gel point was selected as the earliest time of the five-point series which has the maximum curvature using this formula.

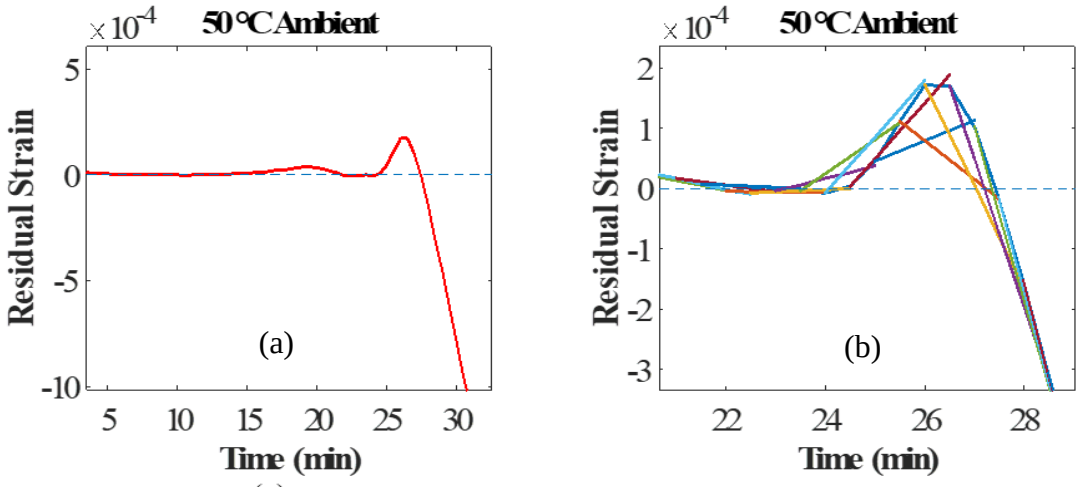

Figure 25: Calculated residual strains point-by-point (a) and zoomed in view with moving average slopes (b)

Initially, it was assumed that simply finding the point at which the moving average slopes became and remained positive would identify the gel point. However, in some samples, such as the 50 °C trial 1 seen in Figure 25a, there seems to be some initial under-compensation of the thermal strains on the optical fiber. This was likely due to the variability of temperature within the sample because of exothermic hot spots [121]. Once the temperature near the FBG sensor started to increase faster than the temperature near the thermocouple, a positive slope was observed, but this was not necessarily the gel point. Thus, the method of seeking a sharp change in the slopes was used and more consistency in the gel point time was observed (see Table 4). As the table indicates, the higher the ambient temperature, the faster the gel/interface point was reached.

Table 4: Gel point times determined by maximum curvature and by Flory-Stockmayer theory for RT epoxy

		Gel Point– Maximum Curvature (min)			Gel Point – 70.7% Degree of Cure (min)		
	Target Temperature	30 °C	50 °C	70 °C	30 °C	50 °C	70 °C
Trial	**1**	43	26	22.5	42	25.5	25.5
	2	34	24	29	39.5	24.5	31
	3	25	29.5	23	42.5	30.5	25.5
	Average	**34**	**26.5**	**24.8**	**41.3**	**26.8**	**27.3**

Table 4 also includes the estimated gel point time using Flory-Stockmayer Theory [62], [63]. Assuming a bi-functional epoxy monomer and a tri-functional curing agent with stoichiometric ratios, the theory predicts that gelation will occur when the square of the probability that each reactive site has bonded equals 0.5, i.e. at a 70.7% DOC [26]. The heat balance approach was therefore used to identify the time at which the DOC, estimated by the left-hand side of equation 43, reaches 70.7%. In eight of the nine trials, there was good agreement between the predicted gel times using Flory-Stockmayer theory and those identified by the maximum curvature approach. In trial 3 for 30 °C, the maximum curvature occurred at a point too early in the process, likely due to under-compensation of the temperature effect. A closer review of the curvature data revealed that the second highest curvature occurred at 45 minutes, close to the 70.7% DOC point.

6.5.2 HT epoxy

The previously developed algorithm in section 6.4 was applied for HT epoxy to compute its gel point. As described previously, the gel point is the time during curing when just enough polymer structure has been built around the FBG sensor for the polymer to

start transferring strain. Up to this point, ideally, the residual strain would be zero. After this point, minimal positive residual strain is observed because of the exothermic heat on the thermal expansion of the polymer. This initial exothermic reaction causes the polymer to expand, leading to a slightly upward profile in the residual strain curve. So, the gel point is calculated as the point when the curvature in this curve is maximum. The computed gel point time from the algorithm was compared to the time from Flory-Stockmayer theory. From Table 5, it is evident that the time calculated from the algorithm is less than 5 % off from the time calculated from Flory-Stockmayer theorem.

Table 5: Gel point times determined by maximum curvature and by Flory-Stockmayer theory for HT epoxy

Trial	**Gel Point– Maximum Curvature (min)**	**Gel Point –70.7% Degree of Cure (min)**
1.00	91.00	87.00
2.00	86.00	82.00
3.00	81.50	78.50
Average	**86.17**	**82.50**

6.6 Residual strains

The equation to determine the residual strain in the embedded FBG fiber has been established before in section 6.1 and is given as:

$$\text{Residual Strain} = \frac{\frac{\Delta\lambda}{\lambda} - \alpha_{\delta}\Delta T}{k} - \alpha_f \Delta T \tag{48}$$

where all the constants and variables are as defined previously.

6.6.1 Residual strain in the FBG sensor embedded in RT epoxy

The residual strains for RT epoxy as calculated using equation 48 and using the data from section 6.2 is shown in Figure 26. The manufacturing strains for this study are defined in section 6.6.3 and are indicated with the arrows in Figure 26. The scatter in the results at each temperature, most likely caused by uneven internal temperature distributions in the samples was evaluated and will be discussed in a subsequent section.

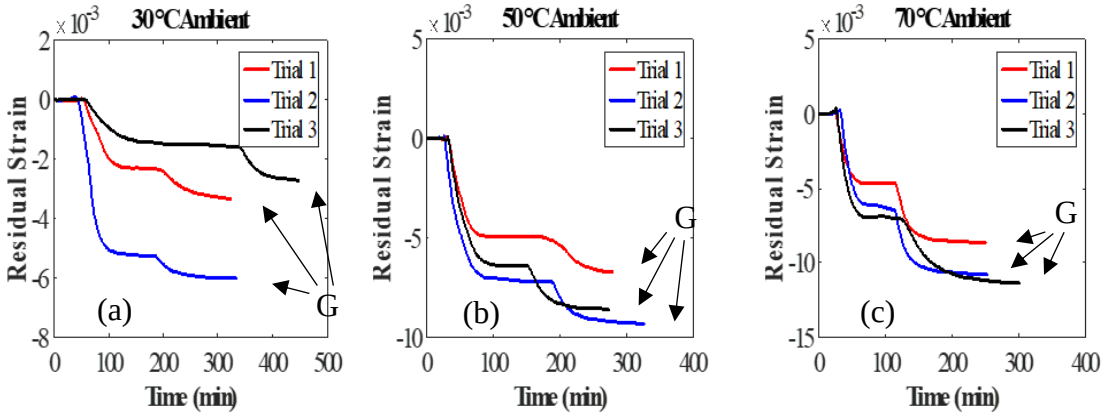

Figure 26: Residual strain profiles of RT epoxy cured at (a) 30 ºC, (b) 50 ºC, and (c) 70 ºC

6.6.2 Residual strain in the FBG sensor embedded in HT epoxy

The raw experimental data (wavelength and temperature profiles) obtained from curing of HT epoxy at 121 C was previously shown in Figure 18. In Figure 27, the calculated residual strain in the embedded FBG sensor from three independent trials are shown. The point G as indicated by the arrows in the Figure 26, and Figure 27 is the end of the experiment (RT).

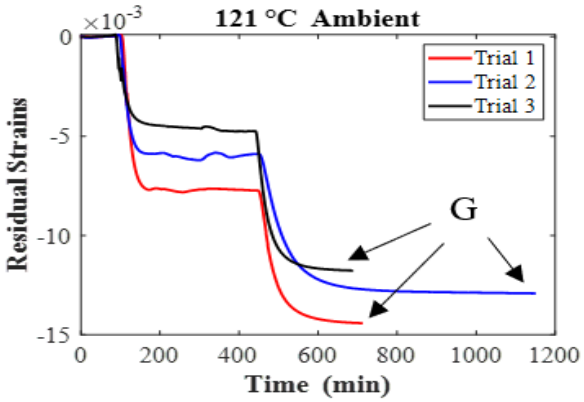

Figure 27: Residual strain profiles of HT epoxy cured at 121 ºC

6.6.3 Curing and manufacturing strains of RT and HT epoxies

Curing strain or the strain at cure is defined for this research as the strain experienced by the FBG sensor at the time of cure completion i.e., when 99.8 % of the curing is complete, even though it includes some cooling strain as the epoxy cools from its peak temperature. Similarly, time to cure and temperature at cure are the time and temperature when 99.8 % of the curing is complete. The approach to calculate those times is discussed in section 6.4.2. Cooling strain for this paper is defined as the difference between the final manufacturing strain and the strains at cure.

Table 6 presents the individual and average curing and manufacturing fiber strains for the RT and HT cure epoxies. For RT epoxy, compressive curing strains ranged from 0.02% to 0.52% while those for the HT epoxy ranged from 0.45% to 0.76%. The compressive cooling strains for HT epoxy was found to be consistent with an average of 0.71% while for RT epoxy the average was 0.28, 0.45, and 0.71 % for 30 ºC, 50 ºC, and 70 ºC cure, respectively. Cooling strains for the second trial of the RT epoxy for 30 ºC cure was observed to be inconsistent with the other two trials. Similarly, for RT epoxy cured at 50

ºC, one of the trials was observed to be inconsistent from the other two trials. For RT epoxy, manufacturing compressive strains ranged from 0.27 % to1.13 % while those for the HT epoxy ranged from 1.17 % to 1.46 %.

Table 6: Summary of key temperatures and strains for RT and HT epoxies

Epoxy type	Target temperature (ºC)	Experiment number	Maximum temperature (ºC)	Temperature at end of cure (ºC)	Strains at end of cure	Cooling strains	Total residual strains
RT	30	1	74.90	55.20	-0.00070	-0.00250	-0.00320
		2	87.40	55.30	-0.00250	-0.00353	-0.00603
		3	67.20	57.71	-0.00020	-0.00250	-0.00270
Average			76.50	56.07	-0.00113	-0.00284	-0.00398
RT	50	1	89.00	67.28	-0.00252	-0.00411	-0.00663
		2	116.20	65.76	-0.00520	-0.00420	-0.00940
		3	126.10	100.79	-0.00237	-0.00623	-0.00860
Average			110.43	77.94	-0.00370	-0.00423	-0.00821
RT	70	1	118.76	82.22	-0.00170	-0.00700	-0.00870
		2	124.50	88.63	-0.00369	-0.00701	-0.01070
		3	112.10	89.98	-0.00433	-0.00690	-0.01123
Average			118.45	86.94	-0.00324	-0.00697	-0.01021
HT	121	1	159.38	121.62	-0.00550	-0.00750	-0.01300
		2	166.08	122.57	-0.00444	-0.00741	-0.01185
		3	154.53	121.84	-0.00560	-0.00732	-0.01292
Average			160.00	122.01	-0.00518	-0.00741	-0.01268

In Table 7 the estimated cooling strains ε_e of RT and HT epoxies are compared with the experimental cooling strains at various curing temperatures. By using the temperature at the end of cure and by using the measured temperature dependent thermal expansion coefficient, the expected experimental cooling strains were calculated including as well as excluding radial strains. Due to the low stiffness of the epoxy, there is a close match between ε_e and the experimental cooling strains regardless of whether the radial strains are included.

Table 7: Comparison of experimental cooling strains [2,3] with the estimated cooling strains for various curing temperatures of RT and HT epoxies

Epoxy type	Target temperature (°C)	Trial number	Temperature at cure (°C)	Estimated cooling strains ($\varepsilon_c=\alpha_m*\Delta T$) ($\varepsilon$)	Experimental axial cooling strains (ε)	
					Including radial strains	Excluding radial strains
RT	30	1	55.20	-0.00241	-0.00258	-0.00250
		2	55.30	-0.00241	-0.00364	-0.00353
		3	57.71	-0.00263	-0.00257	-0.00250
	50	1	69.28	-0.00382	-0.00424	-0.00411
		2	67.76	-0.00367	-0.00433	-0.00420
		3	100.79	-0.00794	-0.00642	-0.00623
	70	1	103.96	-0.00807	-0.00722	-0.00700
		2	89.98	-0.00681	-0.00712	-0.00701
		3	88.62	-0.00667	-0.00701	-0.00690
HT	121	1	121.62	-0.00751	-0.00769	-0.00750
		2	122.57	-0.00753	0.00771	-0.00741
		3	121.84	-0.00759	-0.00759	-0.00733

6.7 Strain scatter analysis in RT and HT epoxies

It is evident from Table 6 that the curing and manufacturing strains increase with higher oven temperatures. It is also observed that the there is significant scatter in curing and manufacturing strains between the three experiments for RT and HT epoxies. To explain the strain scatter, first of all the relationship between the maximum temperature measured and the axial strain was evaluated (see Table 7). It was hypothesized that the higher measured maximum temperature would potentially provide higher axial strains. However, this hypothesis was shown to be challenging to prove as there might have been temperature difference between the TC and the FBG sensor because of their location. The maximum temperature in the curing sample measured by one TC and corelating it to the axial strain measurement did not fully neither prove nor justify the hypothesis. Hence, to try to identify the source of the scatter, several possible sources were investigated as seen the next few subsections: temperature variations between samples, temperature variations within

samples, and the adequacy of stirring of the epoxy and hardener using the amount of stirring time as the variable.

6.7.1 Temperature variations within specimens

Since the maximum temperature in the sample alone failed to explain the scatter in the cure strains, an experiment was designed to investigate if there is any difference in the maximum temperature during curing within the samples. Three thermocouples were embedded at various locations (location 1, location 2, and location 3) inside RT and HT epoxy samples. As before, the experiments were conducted at ambient temperatures of 30 °C and 121 °C for the RT and HT epoxies respectively. In both cases, thermocouple 1 was placed near the center of the mold, while thermocouples 2 and 3 were placed closer to the edges.

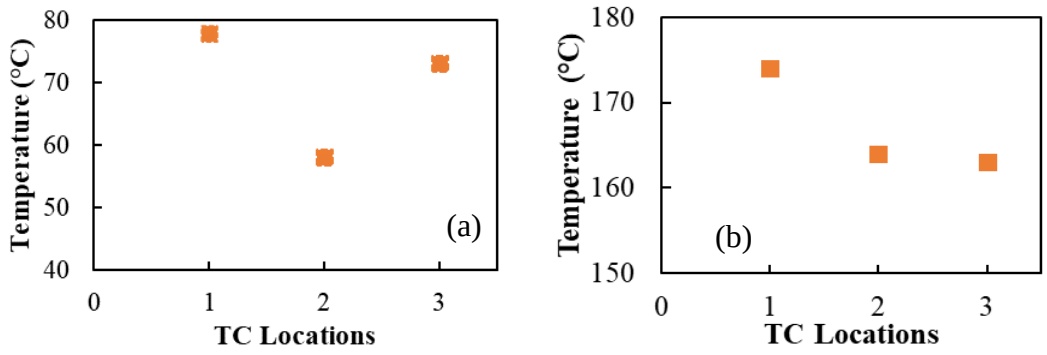

Figure 28: Maximum temperatures from three TCs embedded inside a single sample (a) for RT epoxy cured at 30 °C and (b) for HT epoxy cured at 121 °C ambient temperatures

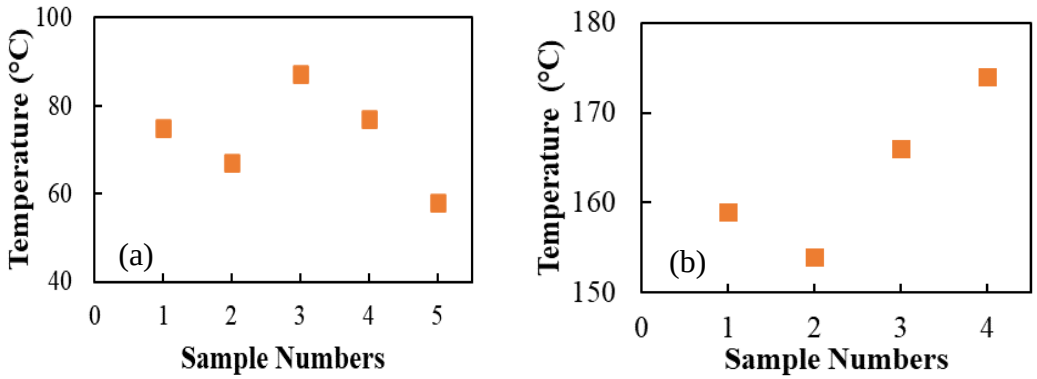

Figure 29: Maximum temperatures measured using TCs embedded (a) inside five distinct samples of a RT epoxy cured at 30 ºC (b) and from four distinct samples for HT epoxy cured at 121 °C ambient temperatures

From this experiment, it is observed (Figure 28a and b) that the maximum temperature inside the curing epoxy is not consistent for either the RT or the HT epoxies. The thermocouple placed in the middle of the specimen recorded higher temperatures than those away from the center. Further from the center, heat is lost more quickly to the ambient environment. Additionally, variation in maximum temperatures could be significantly impacted by non-uniform cure kinetics which result in a heterogeneous exothermic reaction. This could be due to localized hot spots or because of uneven mixing of the hardener and resin. A local increase in temperature accelerates the local curing process which further speeds up the exothermic reaction. It is also possible that an imperfect stoichiometric proportion of hardener and resin could lead to different reaction rates and thus different maximum temperatures between samples.

As seen in Figure 28a, and Figure 28b, the temperature variation within a single sample for both RT and HT epoxies are quite significant (as much as 20 °C). Thus, it is possible

that the scatter in the strains at full cure between the samples could be because the local temperature at the FBG sensor is different from the temperature measured at the thermocouple. An embedded FBG would experience a different thermal field depending on the location of this sensor, concentration of cure agent, etc. For example, an FBG sensor placed in location 1 (Figure 28a) would experience a different temperature profile over time than the one placed at location 2 or 3. This might lead to over or under compensation for temperature and variation in the calculated strains at full cure.

This variation could be even larger between the samples as there are a greater number of variables to be controlled. Maximum temperature during curing of five RT and four HT samples at ambient oven temperatures of 30 °C and 121 °C respectively was compared to determine if there is any variation in maximum temperature attained by the epoxy system. Figure 29a shows that the variation in maximum temperatures recorded between the RT epoxy samples is even higher than the maximum temperature difference within the samples (Figure 28a). For example, the difference in maximum temperature within a single RT epoxy sample cured at 30 °C is found to be about 20 °C while the difference across five distinct samples was as high as 29 °C.

Similarly, maximum temperature difference across four samples for HT epoxy cured at 121 °C (Figure 29b) was found to be greater than within a single HT sample (Figure 29a). These differences for both types of epoxies could be due to non-uniform cure kinetics, uneven mixing, non-exact epoxy/hardener ratios, and placement of the FBG sensors and thermocouples.

6.7.2 Strain variations within specimens

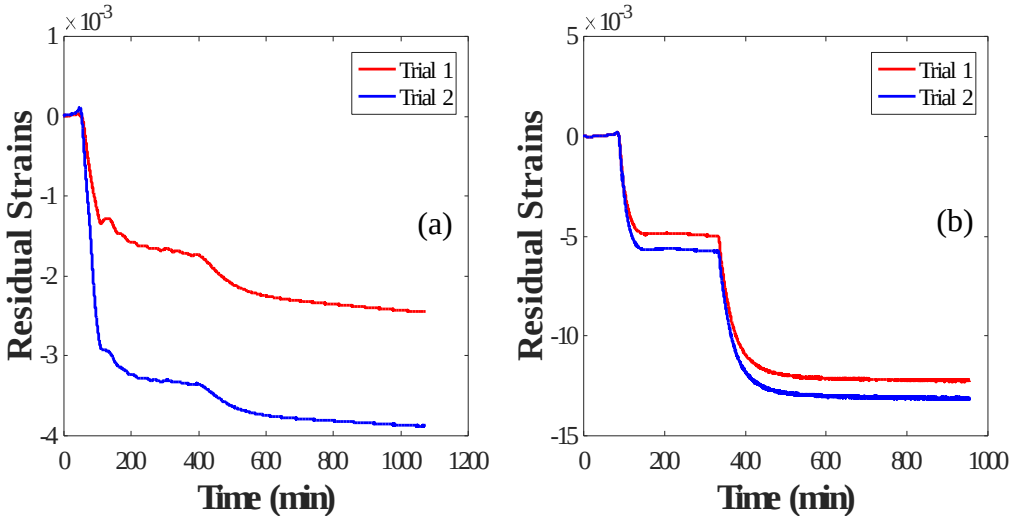

Figure 30: Strain variations in RT (a) and HT (b) individual epoxy specimens

To support the hypothesis that the variation in the temperature field within and between the samples is the reason for the variation in the strains at full cure, an experiment was performed with two FBG sensors and a thermocouple embedded inside each of two samples, one for the RT (cured at 30 ºC) and one for the HT epoxies (cured at 121 ºC). The computed residual strains from this experiment are presented in Figure 30a and Figure 30b for RT and HT epoxies respectively. The residual strains for both FBGs in each sample are calculated based on the same thermocouple reading. As can be seen in Figure 30a and Figure 30b, the final manufacturing strains measured by two FBGs are significantly different for both RT and HT epoxies. The final manufacturing strains obtained from two FBG sensors for RT epoxy are -0.25 % and -0.39 %. Similarly, the manufacturing strains from the two FBGs for the HT epoxy are -1.23% and -1.32%.

6.7.3 Stirring time effect on temperature scatters

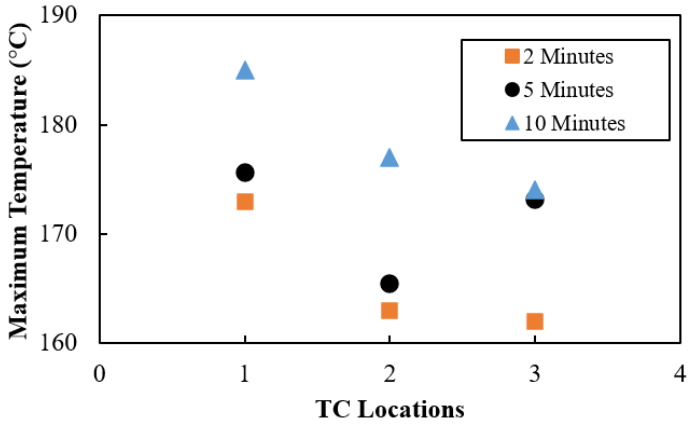

Figure 31: Maximum temperatures during curing from three TCs each time embedded in three different HT epoxy specimens stirred for 2, 5 and 10 min before curing

In order to observe if the stirring time of the epoxy and hardener was inadequate to fully mix the epoxy and hardener and therefore leading to the localized hotspots, additional experiments were performed on the high temperature epoxy with 2, 5, and 10 minutes of stirring. The stirring for all experiments was performed manually with a wooden stick. As shown in Figure 31, the increase in the stirring time did not reduce the scatter in the temperature distribution across various locations in the same sample.

6.7.4 Discussion of scatter analyses

These experiments illustrate that there exist significant temperature differences within a sample based on the location of the sensors. The temperature variations between samples were even larger. The strain variations within epoxy samples for both RT and HT were also significant. Additional stirring time did not reduce the temperature scatter. Based on the results of these analyses, it is believed that the strain variations are due to temperature variations within the samples leading to both actual residual strain differences and to

imperfect temperature compensation of the FBG sensors. Thus, due to the heterogeneous nature of the curing reaction, there will be significant scatter in actual curing and manufacturing strains, even under the same curing conditions.

6.8 Residual Stresses

In this section, residual manufacturing stresses in the fiber and in the matrix were determined. Residual stress in the fiber was calculated using Hooke' law as the final manufacturing strain in the fiber is known from the experiment and the stiffness property of the fiber does not change significantly in the temperature range studied in this research. The determination of residual manufacturing stresses in the matrix of a single fiber composite however is not straightforward as the matrix goes through viscoelastic changes, CTE changes, T_g, modulus changes etc. By using a combination of a single fiber thermal linear elastic model and the Eshleby approach, the matrix stresses were estimated. The details are provided below.

6.8.1 Total stresses in FBG fibers

The residual axial strains in the fiber of a single fiber PMC can be easily obtained from FBG measurements using equation 48 (see Figure 26, and Figure 27). Then, the total axial residual stresses in the fibers can be determined by multiplying the total residual strain in each fiber by the stiffness of the fiber. Using 73 GPa as the Young's modulus of the FBG fiber and the average fiber residual strain of the three trials for each curing condition, the total residual stresses in the fibers were calculated (see Table 8). It should be mentioned that these stresses have two main components: the residual curing stress at the moment

when curing is completed (as determined by the heat balance algorithm in section 6.4.2) and the residual stress due to cooling from the end of curing to the end of the manufacturing cycle. The curing stress can be obtained directly from the curing strain at the point of the end of curing (Figure 19) and includes both chemical shrinkage and some thermal shrinkage as the temperature moves from its peak to the temperature at the end of curing. The cooling stress can be obtained by subtracting the curing stress from the total residual stress calculated at the end of the manufacturing cycle.

Table 8: Average axial residual strains and stresses in the FBG fiber due to curing and cooling during manufacturing for RT and HT epoxies cured at various temperatures

Epoxy type	Target temperature (°C)	Experiment number	Curing strains	Cooling strains	Total residual strains	Curing stress (MPa)	Cooling stress (MPa)	Total residual stress (MPa)
RT	30	1	-0.00070	-0.00250	-0.00320	-51.10	-182.50	-233.60
		2	-0.00250	-0.00353	-0.00603	-182.50	-257.69	-440.19
		3	-0.00020	-0.00250	-0.00270	-14.60	-182.50	-197.10
RT	50	1	-0.00252	-0.00411	-0.00663	-183.96	-300.03	-483.99
		2	-0.00520	-0.00420	-0.00940	-379.60	-306.60	-686.20
		3	-0.00237	-0.00623	-0.00860	-173.01	-454.79	-627.80
RT	70	1	-0.00170	-0.00700	-0.00870	-124.10	-511.00	-635.10
		2	-0.00369	-0.00701	-0.01070	-269.37	-511.73	-781.10
		3	-0.00433	-0.00720	-0.01153	-316.09	-525.60	-841.69
HT	121	1	-0.00550	-0.00750	-0.01300	-401.50	-547.50	-949.00
		2	-0.00444	-0.00741	-0.01185	-324.12	-540.93	-865.05
		3	-0.00560	-0.00732	-0.01292	-408.80	-534.36	-943.16

6.8.2 Determination of thermal stresses in a single fiber composite

6.8.2.1 Single fiber stress model

To fully understand the interactions between single FBG sensors and polymer matrices in the monitoring processes of thermal strains and stresses, single fiber stress analyses must be first performed. They are needed to evaluate the FBG fiber/thermocouple interactions

(as calculated in chapter 2), to identify the effects of the elastic properties of the matrix on the strain in the fiber, and to independently verify the methodology of calculating residual stresses. These tasks are accomplished in this section by performing both analytical and numerical single fiber stress analyses as presented below.

Both the curing process and the associated thermal contractions lead to stress free transformations of a matrix material provided there are no tractions and assuming homogeneous reactions. With an embedded single fiber, however, residual stresses are formed due to the mismatch of the CTEs and the curing shrinkage. To determine the residual stresses throughout the matrix material, a model is needed. For this work, a linear elastic analytical model based on thermal expansions was developed and confirmed by a FE model, which was also used to evaluate other parameters of the experimental design.

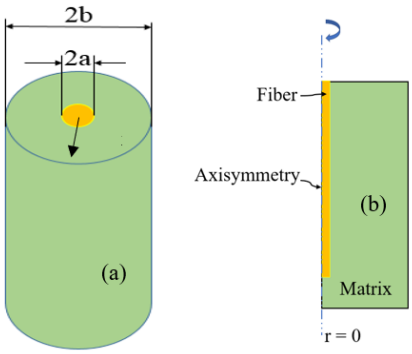

Figure 32: Single fiber composite model (a) and FEM representation (b)

The single glass fiber/epoxy composite is simulated by two infinitely long, concentric circular cylinders, as shown in Figure 32a. The fiber is assumed to be a solid cylinder with outer radius a, while the matrix has inner radius a, and outer radius b. The fiber and matrix both are assumed to be isotropic and linearly elastic. With the assumption of the generalized plane strain condition where the strain in the axial direction is set to be an unknown

constant, the analytical solution of the stress components can be derived. The formulations are shown below, where the subscripts f and m are used to identify the fiber and matrix parameters, respectively. A 2D axisymmetric FE model (see Figure 32b) was used to verify the theoretical model. The mechanical, geometrical, and thermal properties of the fiber and the matrix can be found in Table 1. The ratio of the epoxy diameter to the fiber diameter (b/a) was 120.

The general elastic solution for a thin cylindrical pressure vessel [36], [116] can be modified to fit into the single fiber composite model. The governing equations after considering the theory of superpositions can be expressed as:

For fiber (0<r<a)

$$\sigma_{rr} = -\frac{(3-2v_f)*\rho*\Omega^2*r^2}{8(1-v_f)} - \frac{E_f\alpha_f\Delta T_f}{(1-v_f)*r^2}\int_0^r r'dr' + \frac{E_f*A1_f}{(1+v_f)(1-2v_f)} - \frac{E_f*B2_f}{(1+v_f)*r^2} \quad (49)$$

$$\sigma_{\theta\theta} = -\frac{(3-2v_f)*\rho*\Omega^2*r^2}{8(1-v_f)} - \frac{E_f\alpha_f\Delta T_f}{(1-v_f)*r^2}\int_0^r r'dr' + \frac{E_f*A1_f}{(1+v_f)(1-2v_f)} + \frac{E_f*B2_f}{(1+v_f)*r^2} \quad (50)$$

$$u_r = -\frac{(1-2v_f)(1+v_f)*\rho*\Omega^2*r^3}{8(1-v_f)} + \frac{\alpha_f(1+v_f)\Delta T_f}{(1-v_f)*r}\int_0^r r'dr' - \frac{A1_f*(1-2v_f)(1+v_f)r}{E_f} - \frac{(1+v_f)B2_f}{r*E_f} \quad (51)$$

$$\sigma_{zz} = -v_f(\sigma_{rr}+\sigma_{\theta\theta}) - E_f\Delta\alpha\Delta T \quad (52)$$

For matrix (a<r<b)

$$\sigma_{rr} = -\frac{(3-2v_m)*\rho*\Omega^2*r^2}{8(1-v_m)} - \frac{E_m\alpha_m\Delta T_m}{(1-v_m)*r^2}\int_a^r r'dr' + \frac{E_m\,A1_m}{(1+v_m)(1-2v_m)} - \frac{E_m*\,B2_m}{(1+v_m)*r^2} \quad (53)$$

$$\sigma_{\theta\theta} = -\frac{(3-2v_m)*\rho*\Omega^2*r^2}{8(1-v_m)} - \frac{E_m\alpha_m\Delta T_m}{(1-v_m)*r^2}\int_a^r r'dr' + \frac{E_m\,A1_m}{(1+v_m)(1-2v_m)} + \frac{E_m*\,B2_m}{(1+v_m)*r^2} \quad (54)$$

$$u_r = -\frac{(1-2v_m)(1+v_m)*\rho*\Omega^2*r^3}{8(1-v_m)} + \frac{\alpha_m(1+v_m)\Delta T_m}{(1-v_m)*r}\int_a^r r'dr' - \frac{A1_f*(1-2v_m)(1+v_m)r}{E_m} - \frac{(1+v_m)B2_m}{r*E_m} \quad (55)$$

$$\sigma_{zz} = -v_m(\sigma_{rr}+\sigma_{\theta\theta}) - E_m\Delta\alpha\Delta T \quad (56)$$

where, ν, E, α, Δα, ρ, T are the Poisson's ratio, Young's modulus, CTE, difference in CTE between matrix and fiber, density and temperature, respectively. The subscripts 'm' and 'f' are for matrix and fiber, respectively. Similarly, u_r is the radial displacements and σ_{rr} , $\sigma_{\theta\theta}$, σ_{zz} are the radial, hoop, and the axial stress respectively. Further, $A1_f$, $B2_f$, $A1_m$ and $B2_m$ are constants to be determined.

The loading conditions are as follows:

i. No rotation. i.e. $\Omega = 0$

ii. $\Delta T_f = \Delta T_m = \Delta T$

The general soultion reduces to:

For fiber (0<r<a)

$$\sigma_{rr} = -\frac{E_f \alpha_f \Delta T}{2(1-\nu_f)} + \frac{E_f A1_f}{(1+\nu_f)(1-2\nu_f)} - \frac{E_f B2_f}{(1+\nu_f) * r^2}$$

$$\sigma_{\theta\theta} = -\frac{E_f \alpha_f \Delta T}{2(1-\nu_f)} + \frac{E_f A1_f}{(1+\nu_f)(1-2\nu_f)} + \frac{E_f B2_f}{(1+\nu_f) * r^2}$$

$$u_r = \frac{\alpha_f (1+\nu_f)\Delta T\, r}{(1-\nu_f) r} - \frac{A1_f (1-2\nu_f)(1+\nu_f) r}{E_f} - \frac{(1+\nu_f) B2_f}{r E_f}$$

For matrix (a<r<b)

$$\sigma_{rr} = -\frac{E_m \alpha_m \Delta T\,(r^2 - a^2)}{2(1-\nu_m)} + \frac{E_m A1_m}{(1+\nu_m)(1-2\nu_m)} - \frac{E_m B2_m}{(1+\nu_m) r^2}$$

$$\sigma_{\theta\theta} = -\frac{E_m \alpha_m \Delta T\,(r^2 - a^2)}{2(1-\nu_m)} + \frac{E_m A1_m}{(1+\nu_m)(1-2\nu_m)} + \frac{E_m B2_m}{(1+\nu_m) r^2}$$

$$u_r = \frac{\alpha_m (1+\nu_m)\Delta T\,(r^2 - a^2)}{2(1-\nu_m) r} - \frac{A1_m (1-2\nu_m)(1+\nu_m) r}{E_m} - \frac{(1+\nu_m) B2_m}{r E_m}$$

The boundary conditions are as follows:

i. Stress must be bounded to preserve continuity, i.e., $B2_f = 0$.

ii. Outer boundary is free of traction i.e. $\sigma_{rr\,(r)} = 0$ at r = b

iii. Radial displacemnts at the interface between the fiber and the matrix is continuous. i.e $[u_{r\,(r)}]^f = [u_{r\,(r)}]^m$ at r = a

iv. The radial stress at the interface is equal. i.e $[\sigma_{rr\,(r)}]^f = [\sigma_{rr\,(r)}]^m$ at r=a

There are four equations, four unknowns, and four boundary conditions, hence the constants $A1_f$, $B2_f$, $A1_m$ and $B2_m$ can be found. The constants are:

$B2_f = 0$

$$B2_m = \frac{A1_m b^2}{(1-2v_m)} - \frac{\alpha_m \Delta T(1+v_m)(b^2-a^2)}{2(1-v_m)}$$

$$A1_f = \frac{A1_m E_m\,(1+v_f)(1-2v_f)(a^2-b^2)}{E_f(1+v_m)(1-2v_m)a^2} + \frac{\Delta T\alpha_f\,(1+v_f)(1-2v_f)}{(1-2v_f)} + \frac{E_m \Delta T\alpha_m\,(1+v_f)(1-2v_f)(b^2-a^2)}{2E_f(1-v_m)a^2}$$

$$A1_m = \frac{p}{q}$$

Where, p and q are given as:

$$p = \frac{\alpha_f \Delta T}{(1-v_f)}\left[\frac{(1+v_f)}{2} - \frac{(v_f-v_m)}{\frac{E_m(b^2-a^2)}{E_f a^2}+1}\right] + \frac{\alpha_m \Delta T(b^2-a^2)}{a^2(1-v_m)}\left[\frac{(1+v_m)}{2} - \frac{(v_f-v_m)\frac{E_m}{E_f}}{\frac{E_m(b^2-a^2)}{E_f a^2}+1}\right] + \left[\frac{E_m \Delta T\alpha_m\,(1+v_f)(1-2v_f)(b^2-a^2)}{2E_f(1-v_m)a^2} + \frac{\Delta T\alpha_f\,(1+v_f)(1-2v_f)}{2(1-v_f)}\right] * \left[\frac{2v_f(v_f-v_m)}{\left\{\frac{E_m(b^2-a^2)}{E_f a^2}+1\right\}(1+v_f)(1-2v_f)}+1\right]$$

$$q = \frac{E_m\,(1+v_f)(1-2v_f)(b^2-a^2)}{E_f(1+v_m)(1-2v_m)a^2}\left[\frac{2v_f(v_f-v_m)}{\left\{\frac{E_m(b^2-a^2)}{E_f a^2}+1\right\}(1+v_f)(1-2v_f)}+1\right]$$

$$+\frac{a^2(1-2v_m)+b^2}{a^2(1-2v_m)}-\frac{2E_m v_m(v_f-v_m)(b^2-a^2)}{\left\{\frac{E_m(b^2-a^2)}{E_f a^2}+1\right\}(1+v_m)(1-2v_m)E_f}$$

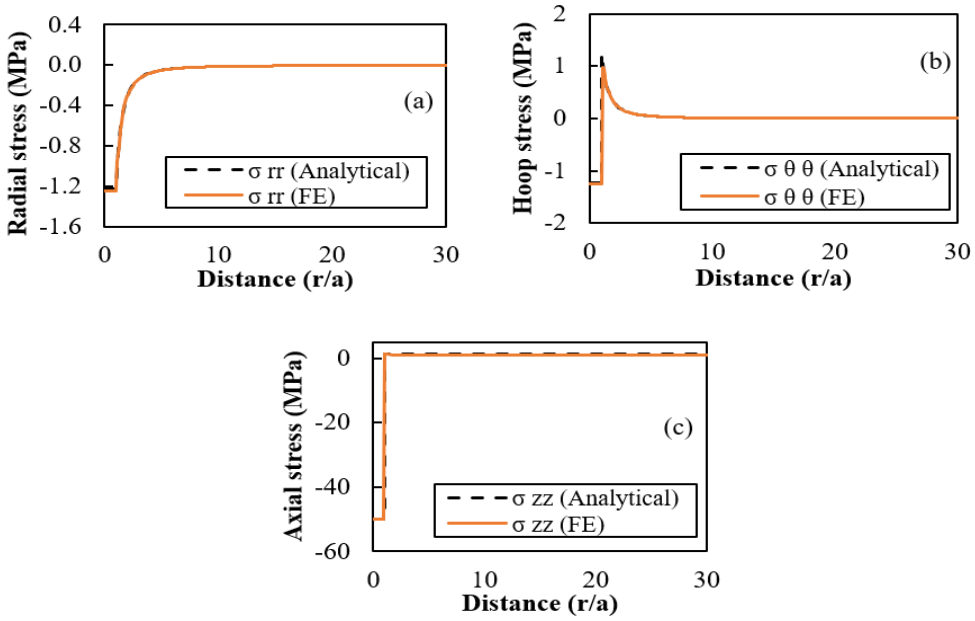

Figure 33: Residual stress as a function of distance (r/a): radial stress (a), hoop stress (b), and axial stress (c)

The single fiber/matrix assembly was subjected to an arbitrary thermal loading of -10 °C. The results obtained from the analytical model and the FE model are shown in Figure 33a, Figure 33b, and Figure 33c for the radial, hoop, and axial stresses respectively. The residual stresses were plotted as a function of the radial distance (r/a). The analytical and FE results agree with each other very well, confirming the validity of the theoretical model.

As shown in Figure 33a, the radial residual stress is constant compressive in the fiber and diminishes in magnitude as a function of diameter in the matrix. The hoop stress is

constant compressive in the fiber, reverses sign in the matrix at the interface and diminishes as r increases. The concentration of hoop stress at the fiber-matrix interface region (see Figure 33b) is likely due to the abrupt change in the fiber-matrix properties. Figure 33c shows the axial stress is compressive in the fiber and tensile in the matrix and almost constant in both cases.

6.8.3 Comparison between measured and predicted cooling FBG fiber stresses

The numerical verification of the total residual stresses in FBG fibers is not a straightforward process due to complex thermal and chemical processes which occurred in the beginning of the manufacturing cycle until the actual curing was completed. However, if the cooling section of the manufacturing cycle is considered from the end of curing to RT, relatively straightforward predictions can be made under certain simplifying assumptions using the single fiber stress models (Section 6.8.2). Also, if the CTEs of the resin as a function of temperature are known, they can be used to predict the residual cooling axial stresses in the fiber in a piecewise manner. Subsequently, the axial cooling stresses in the fiber from the FBG measurements can be compared with these predicted axial stresses.

As examples, for each ambient curing temperature, the experimental axial stress for all the RT and HT epoxy samples from curing completion temperature is plotted along with the numerical calculation in Figure 34 a-d. The cure completion sample temperatures for all the trials were presented in Table 6. In the stress predictions, the CTEs of the epoxy at different temperature ranges as measured in a dilatometer were used. It can be relatively easily shown by performing FE computations or by using micromechanics [36] that the

effect of the elastic properties of the matrix on the Bragg shift (Δλ) and the axial strain in the fiber is negligible for large fiber aspect ratios (larger than 150) and for large ratios of the matrix/fiber diameters (greater than 100). Therefore, the elastic properties of the matrix were kept constant in this analysis.

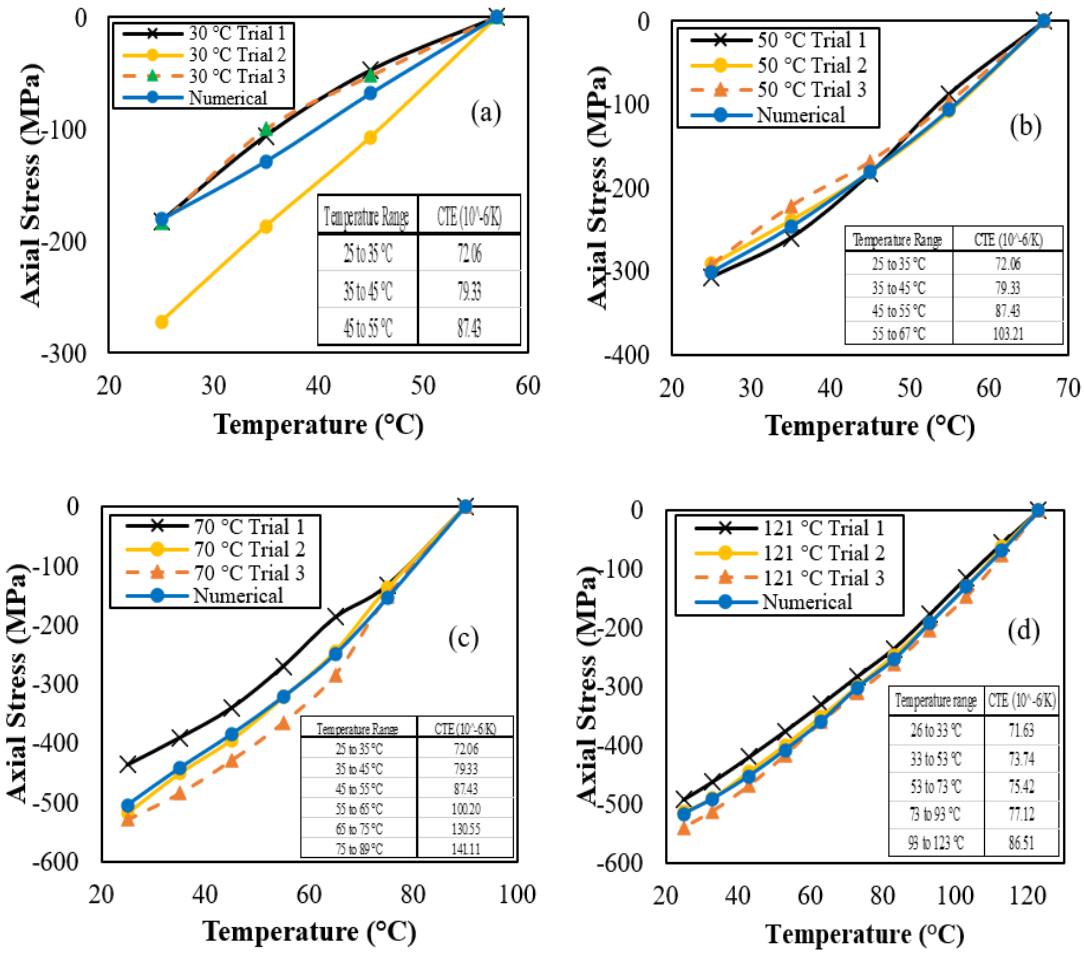

Figure 34: Experimental vs numerical axial residual stress in the fiber for (a) RT epoxy cured at 30 °C (b) RT epoxy cured at 50 °C (c) RT epoxy cured at 70 °C, and (d) HT epoxy cured at 121 °C

The differences in the axial cooling stresses between the experimental and numerical approaches were approximately 5% (see Figure 34a- d) for all temperature intervals.

Importantly, the agreements show that the assumptions of the constant Young's modulus and the constant Poisson's ratio and the actual temperature dependent CTEs in the axial residual stress analysis in the fibers were reasonable. In addition, it can be concluded when analyzing the data in Figure 34 that the effect of viscoelasticity from the end of curing until RT was essentially insignificant since viscoelasticity was not considered in the single fiber models used to obtain the stresses. Of course, almost all of the analyzed cooling for both epoxies occurred below their T_gs which were measured to be 84 °C and 147 °C for the RT and HT epoxies respectively.

6.9 Total manufacturing stresses in the matrix of a single fiber PMC

6.9.1 Key steps of the proposed stress analysis

The new method to determine the residual stresses in the matrix at the end of the manufacturing process of the single FBG fiber composites is based on the following steps:

i. utilize the change in wavelength of the FBG sensor at the end of the manufacturing process to determine the residual strain (ε^{res}) in the fiber (this step has already been accomplished, see Section 6.6)

ii. use the Eshelby approach [27], [34] to determine the far field strain (ε^{ff}) that would produce the measured residual strain in the fiber (ε^{res})

iii. determine an equivalent temperature change ($\Delta T'$) in a single fiber composite system with zero initial stress that would produce the experimental residual strain from step i in the FBG fiber given the results from step ii

iv. apply this temperature change in the thermal stress model for a single fiber (Section 6.8.2) to identify the stresses throughout the matrix including the maximum stresses at the interface.

6.9.2 Determination of far-field strains in a single fiber composite

The Eshelby misfit homogenous inclusion approach [34] can be used to determine the hydrostatic far field strains that would produce the measured residual axial strain (ε^{res}) in the FBG fiber. The required operations for the Eshelby misfit homogeneous inclusion equivalence are provided below.

$$\mathbf{C_f}\left(\varepsilon^{C} + \varepsilon^{ff}\right) = \mathbf{C_m}\left(\varepsilon^{C} - \varepsilon^{T} + \varepsilon^{ff}\right) \tag{57}$$

$$\mathbf{C_f}\left(S\varepsilon^{T} + \varepsilon^{ff}\right) = \mathbf{C_m}\left(S\varepsilon^{T} - \varepsilon^{T} + \varepsilon^{ff}\right) \tag{58}$$

$$\varepsilon^{T} = [\mathbf{C_f}S - \mathbf{C_m}(S - I)]^{-1}\left(\mathbf{C_m}\varepsilon^{ff} - \mathbf{C_f}\varepsilon^{ff}\right) \tag{59}$$

The resultant strains (ε^{res}) measured by the FBG sensor are a combination of the constrained strain (ε^{c}) and the far-field strain (ε^{ff}), i.e.,

$$\varepsilon^{res} = \varepsilon^{C} + \varepsilon^{ff} \tag{60}$$

$$= S\varepsilon^{T} + \varepsilon^{ff}$$

$$= S * [\mathbf{C_f} * S - \mathbf{C_m}(S - I)]^{-1}\left(\mathbf{C_m}\varepsilon^{ff} - \mathbf{C_f}\varepsilon^{ff}\right) + \varepsilon^{ff}$$

$$\varepsilon^{ff} = S[\mathbf{C_f}S - \mathbf{C_m}(S - I)]^{-1}(\mathbf{C_m} - \mathbf{C_f}) + I]^{-1}\varepsilon^{res} \tag{61}$$

where, ε^{c} is the constrained strain, ε^{T} is the transformative strain, ε^{ff} is the applied strain in the epoxy, S is the Eshelby tensor, I is an identity matrix, ε^{res} is the residual strain in the FBG fiber, $\mathbf{C_f}$ is the compliance matrix for the glass fiber, and $\mathbf{C_m}$ is the compliance matrix for the epoxy.

As an example, let us use the fiber axial residual strain (-0.01185, Figure 27 trial 2) measured at the end of the manufacturing cycle of the HT epoxy. For this strain value, Figure 35 shows the axial residual strains in the fiber (ε^{res}) and the axial strain component of the far field hydrostatic strains in the matrix (ε^{ff}) as a function of the aspect ratio of the fiber. For large aspect ratios, both axial strain components are equal. As the aspect ratio of the FBG fiber used in this research was 360, the far-field strain can be set equal to the measured FBG strain.

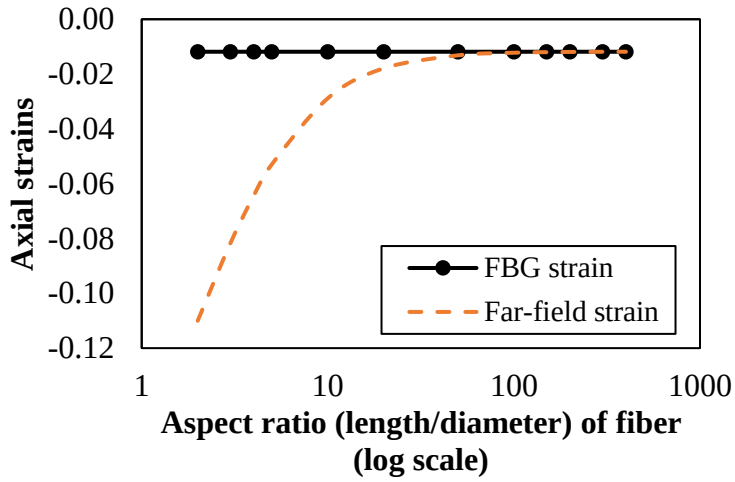

Figure 35: Calculated equivalent axial far-field strain in the matrix and FBG measured axial strain in the fiber as a function of fiber aspect ratio

6.9.3 Manufacturing stresses in the matrix

The far-field strain in the matrix, ε^{ff}, was subsequently used to obtain an equivalent temperature change ($\Delta T'$) in the single fiber composite system that would produce the measured residual strain in the fiber, ε^{res}. Thus, for the axial components of the strains:

$$\varepsilon^{ff} = \varepsilon^{res} = \alpha_m \Delta T' - \alpha_f \Delta T'$$

$$\Delta T' = \frac{\varepsilon^{res}}{\alpha_m - \alpha_f} \quad (62)$$

where α_m is the CTE of the epoxy at RT and α_f is the CTE of the FBG fiber. The equivalent temperature changes for all the curing temperatures for the RT and HT epoxies are listed in Table 9, which were then used in the single fiber stress models presented in Section 6.8.2. The actual profiles of the stresses did not change; however, their magnitudes were affected by the changes to the temperature.

Table 9: Total axial, radial and hoop stresses in the RT and HT epoxy matrices at the fiber/matrix interface

Epoxy type	Target temperature (°C)	Experiment number	Manufacturing strain	Equivalent temperature (°C)	Radial stress (MPa)	Hoop stress (MPa)	Axial stress (MPa)
RT	30	1	-0.00320	45.67	-5.58	5.58	6.40
		2	-0.00600	85.64	-10.46	10.46	12.01
		3	-0.00270	39.11	-4.66	4.66	5.41
	50	1	-0.00670	96.02	-11.51	11.51	13.32
		2	-0.00930	132.74	-16.22	16.22	18.60
		3	-0.00860	122.75	-14.99	14.99	17.21
	70	1	-0.00870	124.17	-15.02	15.02	17.42
		2	-0.01070	153.04	-18.05	18.05	21.41
		3	-0.01130	161.21	-19.55	19.54	22.61
HT	121	1	-0.01290	185.26	-22.26	22.26	25.78
		2	-0.01185	170.21	-20.00	20.00	23.70
		3	-0.01310	188.32	-22.67	22.67	26.20

It can be seen in Table 9 that the matrix stresses increase with the curing temperature. Also for both resins and the four curing temperatures the axial stresses in the matrix were sligthly higher than their corresonding hoop stresses. As expected the radial stresses at the fiber/matrix interface were compressive and equal in magnitude to the hoop stresses. The axial residual stress (25.38 MPa) in the matrix of the HT epoxy was approximately 1/3rd of its tensile strength (71 MPa) [113]. For the RT epoxy for all curing configurations the stresses were between 8 MPa and 20 MPa but could not be credibly compared with the

manufacturer stated strength of the resin (235 MPa), as the reported strength was based on the testing of a glass fiber mat composite rather than the neat resin.

It is very challenging to indepedently verify the stress magnitudes listed in Table 9. However, it might be helpful to note that a system similar to the HT epoxy was investigated by Kim and White [113] who modeled the development of process-induced residual stresses throughout the entire manufacturing cycle of a typical graphite/epoxy composite with a curing temperature of 177 °C. They estimated the axial residual stress in the matrix to be 23.8 MPa.

6.9.4 Contribution of curing to total manufacuring stresses

To separate the contributions of the curing and cooling processes to the total manufacturing matrix stresses, the key steps in Section 6.9.1 were repeated, but using only the fiber cooling strains from the end of cure.

This approach allowed for the calculation of the residual axial stresses in the matrix from cooling only. Table 10 shows the results for the RT and HT epoxies cured at various temperatures. The differences between the total axial stresses in Table 9 and these cooling axial stresses are the curing stresses listed in Table 10. The curing stresses make up about 28% to 48% of the total stresses depending on the resin. These contribution percentages can also be directly determined by finding the ratios of the residual strains or stresses in the fibers at the points of curing to the total manufacturing strains or stresses in the fibers.

It should be emphasized that the curing stresses at the completion of curing would be smaller than the values reported in Table 10 as the stiffness of the epoxies are reduced at higher temperatures. However, the ultimate impact of the residual stresses induced from

the curing process is an important component of the total manufacturing residual stresses in the matrix.

Table 10: Estimation of equivalent temperature change, cooling axial stresses in the matrix, and the stress contribution from curing in the total axial manufacturing stress for RT and HT epoxy systems cured at various temperatures

Epoxy type/Target temperature	Cooling equivalent temperature changes (°C) (ΔT')	Axial stress from cooling only (MPa)	Axial stress contribution from curing (MPa)	Matrix axial curing stress contribution %	Fiber axial curing stress contribution %
RT /30 °C	40.44 ± 6.72	5.67 ± 0.94	2.27 ± 1.97	28.58	28.45
RT /50 °C	60.42 ± 4.09	8.47 ± 0.57	7.93 ± 1.87	48.35	48.41
RT /70 °C	100.22 ± 1.83	14.00 ± 0.16	6.47 ± 2.06	31.59	31.28
HT/121 °C	110.14 ± 2.51	15.21 ± 0.34	10.36 ± 1.41	40.81	40.85

6.10 FBG sensor for aging monitoring

It has been shown that polymers and PMCs will age and will cause flexural and fatigue properties to degrade over time when exposed to high temperatures [120], [121], [122]. Most of the parts made from PMCs are used at elevated temperatures. Various methods [122], [123] have been used by other researchers to monitor aging processes in epoxies and PMCs. This section provides a demonstration of the use of FBG sensors to monitor the aging process of the HT epoxy at high temperatures in air.

The single FBG glass fiber HT epoxy composites were aged in several conditions: below T_g (147 °C) at 130 °C and 140 °C, at (or near) T_g (147 °C) and above T_g at 185°C. These conditions were chosen to produce accelerated aging of the HT epoxy. The highest

temperature of 185 °C was chosen to demonstrate the capability of the FBG sensor to monitor the entire life cycle of a PMC including its potential HT degradation. Hence, 185 ºC aging was carried out for the longest (~ 300 days). The aging was conducted in the atmosphere and not under a vacuum to be more representative of potential in-service conditions. The aging of polymers at high temperatures has been studied before [121]. However, until the time of writing this dissertation, the author was not aware of any experimental or analytical studies involving the aging monitoring of polymers using FBG sensors.

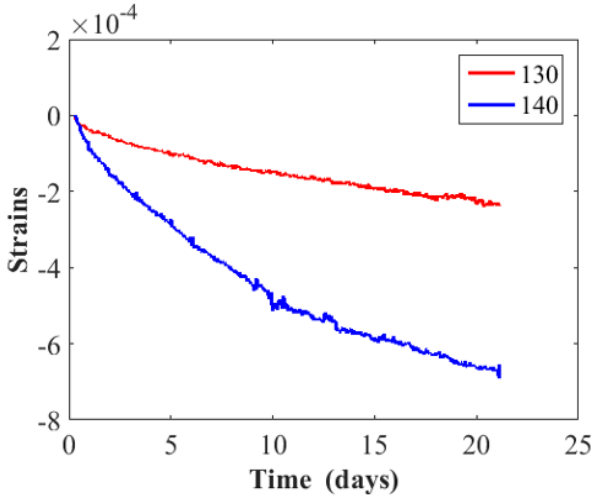

Figure 36: FBG sensor measured axial aging strains in the HT epoxy at 130 ºC and 140 ºC

Except for the 185 °C aging, for each aging condition, specimens were aged for twenty-one days. The aging was performed in a Precision Scientific EconoTherm Laboratory Oven and the specimens were freely suspended from the top of the oven. Figure 36 shows the axial aging strain in the FBG fiber as a function of aging time. It is observed that with an increase in the aging temperature below T_g, physical aging is increased because of the

increased magnitude of the residual strains, and therefore the amount of reduction in the free volume must be greater for 140 ºC than that for 130 ºC aging. This well-known reduction in the free volume increases the magnitude of the residual stresses in the composite. In other words, at higher temperatures but below T_g, the PMCs move to a higher state of stress which weakens the composites and potentially reduces their flexural and other strengths. On a micro-level, the stress may be high enough to create micro-cracks and even fiber-matrix debonding. The debonding of the fibers could lead to a drop in the stiffness of the composite. The increase in the magnitude of the aging strain with the increase in the isothermal aging temperature below T_g agrees with the conclusions of the previous research [121].

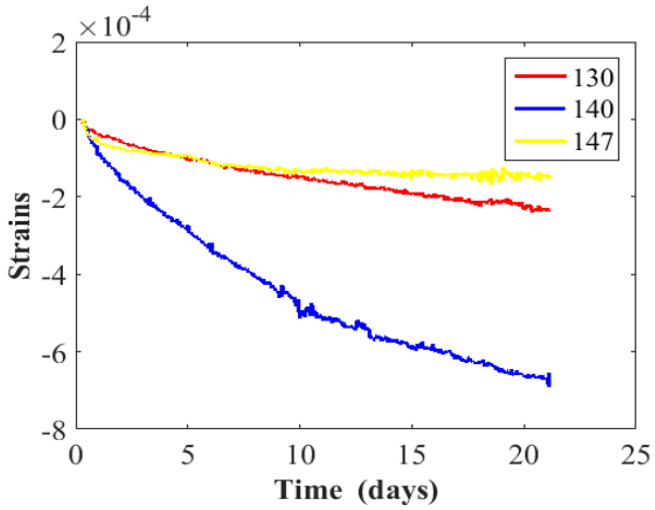

Figure 37: Axial aging strains in the HT epoxy measured by FBG sensors at 147 ºC (near or at T_g) and compared with other aging results (130 ºC and 140 ºC)

Figure 37 shows the comparison of the aging strains near (or at) T_g with the aging results below T_g. Ideally, at T_g, no physical aging is supposed to occur as the molecular configurational change occurs at constant free volume [124]. But the HT epoxy tested at

147 ºC in this research showed some physical aging (compressive strains in the fiber). This could be because this epoxy sample is slightly above the T_g (manufacturer provided a range for T_g from 145 to 149 ºC) and is beginning to undergo chemical aging as the filler materials might have started to evaporate.

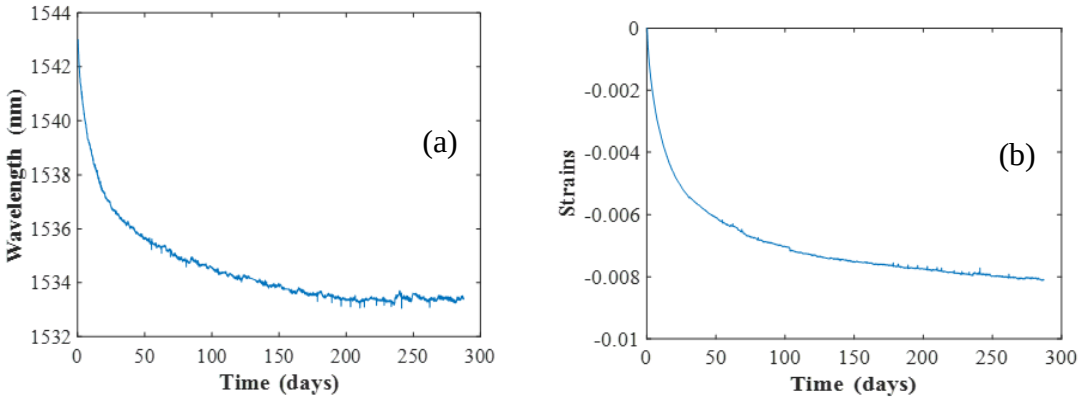

Figure 38: Wavelength (a) and axial strain (b) measurement during aging of HT epoxy

Figure 38 shows the wavelength profiles from the 185 °C aging of the HT epoxy. The axial strain in the FBG fiber during the aging process is shown in Figure 38b. As can be seen, the FBG fiber is being compressed even more in comparison with the lower temperatures during the aging process as the filler materials present in the epoxy are being evaporated (mass loss was observed) because of the high temperature. This causes the epoxy sample to contract further, causing the FBG fiber to be in higher axial compression.

Figure 39 shows a comparison between the FBG measured aging strains with those from a dilatometer. The results from the two independent techniques are comparable. The small difference between the two techniques might be because, in the case of the dilatometer measurements, physical aging and creep are acting in the same direction, while in the case of the FBG measurements, physical aging and creep are competing with each

other. The presence of the stiffer glass fiber in the FBG measurements (not used in the dilatometer) makes it difficult for the resin to act in the same direction as physical aging.

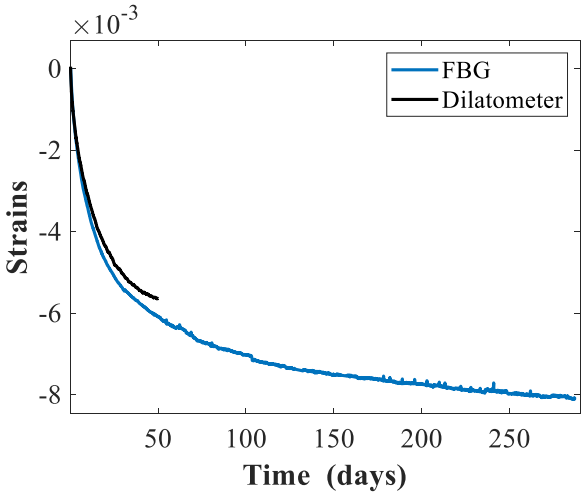

Figure 39: Axial strain comparison during aging of HT epoxy at 185 ºC as measured by an FBG sensor and a dilatometer

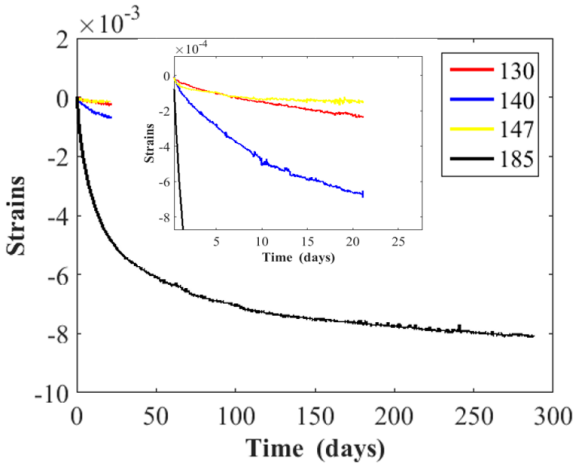

Figure 40: FBG sensor measured aging strains of HT epoxy at below and above T_g

Figure 40 shows the summary of the HT epoxy aging experiment carried out at various temperatures. The physical aging strains observed both below and above the T_g seems to be reasonable. From the experimental demonstration presented in this section, it is evident

that the FBG sensor can be used to monitor the aging process not only in HT epoxy but also in other polymers. Further, the FBG sensor was able to survive the high temperature of 185 ºC for a prolonged period. This demonstrates that embedded FBG sensors in PMCs could continue to provide valuable information during the in-service condition of PMC components even at relatively high temperatures.

6.11 FBG sensor for degradation monitoring

This section demonstrates the application of FBG sensors in the monitoring of extensive degradation processes in single fiber polymer composites. First, a single FBG fiber HT epoxy composite was manufactured following the technique discussed in chapter 4. The composite was then subjected to an extremely high temperature of approximately 575 ºC to drastically accelerate the degradation process.

Figure 41 and Figure 42 show the still un-processed wavelength and temperature profiles from the degradation experiment on the HT epoxy. The detailed features of the curing kinetics have already been discussed in chapter 6. In this section, the emphasis was placed on the heating and degradation of the composite. i.e., between points G and L in Figure 41.

G is the point when the manufactured single fiber composite is put into an oven and heated until complete degradation at 575 ºC. The ambient and the sample temperatures were measured using a TC. As can be seen in Figure 42, during the heating of the sample after the completion of the manufacturing cycle (before point G), the sample temperature exceeds the ambient temperature. This may be caused by the presence of some uncured

epoxy residue in the sample. At the very high temperature above T_g, the leftover uncured epoxy could react with the polymerizing agent and give off heat. Further, the epoxy might be burning at such high temperature resulting in a higher sample temperature than the ambient temperature. During the heating process, the oven door was not opened to check whether the sample was burning or not as this would influence the heating rate. However, a cloud of fumes was observed to be coming out of the oven during the heating process. Further, when the experiment was finished, the FBG sensor was found to be free hanging inside the oven and the traces of ashes of the burnt epoxy were detected at the bottom of the oven. Hence, the assumption that the sample had burned off during testing resulting in higher sample temperatures than that of the ambient is justified.

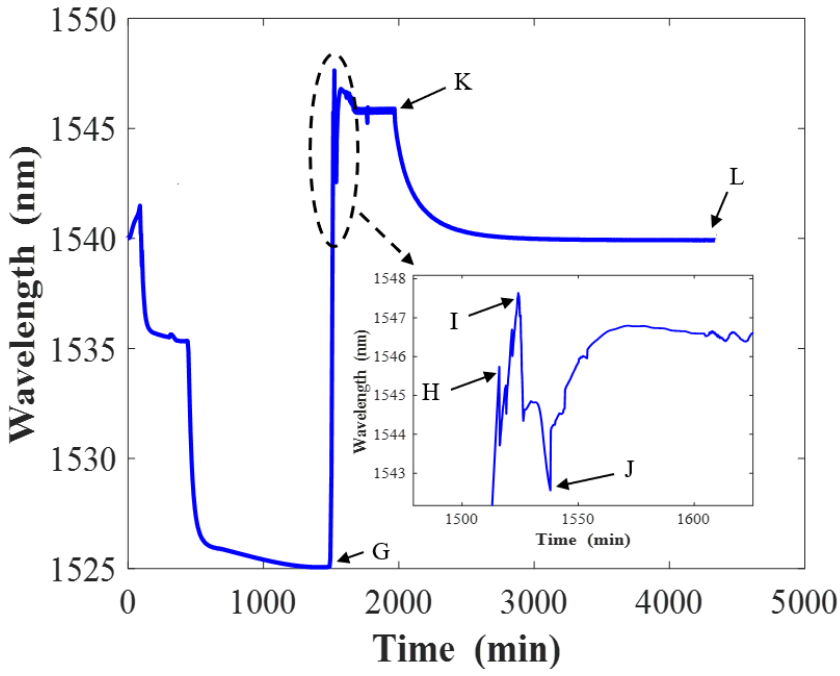

Figure 41: Raw (as received) wavelength data from the degradation experiment on the HT epoxy

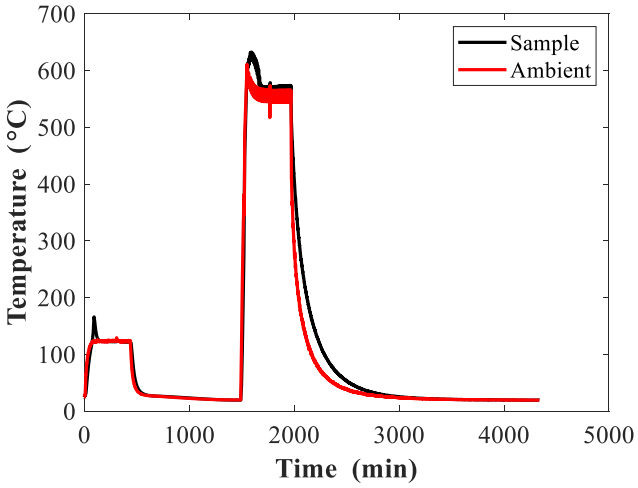

Figure 42: Sample and ambient temperatures from the degradation experiment on the HT epoxy

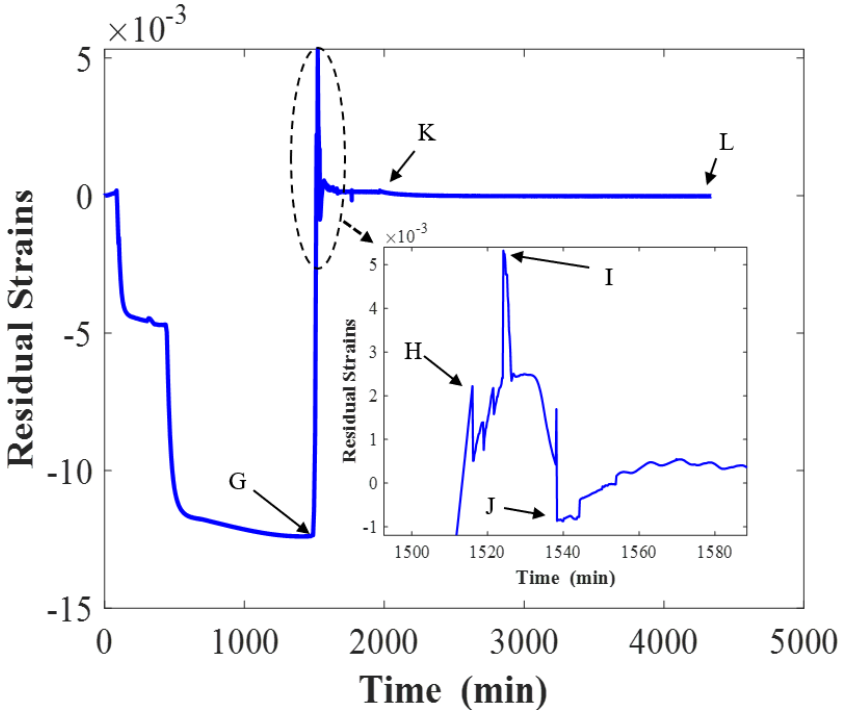

Figure 43: Temperature-compensated axial strains from the degradation experiment on the HT epoxy

Previously, in section 5, it was demonstrated that the FBG glass fiber forms an excellent bond with the tested epoxy. The wavelength profile during the manufacturing as well as during the aging testing were smooth. However, if the degradation of the epoxy and that of the fiber/matrix interface were to occur, then the FBG wavelength profile should no longer be smooth and some anomaly in the wavelength and hence in the strain readings should be observed. Figure 43 shows the zoomed-in view of the residual strain profile. It is known that at such high temperature, the epoxy sample is likely to be very pliable because of a viscoelastic effect, or degradation of the epoxy network and plasticization by degradation products. Because of this, the bonding between the FBG fiber and the epoxy starts to deteriorate. A stick-slip phenomenon can be seen as the FBG fiber is being relaxed and compressed repeatedly from point H. 'H' is the first point when the FBG glass fiber with an excellent bonding with the epoxy starts to show some anomalous behavior. When the wavelengths between point 'H' and point 'I' were compared with the temperature profile, it was observed that the temperature profile was smooth and increasing. That means that the anomaly observed in the FBG sensor measurement was not associated with the temperature profile. Rather it was the result of the anomalous behavior of the epoxy/fiber interface at high temperature. Therefore, it can be confidently stated that ‘H’ is the beginning of some significant degradation of the FBG glass fiber-epoxy interface.

From point 'I' onwards, the degradation of the epoxy rapidly increases and is combined with an occasional stick-slip phenomenon. Point 'J' is the completion of the degradation of the fiber/matrix interface. The rise in the strain after point 'J' is due to the rise in the oven temperature as indicated by the TC. Once the fiber/matrix interface is destroyed, the FBG

fiber is free from any surrounding matrix and is sensitive to the applied temperature only. Hence, once the temperature influence on the FBG measurement was subtracted, the axial residual strain profile became very close to zero (from J through to K to L), as expected.

A very small slope in the residual strain profiles between K and L could be due to a slight difference between the assumed and actual CTE and thermo-optic coefficients used in the strain calculations for this section, as these factors are temperature dependent. However, the residual strain profile being almost zero in this section i.e., after the completion of degradation (from J through K to L), demonstrates that the values used for the CTE and thermo optic coefficients are reasonably accurate. Furthermore, the stripped FBG sensor was able to survive the degradation temperature of 575 ºC, thereby proving that it could be potentially used in the lifecycle monitoring of composite structures at extremely high temperatures where the use of existing monitoring technique might be challenging or even impossible.

In this relatively short section, a novel degradation monitoring method was developed for the first time using the FBG sensors. The experimental results and the analysis presented ~~in~~ here demonstrate that the application of the FBG sensor to monitor the entire life cycle of the polymers and PMCs is possible with very useful aging/degradation data as an outcome.

Summary Observations and Concluding Remarks

Utilizing the algorithms and techniques developed in this research, significant characteristic points can be determined for the investigated room temperature epoxy by the embedded thermocouple and the readings of the internal and external FBG sensors. Figure 44 illustrates schematically the progression of the typical curing cycle from the initial heating to the cooling stage. The schematic exemplifies well the curing curves at three different temperatures. In the initial heating stage between points A and B the oven is turned on and starts to heat up. The optical fiber in this period is undergoing thermal expansion due to sample heating from the oven and the exothermic reaction. There is no residual strain between A and B as the interface is not yet fully built and the gel point has not yet occurred. At B, the gel point is reached, and the interface has been established leading to the commencement of positive residual fiber strains from the thermal expansion of the epoxy. Using the maximum curvature approach the gel point can be accurately determined even if the residual strain curves are over or under compensated for temperature. At C, the maximum temperature and the maximum positive residual strain is reached as the heat generated by the exothermic reaction is equal to the heat dissipated from the sample to the ambient oven environment. Between C and D, the exothermic reaction slows and the sample cools towards the ambient oven temperature. At D, the curing reaction is complete and no more exothermic heat is generated. Point D represents the curing time which can be determined using equation 46. Importantly, many factors can

affect the accuracy of the curing time determination at D, as clearly indicated in this study. The convenient approach of using the combined thermocouple/FBG setup with the iterative calculations of the conductivity factors resulted in an extremely accurate estimation of the curing time indirectly verified by Flory-Stockmayer. Without the proper estimation of the heat balance at the end of cure and the heat conductivity factor, the gel point would not be precisely determined and then successfully compared with the Flory-Stockmayer. After reaching the end of cure, the sample cools towards the ambient oven temperature reached at E, and then between E and F, the sample is held at the oven temperature. At F, the oven is shut off and both the sample and the oven cool towards room temperature which is reached at G. While the gel point at B may be readily apparent by viewing the figure, the techniques developed in section 6 provide mathematical precision. The end of cure at point D is more difficult to isolate without the use of the algorithm from section 6.

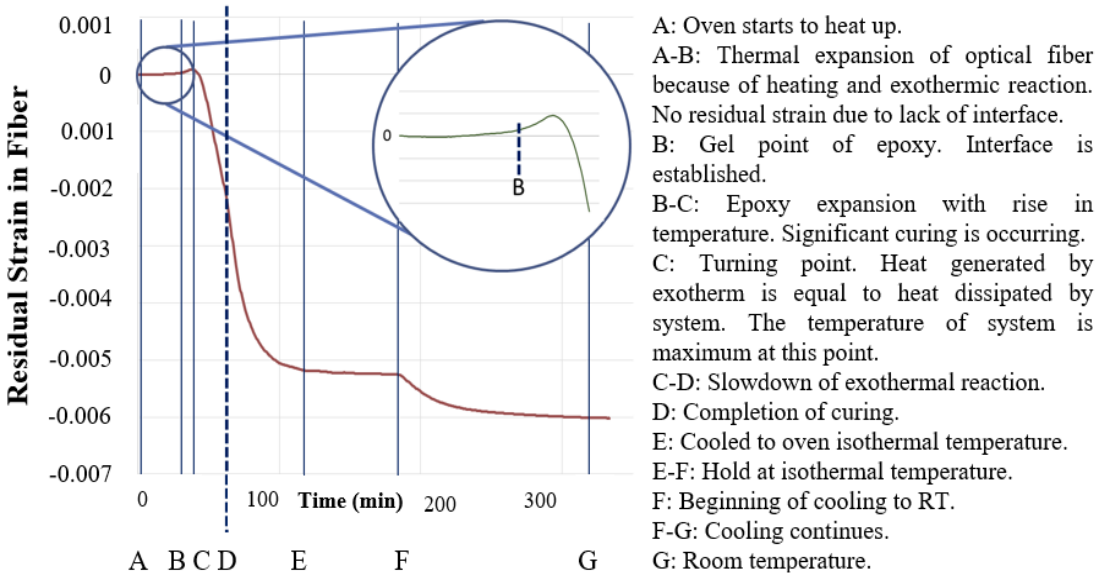

Figure 44: Strain evolution during manufacturing of epoxy-based composites, as displayed by FBG strain

The numerical models developed to identify the gel point and the end cure for a RT epoxy [1] have been successfully applied to and validated with a HT epoxy. The algorithms were extended to detect the start of cure for the HT epoxy, as this does not occur immediately upon mixing of the epoxy and hardener. Flory-Stockmayer theory was utilized to cross-validate the heat balance methods utilized to identify the start and end of cure and to pinpoint the gel point. The differences in the average actual times to reach the gel points determined from the curvature method and Flory-Stockmayer theory were less than 5% for both RT and HT epoxies.

The measured manufacturing strains in the single fiber composites were split into curing strains (those until the end of the curing reaction) and cooling strains (those after the end of cure). The magnitudes of these total manufacturing strains are significantly higher than would be predicted based only on cooling from the ambient curing temperature to RT. The curing strains contributed about 28% and 45% of the total manufacturing strains for the RT and HT epoxies, respectively. The measured cooling strains were found to be very close to their thermal-expansion predictions, especially for the HT epoxy.

The scatter observed in the overall manufacturing strains, which were precisely measured by the FBG sensors, were tied to temperature variations across the curing epoxies. It is important to understand these variations as more complex composites are analyzed. This work demonstrates that a simple test with a single FBG sensor and a thermocouple can provide valuable information about the curing process that could be applied to advanced composite structures.

Further, a novel approach to determine residual stresses in the matrix of a single FBG fiber/matrix composite at the end of the manufacturing cycle using FBG strain measurements is also presented. Using the corresponding residual strains in the fibers and their stiffness properties, the residual axial stresses in the FBG fibers at the end of curing and the end of manufacturing for RT and HT epoxies were measured. The end of curing can be obtained by the combined application of FBGs and thermocouples [1], [2] and by using the algorithm developed in chapter 6. Thus, the cooling stresses from the end of curing to RT could be measured in the FBG fibers. The stresses were subsequently numerically predicted using single fiber/epoxy cylinder models. In the models, the stresses were calculated using the actual temperature dependent CTEs for the matrix, a constant RT CTE for the FBG fiber, and the RT matrix stiffness properties. The errors between the numerical and experimental results were less than 5% for both epoxy systems and all curing conditions.

During the manufacturing process of a single fiber composite, the matrix undergoes many complex and often nonlinear transformations. However, the glass FBG fiber responds linear elastically to all the stresses imparted on it during the curing and cooling processes. Using the residual strains in the fiber as the input, the calculation of the residual stresses in the matrix was performed using an approach that solved for the matrix stresses using equivalent fully linear elastic transformations. This process determined an equivalent temperature change in a stress-free single fiber composite that would produce the measured residual strains in the fiber from the manufacturing process. As part of the process, the

misfit /homogeneous inclusion Eshelby concept was used to identify the far field strains that would produce these residual strains in the fiber.

The residual total stresses in the matrix of both composite types were found to be close to what could be expected for the epoxy systems investigated in this research, in particular, if compared with their strength values. For the HT epoxy system, the axial stress (25 MPa) was close to about one-third of the strength of the resin (71MPa). For the RT system the residual axial stresses increased from about 8 MPa for the curing ambient temperature of 30 °C to about 20 MPa at 70 °C.

In addition to determining the total manufacturing stresses in the matrix, the sources of the stresses were allocated between the curing and the cooling cycles. For the resins and curing temperatures considered, the curing process itself contributed 28 to 48 % of the total residual stress in the matrix. This strongly indicates that the curing portion of the manufacturing process cannot be ignored in the residual stress analysis of PMCs even at relatively low curing temperatures. The magnitudes of the stresses caused by curing and cooling can be obtained using the newly proposed single fiber/Eshelby misfit approach in this work and previously published algorithm [1,2] for the determination of the end of curing. If just the ratios of the stresses are required, a much simpler approach can be used based on the residual strains and stresses measured in the FBG fibers at the end of curing and manufacturing.

Moreover, the FBG sensor was demonstrated to be an effective tool for aging monitoring of epoxy at various temperatures. The physical aging measurements from the FBG sensors are logical and in agreement with the conclusions made by previous

researchers. Additionally, the embedded FBG sensor in a single fiber composite allowed the determination of the start and end of the interface degradation between the fiber and the matrix. Therefore, it can be concluded that the FBG sensor is capable of monitoring the entire life cycle of a composite.

Solidification Monitoring of Tin (Sn)/Bismuth (Bi) Alloys Using FBG Sensors

7.0 Introduction

In the ensuing chapters (chapter 7 to 9) an advanced FBG sensing techniques has been applied to monitor the solidification processes in seven different tin/bismuth alloys. It is shown that the techniques can successfully identify the most characteristic features of different phase transformations in the alloys if the FBG sensors are correctly applied in conjunction with a thermocouple. Tin/Bismuth alloys were chosen for the experimental purpose because of the following reasons: 1) their melting temperature is high enough to be a representative alloy of other high temperature metals/alloys (Aluminum, Steel etc.) but not too high to damage the FBG sensor, 2) tin/bismuth alloys exhibit significantly different physical properties (stiffness, thermal conductivity etc.), 3) the alloys undergo through multiple phase transformations. Hence, the obvious question was whether the FBG sensor can sense these transformations. Further, tin contracts while bismuth expands during solidification making the tin/bismuth solidification process more diverse than most of the metal/alloy systems.

7.1 Solidification

The manufacture of most man-made metallic objects involves the process of solidification at some stage. Solidification is a comprehensive process of transformation of the melt of metals and alloys into a solid, involving nucleation, development of a solid-

liquid interface, formation of crystals and dendrites and their growth, etc. [125], [126], [127], [128]. Above the melting point, the free energy of the liquid is less than that of the solid and thus the liquid is stable above the melting temperature. Below the melting point, the free energy of the liquid becomes higher than that of the solid. Hence, the solid becomes more stable. At the melting point, both the liquid and solid will have equal energy and hence both are equally stable. This means, no crystallization process will occur, i.e., liquid will remain liquid and the solid will remain solid. But the presence of small impurities, or undercooling will act as a nucleating site and the solidification process will begin.

The most important practical applications of the process of solidification are found in processing technologies such as: casting, welding, surface alloying, crystal growth, ingot production, materials purification, refining, etc. Most of these processes involve introducing the liquid metal into a mold under controlled conditions of melting, cooling, etc. to obtain the desired structure [127], [128]. A molten metal has a viscosity which is about only one-twentieth of the corresponding solid [128]. Thus, instead of using high energy to overcome the high flow of stresses of a solid to shape it by adopting bulk metal forming operations such as forging, extrusion, rolling, etc., a liquid metal with essentially zero shear strength is much easier to handle. A detailed study of the process of solidification, therefore, enables one to understand and hence control the microstructure that determines a metal's mechanical and thermal properties.

The process of solidification is accompanied by a very important phenomena which decides the intrinsic properties of the resultant solidified part. At the first instance, freezing in most of the metals/alloys is associated with volume contractions because of the

development of a more closely packed solid [129]. At the same time a reduction in the atomic or molecular motion is experienced when the randomly moving atoms in the liquid phase generate the nuclei that finally grow into the solid phase. Latent heat of crystallization is liberated at the solid/liquid interface. This liberated heat energy significantly affects the rate and mode of crystal growth. The temperature decreases leading to freezing generally causes a lowering of the solubility of the alloying elements in the melt. Solute atoms are ejected at the solid–liquid interface.

Whether the casting, welding, alloying, refining processes are the last stage of fabrication or need be followed by further mechanical working, solidification processes play an important role in deciding the microstructure of the product and hence its final structure related properties.

7.1.1 Solidification monitoring

The solidified microstructure is the bridge connecting the composition and properties of alloys. An accurate understanding of the formation mechanisms, governing factors, and control approaches of solidification of alloys are conducive to the precise control and design of microstructures to improve the comprehensive properties of materials and optimize the performance of alloys [125]. However, due to the opacity and micro-nanoscale size of the solidification structure and the high-temperature environment during solidification, traditional characterization techniques such as metallographic microscopic observation, rapid quenching, and molten liquid dumping cannot be used to observe the whole solidification process dynamically, completely, and in real time. As a result, some crucial information about the solidification process can be missing.

Significant advancements have been made to the traditional microscopic solidification characterization technique [130], [131], [132], [133], [134], [135]. Various experimental and computer simulation-based techniques have been developed to monitor the solidification process of metals/alloys [136], [137], [138], [139], [140], [141], [142], [143], [144], [145], [146], [147], [148], [149], [150]. Thermal analysis techniques monitor temperature changes in a sample as it cools through a phase transformation interval. The use of thermal analysis techniques to study the solidification of aluminum dates back to laboratory studies conducted 40-50 years ago, but the procedure has found extensive commercial application in the last two decades, when foundrymen found the techniques useful for checking the microstructure [129] of aluminum alloys before they were cast. Over time, these techniques have continually progressed. Normally, differential thermal analysis (DTA) [125], [130] is used for thermal analysis of solidification. In DTA, heat evolved or absorbed due to a phase transformation can be calculated from the difference of thermal events in the sample versus a neutral reference; however, the DTA apparatus is expensive and complicated, and it is not feasible for use on a foundry floor. Hence, a simpler approach is necessary to obtain the cooling curve data of a solidifying sample with the help of thermocouples. Data obtained from the TC can be analyzed to understand various phase transformation characteristics [130], [131].

One of the techniques for monitoring the solidification process is cooling curve analysis [134]. It is used to analyze the microstructural changes and evaluate the fraction of solid. Using this technique, time and temperature were recorded under different cooling rates

[134]. The information thus generated can be used in a quantitative or qualitative sense to discern the solidification phenomena.

The cooling curve analysis has played an important role in the control of the metallurgical quality of metallic products obtained through processes that in some of its stages involve the solidification of liquid metal [136]. Although the solidification history is contained in the cooling curve, the most frequently measured changes are only related to alloy composition and phase transition temperatures. For that reason, there has been interest in finding new ways of analyzing the cooling curves of metals and alloys during their solidification, giving rise to what are known as Computer Aided Cooling Curve Analysis (CA-CCA), historically performed by a Newton thermal analysis (NTA) [134], [135], [136] or a Fourier thermal analysis (FTA) [138], [139] technique.

The NTA methodology has been described in detail elsewhere [134], [135]. It analyzes a cooling curve that is obtained with a thermocouple located at the thermal center of a casting. NTA calculations are performed on the first derivative of that curve. In the classical version of this method [134], the times of start and end of solidification are identified, and the zero-baseline curve is obtained from an exponential interpolation between these points. Integration of the area between the first derivatives of the cooling curve and the zero-baseline curve gives relevant information about the solidification kinetics [151].

The FTA method is based on the readings of two thermocouples located at different radial positions in a cylindrical mold, which contains the melt under study during its cooling and solidification. FTA uses the data acquired from the two thermocouples to calculate the thermal diffusivity of the sample and the zero-baseline curve by an iterative

procedure. The integration of the area between the first derivative of the cooling curve and the zero-baseline curve gives relevant quantitative information on solidification kinetics.

Computer aided cooling curve analysis assumes that the thermal events in a heating or cooling curve are directly related to phase transformations occurring in a sample. In the past few years' computer aided cooling curve analysis has also been used for the determination of thermo-physical properties of alloys, e.g., latent heat and solid fraction [152]. This technique has also been used to estimate the extent of grain refinement, degree of nodularity in cast irons etc. [152]. This is a relatively new field and thus far there have been few papers that have addressed it.

In recent years, there has been a new generation of methods enhancing the potential applications of CA-CCA elsewhere [136], [137], [138]. A very relevant change occurred with the proposal of Gibbs [136] who, for the first time, created a method of quantitative characterization of solidification that did not depend on a zero-baseline curve but was based on an energy conservation equation, opening a new avenue for the development of new CCA methods.

Solidification processes are widely used in practice. A wide range of research has been carried out to accurately monitor the solidification process, but there are still many problems to be resolved. The recent progress in numerical analysis and computing facilities permit the use of more accurate formulations and assumptions for the phenomena. Nevertheless, real-time dynamic experimental observation is still essential to compare and verify simulation results and predictions.

7.2 Phase change

Phase changes in metals/alloys are caused by changes in temperature [125], [126]. Phase diagrams are a useful tool to metallurgists and materials scientists for understanding alloys, for designing and controlling heat treatment procedures, and for solving problems that arise with specific alloys, thus improving product predictability etc. [125], [126], [127] [128]. Traditionally, phase diagrams are determined from the equilibrated alloys approach [144]. Employing this method, one can provide phase relationships of alloys under different conditions. The obtained phase equilibria are important experimental data for the optimization of thermodynamic parameters, which in turn can be utilized for calculation of phase diagrams. A phase diagram is constructed by preparing alloys of specified constituents, heating and melting the alloys, and then cooling to the room temperature, then identifying the phases, the liquidus temperatures, the solidus temperatures, solubility lines, invariants, and other phase transition lines [126]. Several techniques have been developed that rely on this approach, such as thermal analysis (TA), metallography, X-ray diffraction (XRD), dilatometry, and electrical conductivity measurement, among others [125], [127]. All these methods are based on the principle that when a phase transition occurs, an alloy's physical and chemical properties, phase composition, and/or structure will change. By analyzing the temperature, composition, and property changes associated with phase transitions, one can construct phase diagram in accordance with the Gibbs phase rule.

Many of these approaches are time-consuming or costly. In this study, a novel approach for monitoring the solidification process of tin/bismuth alloys using FBG sensors is successfully demonstrated. By embedding an individual FBG sensor and a wire

thermocouple into seven samples with different tin/bismuth alloy compositions, the entire solidification process was monitored. The crystallization process of water was also monitored as it is one of the simplest material systems and enabled a comparison with the one component alloys that go through a constant temperature phase transformation. It was demonstrated that the novel FBG sensor-based technique is better suited than the existing TC-based technique to detect the phase transitions of the alloys. Further, the axial strain evolution during the solidification process was also monitored using the FBG sensor and provided a major advantage over the TC sensor-based technique for solidification monitoring.

8.0 Materials and Methods

8.1 Materials

The materials used in the experiments were granular tin (Sn – 99.955% purity) and granular bismuth (Bi – 99.955% purity). Seven different tin/bismuth alloys were selected for this research to cover the major features of this binary phase diagram with compositions ranging from pure tin (0% of Bi) to pure bismuth (0% of Sn) as marked in Table 11 and Figure 45. The selected compositions also contained all equilibrium transformations which could be expected in tin/bismuth alloys. Since water appears to be a much easier medium to monitor for crystallization using FBG sensing than tin/bismuth alloys, the experimental and numerical techniques developed in this research for the metals were also independently verified during distilled water solidification under isothermal cooling conditions.

Table 11: Tin/bismuth alloy compositions used in this study

Sample Number	Tin %	Bismuth %
1	100	0
2	90	10
3	65	35
4	43	57
5	30	70
6	10	90
7	0	100

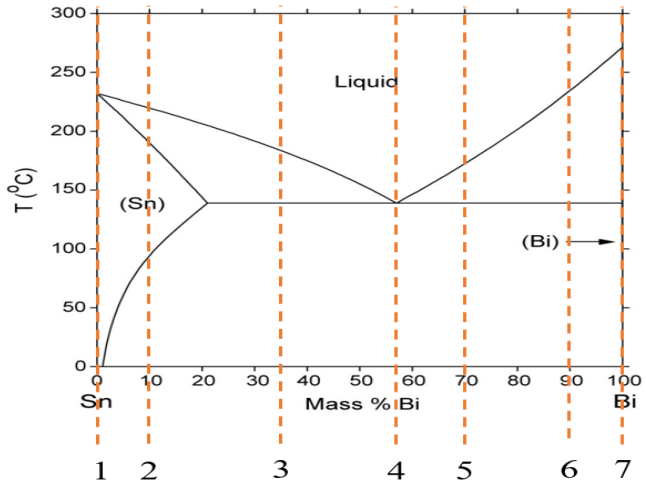

Figure 45: Tin/bismuth phase diagram [146] with specific alloy compositions investigated in this study (marked 1-7)

8.2 Experimental setups

8.2.1 Monitoring tin/bismuth solidifications

The alloys were weighed using a U.S. Solid Lab Balance scale and put into a glass test tube. 40 grams in granule form of each alloy sample were put into a cylindrical mold made of a high-temperature resistant silicone rubber. The molds were 50 mm long and had a 15 mm inner diameter and 17 mm outer diameter. Silicone rubber, being very flexible and having a very small Young's modulus ranging from 1 to 40 MPa, would not exert any measurable traction on a solidifying sample. Therefore, the alloys inside the mold during the solidification could freely expand or contract. A K-type TC was embedded in the specimen to measure the temperature during the solidification process to allow for proper temperature compensation of the FBG sensor. After completion of the solidification process, the samples were consistently cylindrical in shape with a diameter of

approximately 15 mm and length of approximately 45 mm. A schematic of the experimental setup is shown in Figure 46.

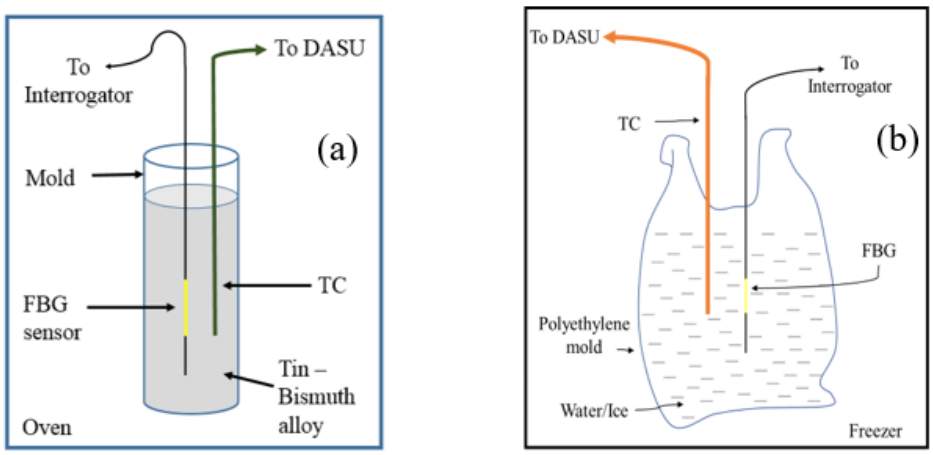

Figure 46: Schematic of the experimental setups for (a) tin/bismuth solidification and (b) water crystallization

A Ruby cutter was used to cut the FBG fiber at one end, far enough beyond the grating to mitigate any shear lag effect [27], while the other end was connected to the interrogator, the wavelength recording device. A Microstripper was used to remove the acrylate coating from the FBG fiber. The FBG fiber was placed in the middle of the mold and the K type TC was placed a certain distance away from the FBG sensor. The diameter of the TC (1 mm) was an order of magnitude larger than that of the FBG fiber (0.125 mm). The presence of the TC too close to the FBG fiber could influence the FBG measurements. Therefore, to minimize this effect, the TC was positioned approximately 4 mm away from the FBG sensors based on simple linear elastic FE analysis performed previously in chapter 3. The sensor setup was then placed in an oven. The weighed alloy composition was then poured into the mold, and the temperature of the oven was raised above the melting point of the

alloy. The wavelengths as well as the temperature were recorded every second as the various tin/bismuth alloy melts were cooled in ambient air. The shift in the FBG peak wavelength was measured with a Micron Optics si155 interrogator while the temperature was recorded by a DASU connected to the TC.

8.2.2 Monitoring water crystallization

A FBG sensor and a TC sensor were placed at least 4 mm apart near the middle of a polyethylene bag as shown in Figure 46b. The setup was then placed in a freezer. Approximately 4 liters of distilled water was poured into the bag and the temperature of the freezer was then reduced. Similarly to the tin/bismuth alloy experiments, the wavelength and the temperature data were recorded every second using the Interrogator and the DASU.

8.3 Axial strain calculation in tin/bismuth alloys using FBG sensor measurements

It has been shown in chapter 3 that for tin/bismuth alloys, the assumption of radial strains being equal to the axial strain multiplied by the negative of the Poisson's ratio of the fiber would be erroneous and the effect of radial strain on the Bragg shift might need to be considered. Hence, the full formula (equation 16) might need to be applied [139,142,148].

In that full formula, ε_1 and ε_2 were defined to be the total strains in the fiber, including the thermal strains prior to solidification of the metal and the imparted strains in the fiber from the metal after solidification. Hence, the component $(P_{11} + 2P_{12})\alpha_f\Delta T$, which is the thermal impact in the FBG fiber, can be removed from equation 16 to produce following equation:

$$\frac{\Delta\lambda}{\lambda} = \varepsilon_1 - \frac{n^2}{2}[P_{12}(\varepsilon_1 + \varepsilon_2) + P_{11}\varepsilon_2 - \frac{2}{n^3}\frac{dn}{dT}\Delta T] \quad (63)$$

In the following section, the analysis presented in Chapter 3 (Section 3.2) is repeated for various alloys of tin/bismuth to determine the impact of not including the radial strain in the governing equation.

The ratio (Z) of radial to axial strain heavily depends on the elastic properties of the matrix and the fiber. While the elastic properties of the FBG fiber are constant (the same type of fiber is used in all the experiments), the elastic properties of the metal matrix vary with sample composition. Hence, an additional analysis to determine the ratio of the radial to the axial strains for each of the seven individual alloys was necessary. The elastic properties are the room temperature (RT) values and the CTEs were measured from RT to 90°C using the dilatometer and found to be nearly constant. For the other five alloys (samples 2-6), the Young's moduli were interpolated using the rule of mixtures [27], as it was found that these values differ only slightly from the more precise Hashin-Shtriktman model [153]. Then the analysis described in Section 3.2 was completed for all the alloys to calculate the ratio of radial to axial strain (Z) and are presented in Table 12.

Table 12: The ratio (Z) of the radial strains to the axial strains for seven tin/bismuth alloys

Sample Number	1	2	3	4	5	6	7
$Z = \varepsilon^2/\varepsilon^1$	0.82	0.80	0.75	0.71	0.69	0.65	0.63

For a given wavelength shift, the axial strain in the FBG fiber can be obtained by rearranging and simplifying equation 63:

$$\frac{\Delta\lambda}{\lambda} - \frac{n^2}{2}\frac{2}{n^3}\frac{dn}{dT}\Delta T = \varepsilon_1 - \frac{n^2}{2}[P_{12}(\varepsilon_1 + Z\varepsilon_1) + P_{11}Z\varepsilon_1]$$

$$\varepsilon_1 = \frac{\frac{\Delta\lambda}{\lambda} - \frac{1}{n}\frac{dn}{dT}\Delta T}{\left\{1 - \frac{n^2}{2}(P_{12} + P_{12}Z + P_{11}Z)\right\}} \quad (64)$$

8.4 Numerical analysis of temperature distributions in tin/bismuth samples during cooling

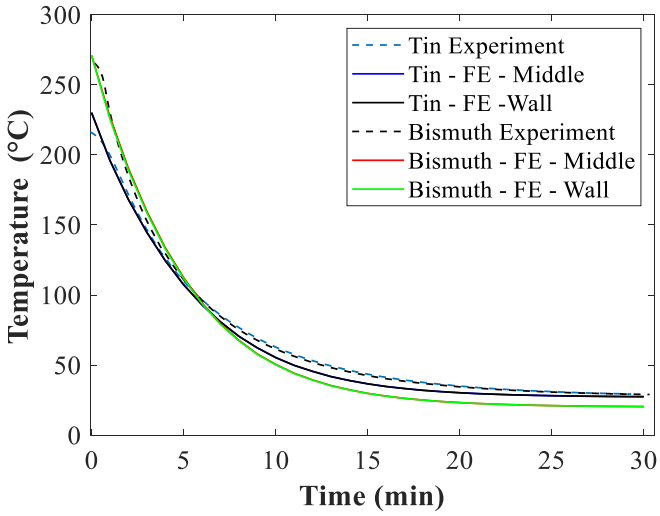

Figure 47: Cooling verification between experiment and FEM for tin and bismuth

A comparison between the experimental and the numerical temperature cooling curves for pure tin and pure bismuth samples from the end of solidification to RT are shown in the Figure 47. This comparison was important to justify that the temperature variation between the wall and the middle of the samples was small. The numerical cooling temperatures in the middle of the samples and near the mold wall were obtained by performing a transient heat transfer analysis. Cylindrical tin and bismuth samples were cooled down from their respective solidification temperatures to the room temperature. The elastic, thermal, and the geometrical properties of tin and bismuth used in the analysis can be found in Table 1. The external silicone mold walls of the samples were subjected to

convection and the temperature drop in the samples near the wall and in the middle were recorded. The temperatures extracted from FE model were then compared with the experimental temperature data. As seen in the figure, the numerical and experiment temperature profiles agree with each other and the only noticeable effect on the profiles was the type of metal.

9.0 Experimental Results

9.1 Phase Transformations in Tin/Bismuth Alloys; Comparison with Water Crystallization

In this section, various types of phase transformations (i.e., single, multi-phase transformation) as measured by the FBG sensor are discussed. It has been demonstrated that for seven tin/bismuth alloys, the FBG sensor was able to measure the beginning and end of all the phase transformations. Further, alloys in which phase transformation is taking place at a single temperature (zero degrees of freedom) such as the solidification of pure tin, pure bismuth, and eutectic tin/bismuth alloy, were compared with the crystallization of water.

9.1.1 Monitoring water crystallization using an FBG sensor

Figure 48a, and Figure 48b shows the wavelength, temperature, and strain profiles (AS^sS^fE) as a function of time measured during freezing of distilled water for two trials. The wavelength and the temperature profiles were obtained by conducting the experiment as described in section 8.2, while the axial strain profile is calculated by using the measured wavelengths and temperatures and applying equation 64. The first thermal event that was expected in the wavelength and the temperature profiles was a very small/negligible undercooling below the freezing point at S^s before the start of crystallization However, no undercooling was detected in this experiment. This is likely because the size of the sample was very large, and the cooling process was very slow. Once the critical embryo size is

reached, the system nucleates at point S^s in Figure 48 and releases its latent heat. The absence of undercooling suggests that, at nuclei, probably ice crystals were present. The timeline from S^s to S^f reflects the time during which crystal growth is occurring at 0 ^{0}C. Many small ice crystals are formed during this period [148]. The partially frozen mixture will not cool until all the water has crystallized; hence, the line S^sS^f for water occurs at a constant equilibrium freezing temperature [150]. After crystallization is completed, the temperature drops from S^f to E as the sensible heat of ice is removed. The serrations observed in Figure 48a at the end of the crystallization process (S^f) in the wavelength and strain profiles might be due to birefringence causing a split of the FBG peak and the peak reflection switching between the two peaks [16], [28].

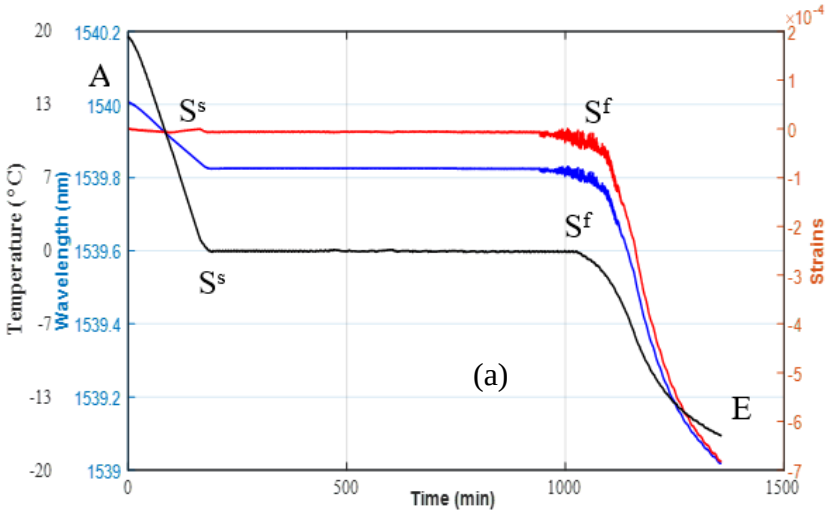

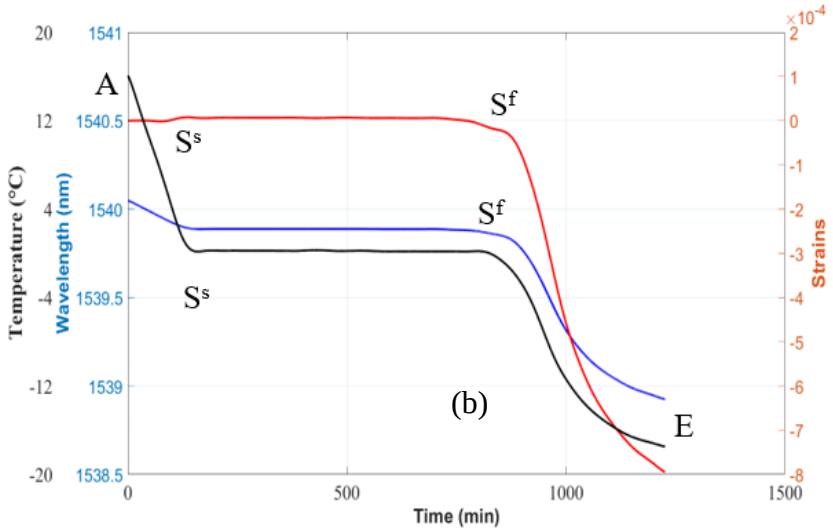

Figure 48: Crystallization of water as monitored from the FBG sensor and the TC (a) Trial 1 (b) Trial 2

9.1.2 Single phase transition points for alloys 1, 4 and 7

Alloys 1, 4, and 7 all have a single-phase transition point, from liquid to solid, and under equilibrium conditions this phase change occurs at a single temperature. In Figure 49, A is the beginning of the experiment and is the point when the oven heat is removed from the molten alloy and the air cooling of the alloy begins. A-S^s represents the cooling of the melted sample. Because of the faster cooling rate and likely presence of impurities that act as nucleating sites for solidification [133], a small supercooling in the sample (S^s) is observed. S^s is the lowest temperature/wavelength in the supercooling region before it starts to rise and represents the beginning of solidification. Similarly, S^f is the point when the solidification is complete, and from this point onwards, the wavelength/temperature profile starts to drop as the sample moves toward room temperature (E).

In samples 1, 4, and 7, as the temperature of the specimens starts to decrease from 'A' (see Figure 49), the alloys are still liquid as the temperature is well above the melting point. The liquid melt has little or no mechanical effect on the FBG sensor as substantiated by the axial strain profiles remaining close to zero. When the temperature of the specimens reach their respective solidification temperatures, the alloys change from liquid to solid producing a flat wavelength and temperature profiles. As the sample temperatures reaches solidification temperatures, a small undercooling was observed in most of the samples that indicates the lack of a seed crystal or nucleus around which a crystal structure can form. However, as the phase transition from the liquid (L) phase to the solid (S) phase begins, the latent heat of crystallization is yielded by the sample resulting in a slight increase in the temperature of the specimen. The slight increase in the FBG wavelength, consistent with the small increase in the temperature profile, supports this fact. These changes are more visible in the magnified insets in Figure 49. After the completion of the phase changes, the alloys that are now in a solid state are cooled to room temperature (30 °C).

In sample 1, however, the strain profile does not have a distinct solidification end point. If there were to be a distinct solidification end point, the profile of a cooling curve from that point onwards would be a concave up. However, the profile obtained is still concave down when the end of solidification was anticipated. Hence, a regression approach was used to determine the end of solidification point. By reviewing the data for sample 1, it can be assumed that the end of solidification is somewhere between 3 to 5 minutes because the wavelength and the temperature profiles are no longer constant and start to drop towards room temperature. Hence, to identify this point (S^f) more precisely in this sample, an

algorithm was developed which fits two regression lines to the wavelength/temperature data. The regression lines were fitted for the data before 3 minutes and the data after 5 minutes in the wavelength/temperature profile. The intersection of those regression lines was taken as the time when the solidification for the sample ended. Further discussion of this approach is provided in section 9.2.

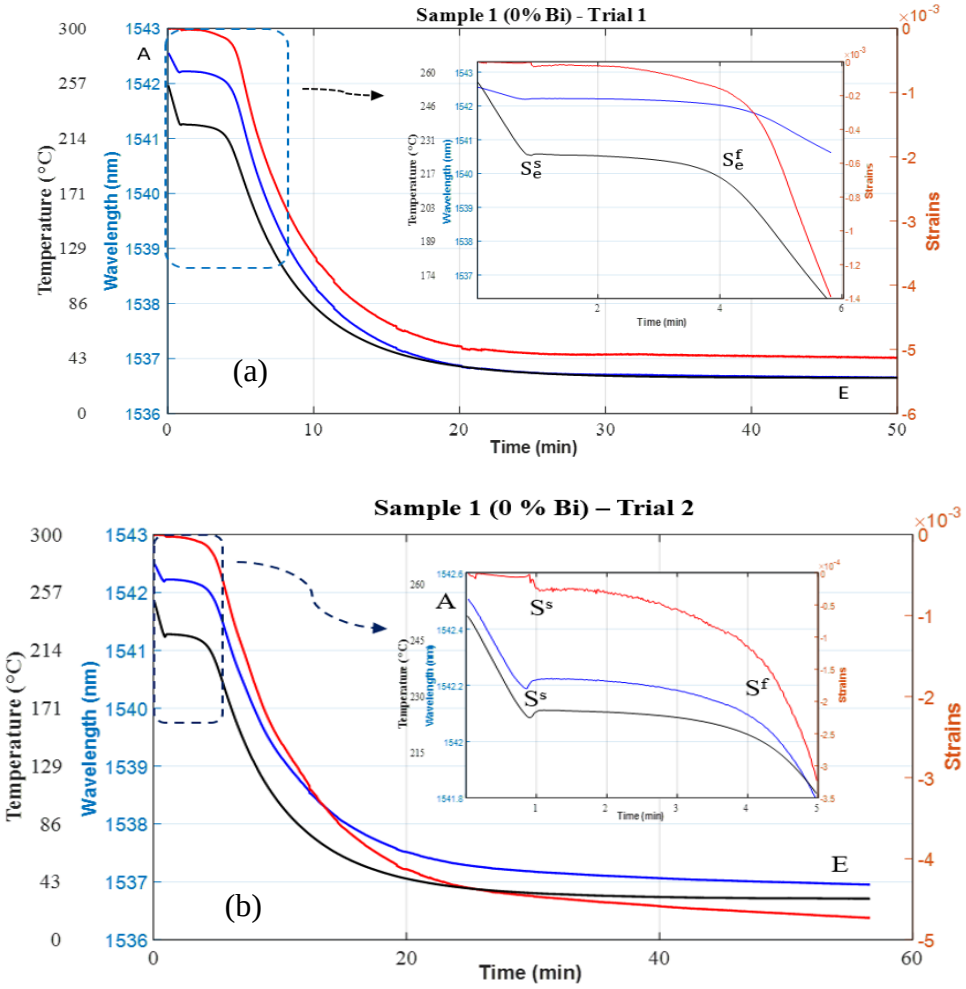

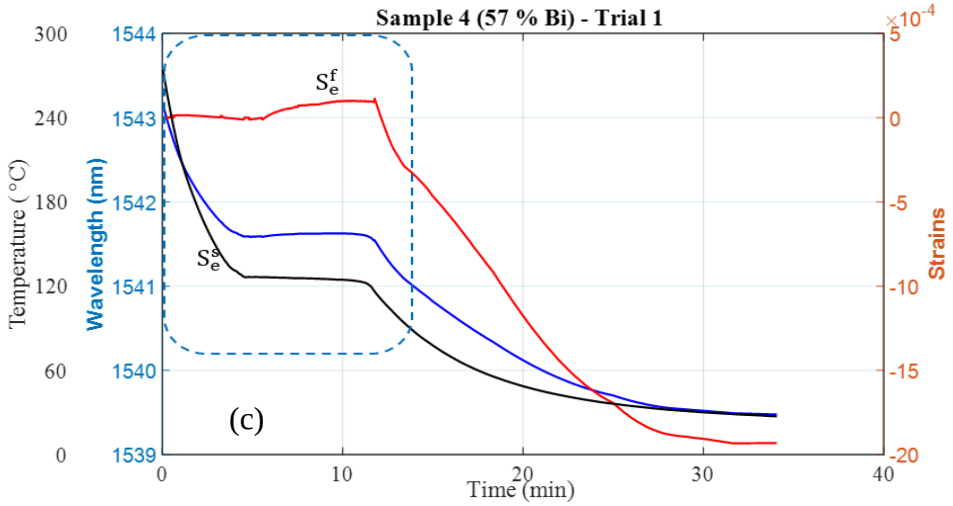
Sample 4 (57 % Bi) - Trial 1
Temperature (°C)
Wavelength (nm)
Strains
Time (min)
S_e^f
S_e^s
(c)

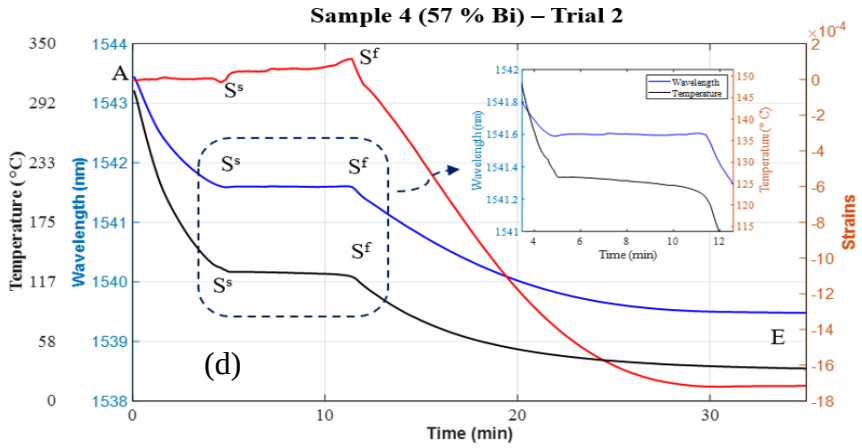
Sample 4 (57 % Bi) – Trial 2
Temperature (°C)
Wavelength (nm)
Strains
Time (min)
A
E
S^f
S^s
(d)

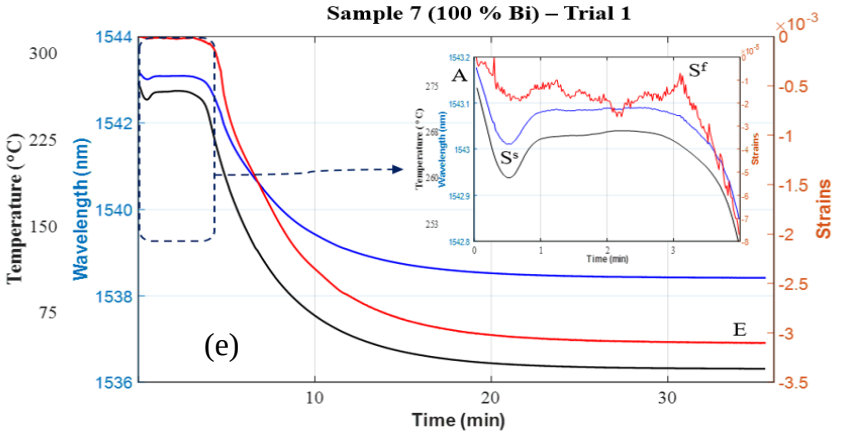
Sample 7 (100 % Bi) – Trial 1
Temperature (°C)
Wavelength (nm)
Strains
Time (min)
A
E
S^f
S^s
(e)

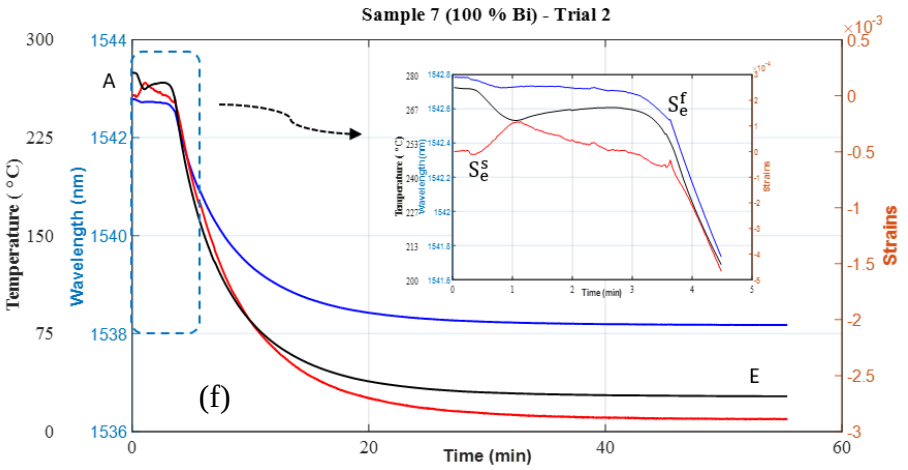

Figure 49: Wavelength, temperature, and strain profiles for sample 1: (a) and (b), for sample 4: (c) and (d), and for sample 7: (e) and (f). Two trials for each sample

9.1.3 Two transition points for alloys 3, 5 and 6

The commonalities between samples 3, 5, and 6 are that they all have two-phase transition points, and they all pass through eutectic transformations. In Figure *50* a-f, A-B is the cooling of the molten alloy, including some supercooling. At B (the liquidus line), α starts to precipitate with an evolution of heat of crystallization leading to a small temperature rise and change of slope after B. From B to S_e^s, α or β continues to crystallize from the melt. Here, S_e^s represents the start of the solidification of the alloys at the eutectic temperature. At S_e^s the remaining liquid goes through the eutectic reaction producing the α + β eutectic accompanied by an evolution of heat. At S_e^f the eutectic reaction is complete, and the sample continues to cool to room temperature, E, while the α phase progressively loses bismuth.

In Figure 50a-f, the characteristic points A, B, and S_e^s are pronounced and can be identified by the review of either wavelength or temperature data. However, the finish of

solidification (S_e^f) is only distinctly visible in the strain profiles of alloys 3, 5, and 6. The strains for sample 3 and 5 are very close to zero until they reach the end of solidification point. After that point, the FBG sensor measures the thermal contraction of the matrix. In sample 5 (Figure 50d), however, the axial strain at the beginning of the eutectic solidification is about - 300 με. This is likely because of the difference in the temperature at the TC and the FBG sensors.

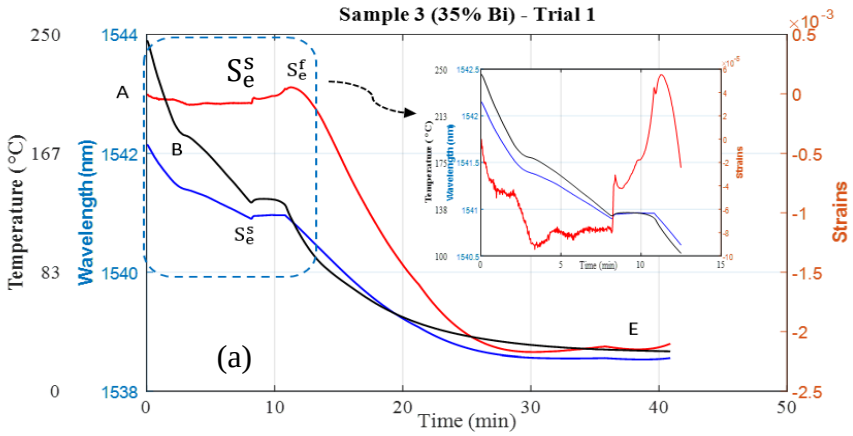

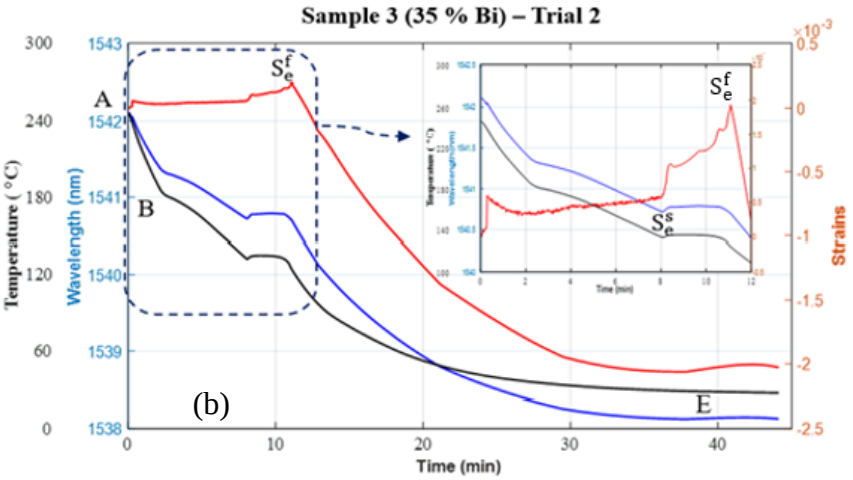

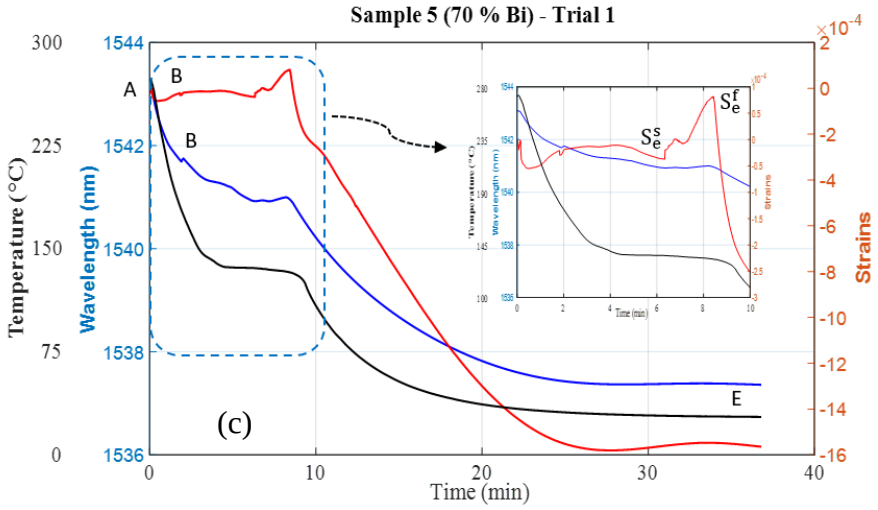
Sample 5 (70 % Bi) - Trial 1
Temperature (°C)
Wavelength (nm)
Strains
Time (min)
A
B
B
E
(c)
S_e^f
S_e^s

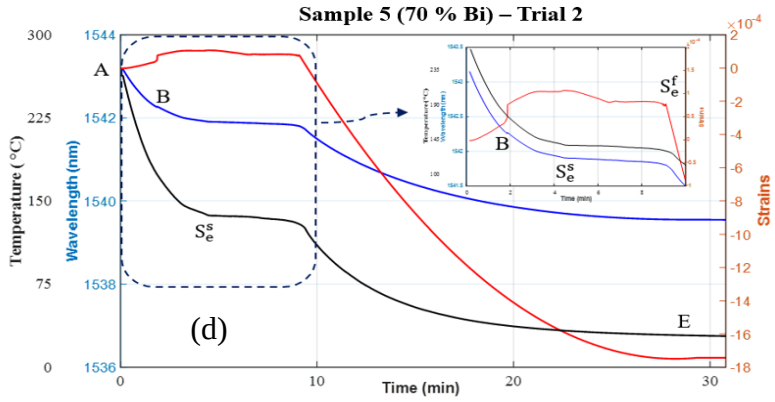
Sample 5 (70 % Bi) – Trial 2
Temperature (°C)
Wavelength (nm)
Strains
Time (min)
A
B
B
E
(d)
S_e^f
S_e^s
S_e^s

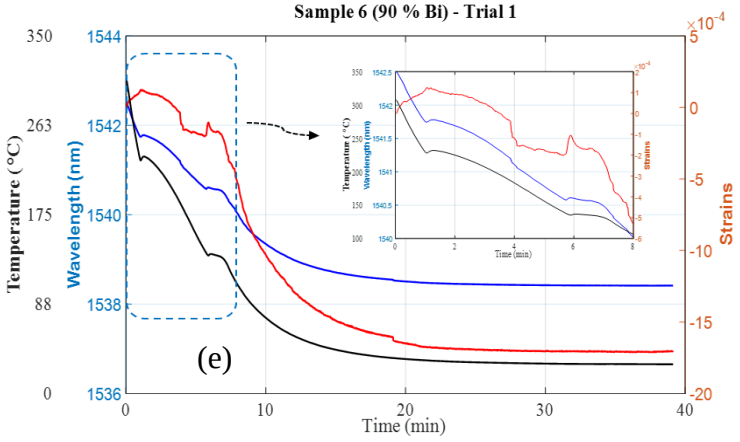
Sample 6 (90 % Bi) - Trial 1
Temperature (°C)
Wavelength (nm)
Strains
Time (min)
(e)

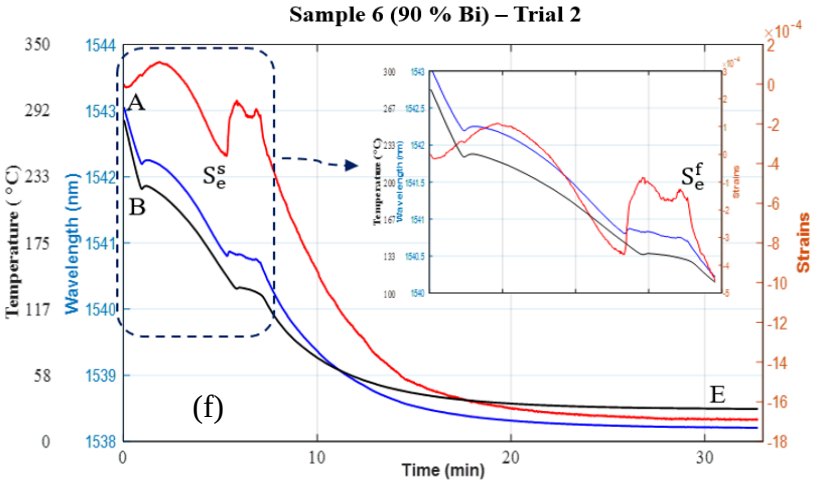

Figure 50: Wavelength, temperature, and strain profiles of sample 3: (a) and (b), sample 5:(c) and (d) and sample 6: (e) and (f). Two trials each

9.1.4 Three transition points in alloy 2

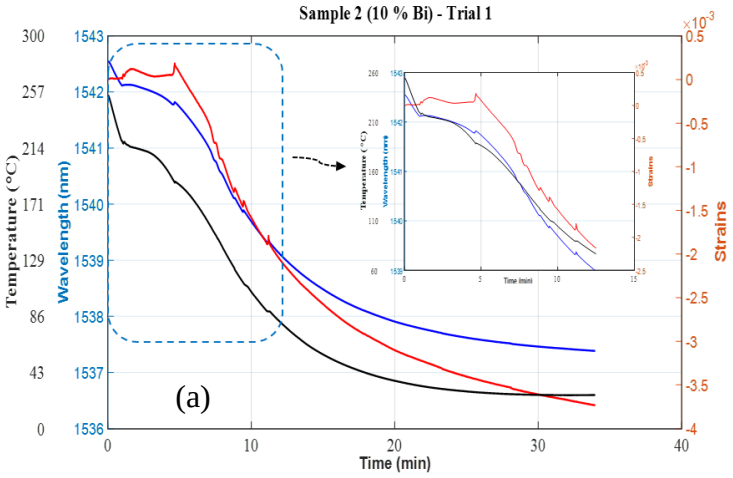

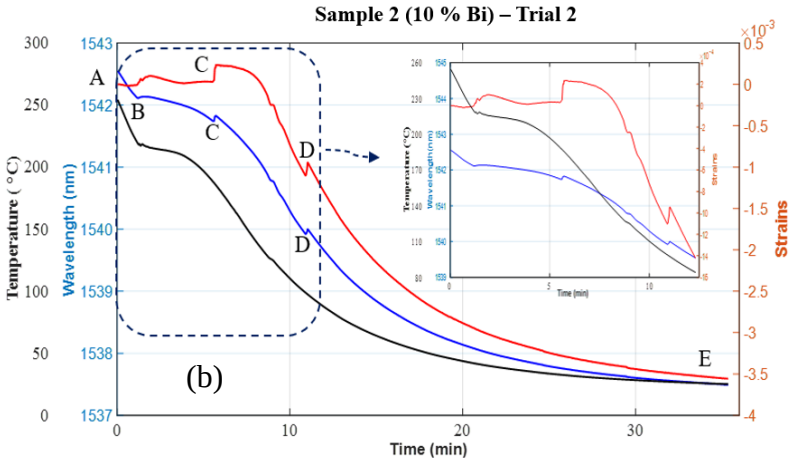

Figure 51:Wavelength, temperature, and strain profiles of sample 2 (a) trial 1, and (b) trial 2

In sample 2 (10 % Bi), three distinct phase transition points would be expected: the start of L to α + L at 222 ^{0}C, of α + L to α at 188 ^{0}C, and of α to α + β at 93 ^{0}C, where the β phase (essentially pure bismuth) precipitates from the α (solid solution of tin in bismuth). As seen in Figure 51, using only the TC, it is difficult to identify distinct points for the start of all three of these phase transitions for this sample. On the other hand, a review of the FBG sensor data was able to reveal all these transition points and the supercooling associated with liquid to solid as well as the phase transition from solid α to solid α + β. In Figure 51a, and Figure 51b, A is the beginning of the cooling of melted sample, B represents the start of the transformation from L to L+α, C represents the end of the transformation to α, D is start of the precipitation of β in the α phase, and E is the end of experiment (RT).

9.1.5 Summary of section 9.1

An interesting takeaway from the review of the axial strain profiles for these alloys is that the strains remain zero or close to zero until the solidification is finished. This implies that the interface between the FBG fiber and the matrix alloy is not formed until very near or at the absolute end of the solidification. By that time i.e., when the interface between the fiber and the matrix starts to develop, most of the liquid metal has solidified and there is very little to no liquid around the FBG sensor to detect the volumetric expansion or contraction of the alloys during solidification. Nonetheless, the FBG sensor was able to monitor the strains imparted by the cooling process after the solidification end point. The axial strains measured by the FBG sensor at the end of the process (E) are very similar to the expected cooling strains of the respective alloys. More detailed analysis of the axial strain evaluation can be found in chapter 9.4.

9.2 Identification of Characteristic Points during Solidification of Tin/Bismuth Alloys

9.2.1 Solidification temperature

The solidification temperature is the temperature at which the alloy transitions from liquid to complete solid. Ideally, the liquid to solid transition would occur at a constant temperature as the alloy is giving off latent heat during the phase change process. This constant temperature is the solidification temperature. However, in this experimental work, the temperature during this process was not constant and gradually decreased as a function of time, likely because of the large difference between the sample temperature and the

ambient temperature. Hence, the solidification temperature was estimated by taking the first maximum temperature after the supercooling point.

9.2.2 Solidification start (S^s)

During undercooling, the small and negative free energy change exists in the system, acting as a driving force for the nucleation process [148]. Since undercooling was observed in all experiments, this point is taken as the beginning of solidification. It is evident that both wavelength and temperature profiles can identify both undercooling and the subsequent temperature maximum at the beginning of the solidification process (see Figure 49, Figure 50, and Figure 51 insets).

9.2.3 Solidification end (S^f)

If the FBG and the TC profiles show the distinct characteristic points (abrupt slope changes) after the conversion of the liquid to the solid then the end of solidification (S^f) can be visually determined by reviewing the wavelength, and the temperature profiles. However, in some cases (see Figure 49 – sample 1 and sample 7), the wavelength and the temperature profiles did not show a clear characteristic point i.e., the slope changes were gradual. Hence, it is difficult to establish the exact time when the solidification process is finished. The axial strain profile of the alloys as calculated using equation 64 could help identify the solidification end point. As seen in Figure 49(c-d) and Figure 49(e-f) for alloys 4 and 7, respectively, the end of solidification point (S^f) is more pronounced in the strain profiles. In some of the samples, however, even the strain profile does not have a distinct solidification end point (Figure 49a). Hence, several approaches were used in this study to identify the end of solidification (S^f) point consistently.

9.2.3.1 Regression approach

When the FBG and the TC profiles do not show an abrupt slope change at the end of solidification in the cooling curve, then by reviewing the FBG and the TC data, the solidification end region can be tentatively identified. i.e., the gradual slope change region. To precisely pinpoint the solidification end point (S^f), a technique of fitting two regression lines, one before the beginning of the gradual slope change, and another one after the completion of a gradual slope change, is developed. The intersection of these two regression lines provides the end of the solidification point. This approach was used for all the wavelengths and the temperature profiles obtained from every trial of all the samples. The regression curves can be of single or multi-order.

9.2.3.2 The strain method

This is the visual method of determining the end of the solidification point. In most of the axial strain profiles for the alloys investigated in this work, a clear and abrupt slope change was observed at the expected solidification end point (see Figure 49, Figure 50, Figure 51). Hence, those points were visually picked as the solidification end (S^f) point and compared with other approaches discussed in this study in Table 13. However, in some of the trials, the strain profiles did not show an abrupt slope change (see Figure 49a). In those trials, the regression approach, or the heat balance approach was employed to estimate the solidification end point.

9.2.3.3 Heat balance approach

In perfect experiment with little or no effect of external environments, the end of solidification would be a point in time from which the solidification temperature profile

would follow a normal cooling profile. In another word, from this point onwards, there would be no generation of latent heat due to solidification. Therefore, following an approach developed previously for the polymers in chapter 6, the heat generation in each timestep is calculated. Using a step wise approach, the relative heat (in units of J $mass^{-1}$ C_p^{-1}, where C_p is the specific heat of each alloy sample) generated in each time step can be calculated using the current and previous temperatures and is given as:

$$\Delta H_{(n+1)} = T_{n+1} - T_n + K_c (T_n - T_a) \quad (65)$$

where, T_n is current temperature, T_a is ambient temperature, K_c is the thermal conductivity factor and ΔH_{n+1} is the heat added at every time step to the system. If there was no heat being added to the system (i.e., at the solidification end point), then the temperature in the next time (T_{n+1}) step is given as:

$$T_{n+1} = T_n - K_C(T_n - T_a) \quad (66)$$

In equation 66, an optimized K_c was estimated by fitting the expected temperature curve to the pure cooling portion of the experimental temperature profile. Then, by using the optimized K_c, a cumulative heat during the entire solidification process was calculated by solving for ΔH in equation 65. The result obtained for one trial each for all the samples except sample 2 is shown in Figure 52. The cumulative heat for sample 2 was not calculated as the sample does not have a constant solidification temperature.

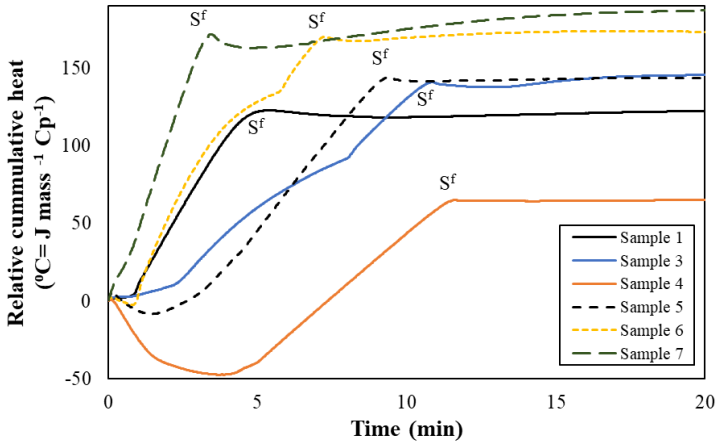

Figure 52: Cumulative heat as a function of time for 1 trial of all samples (except 2)

In Figure 52, the cumulative heat plot for sample 4 is negative in the beginning. This is likely because the model used in this work assumes thermal conductivity (K_c) to be constant in the liquid as well as in the solid phase. It was reported previously that the thermal conductivity of a eutectic alloy increases with an increase in the temperature when in a liquid state [149]. Hence, if the actual temperature-dependent thermal conductivity was known then the cumulative heat plot for sample 4 would likely be similar to that of the other samples. The assumption of constant thermal conductivity however does not affect the estimation of solidification end (S^f) time which is of particular interest in this study.

9.2.3.4 Comparison of solidification end time calculated from the regression, strain, and heat balance approaches

As an example, the regression approach used for the FBG and TC data for one trial of sample 4 is shown in Figure 53a, and Figure 53b, respectively. The solidification end time estimated after applying the regression method to the wavelength and the temperature profile was 11.23 and 11.12 minutes, respectively. The strain profile (Figure 53c) of this

sample showed a clear end of solidification point at 11.40 minutes; hence, a regression line approach was not needed. Figure 53d shows the heat generated at every time step and the cumulative heat as a function of time for sample 4. As seen in Figure 53d, after 11.65 minutes, there is no more heat being added to the system, signifying the end of solidification using this method.

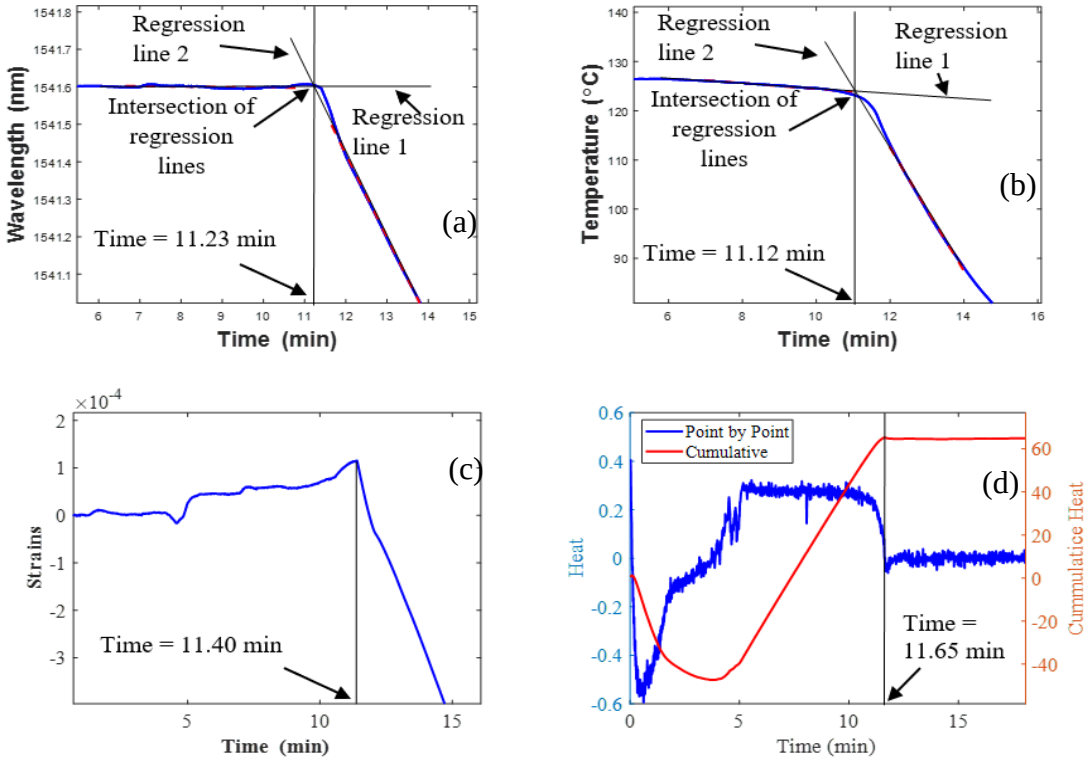

Figure 53: Determination of S^f using regression approach in the FBG (a) and the TC (b) profile, the strain (c) and heat balance (d) method for sample 4

Table 13 provides the summary comparison between the solidification end time (S^f) calculated using the regression approach in the FBG and the TC data, the strain method, and the heat balance approach for one trial of all the samples. A similar table could be

obtained for the second trial as well. The time discrepancy between the methods is small but the heat balance method gives slightly larger values.

Table 13: Comparison of S^f determined using FBG, TC, strains, and heat balance approach

	Solidification finish time (S^f) (min)			
	FBG	**TC**	**Strain**	**Heat Balance**
Sample 1	4.23	3.93	4.40	4.70
Sample 2	N/A	N/A	N/A	N/A
Sample 3	10.80	10.57	11.08	10.90
Sample 4	11.23	11.13	11.40	11.76
Sample 5	8.90	9.10	8.98	9.38
Sample 6	7.03	7.05	7.06	7.25
Sample 7	3.38	3.16	3.10	4.00

9.3 Effect of Alloys Composition on Characteristic Solidification Points

9.3.1 Comparison between water crystallization and single-temperature transformations of Alloys 1,4 & 7

The crystallization of water and the crystallization of alloys 1, 4, and 7 are the simplest among all the solidification processes discussed in this dissertation because they involve a phase transformation occurring at a single temperature under equilibrium conditions. As observed in Figure 48, the beginning, and the end of the crystallization of water is distinct in both the temperature and the wavelength profiles. There was very little/no undercooling present during water crystallization for two reasons. First, the sample size was very large (dia.=200 mm) and hence the sample was able to retain heat for a longer period. Second, the temperature difference between the sample and the ambient was small (=20 °C); as a result, there was a slower cooling rate. Undercooling occurs when heat is removed from a liquid sufficiently rapidly that the molecules do not have enough time to align themselves

in the ordered structure of a solid [144], [151]. The alloys 1 and 7 have a smaller sample size (dia.=15 mm) and the temperature difference between the sample and the ambient is more than 200 °C, therefore, the cooling takes place more rapidly giving atoms less time to align themselves in the ordered structure and, hence causing moderate undercooling. Alloy 4 on the other hand does have a small sample size but the temperature difference between the sample and the ambient is significantly lower by about 100 °C than that of alloys 1 and 7. Hence, very little undercooling in sample 4 was observed. The absence of undercooling in sample 4 could also be due to the low temperature of the eutectic melt just above the eutectic temperature. This would promote tin-rich and bismuth-rich metastable precursor cluster formation in the melt. These could act as nuclei at the eutectic temperature. Another potential reason that undercooling in water was not observed is likely because the distilled water used for the experiment had little to no impurities present. Absence of seed crystals or impurities promotes undercooling, therefore absence of undercooling in the water sample means that ice crystals must have been present, maybe in the ambient air.

9.3.2 Prediction of solidification times for alloys 3, 4, 5 and 6

Figure 54 shows the time taken for eutectic transformations by samples 3, 4, 5, and 6 as a function of the amount of liquid present. The amount of liquid present at the eutectic transformation for each sample was calculated using the Lever rule. Similarly, the time taken for solidification (S^f - S^S) was estimated by reviewing the strain data and by using the heat balance approach. As seen, the greater the amount of liquid present in the sample, the longer it took to finish the eutectic transformation. The relationship between the time

for solidification and the amount of liquid present for samples 4, 5 and 6 is close to linear. In Figure 54, sample 3 falls below the trend line most likely because it is a tin-rich sample, rather than a bismuth-rich sample, and has higher thermal conductivity than samples 5, and 6. It is likely that if more alloy samples in the tin-rich region (left side of the eutectic) were analyzed, the relationship between the solidification time and mass fraction of liquid present for those tin-rich alloys would have been linear as well.

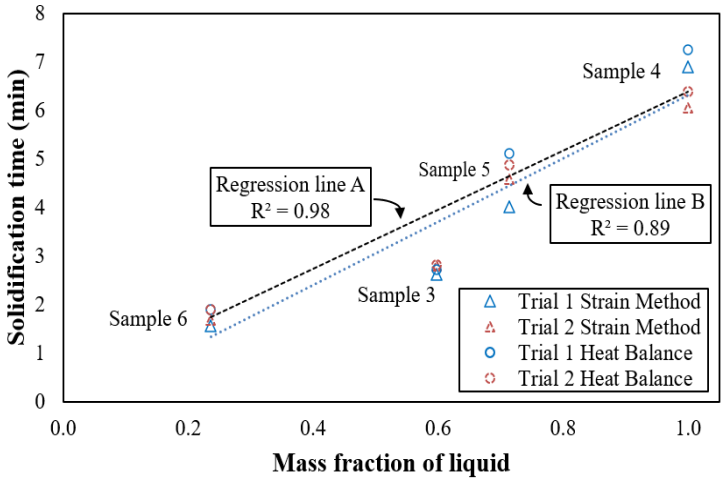

Figure 54: Solidification time calculated using the strain and the heat balance technique as a function of mass fraction of liquid

9.3.3 Effect of alloy compositions on transformation temperatures; independent verification of FBG/TC measurements

Table 14 shows the measured transformation temperatures for various alloys using the FBG and the TC. The measured transformation temperatures are compared with the temperatures found in the literature for tin/bismuth alloys [148]. The transformation temperatures were found by reviewing the TC and the FBG data.

Table 14: Comparison between the measured transformation temperatures from the TC and the FBG with the literature data [148]

Bismuth %	Phase change	Temperature (°C)				
		Literature	Thermocouple		FBG	
			Trial 1	Trial 2	Trial 1	Trial 2
0	L to S	231.00	229.80	230.30	227.80	227.00
10	L to α+L	222.00	217.00	217.75	220.00	219.56
	α+L to α	188.00	**N/A**	**N/A**	187.84	187.31
	α to α+L	93.00	**N/A**	**N/A**	92.00	98.42
35	L to α+L	184.00	182.07	182.70	179.50	181.00
	α+L to α+β	139.00	131.80	131.40	133.08	133.61
57	L to α+β	139.00	127.42	127.52	130.01	131.22
70	L to L+β	174.00	**N/A**	**N/A**	178.50	178.80
	L+β to α+β	139.00	130.02	130.50	135.99	135.65
90	L to L+β	233.00	223.15	226.90	229.10	228.00
	L+β to α+β	139.00	130.81	130.87	137.80	135.23
100	L to S	271.00	263.95	262.16	266.30	265.50

To identify the transformation temperatures using FBGs, first the characteristic points on the FBG wave profiles were determined. After that, the time at which those characteristic points were observed were found and then that time was traced to the TC profile to get the temperature. There is small discrepancy (<1%) between TC and FBG measured transformation temperatures, due to small differences in timing identified by the two sensors. Further, the difference between the measured transformation temperatures and the literature values is likely due to significantly slower cooling rates in the latter, in order to approximate equilibrium conditions. Potential errors in mass measurements of the constituent alloys leading to slightly different alloy compositions, could also contribute.

Figure 55a, and Figure 55b shows the phase diagram constructed from the TC and the FBG data, respectively. Figure 55a-b show some undercooling in comparison with literature data, which is to be expected since the cooling rate of approximately 6 °C/min

did not allow phase equilibrium to be fully established. As seen in Figure 55a, the inspection of the TC data did not allow for the identification of all the characteristic points during the solidification process. For example, for the 10 % bismuth sample (sample 2 – see Figure 51), only one of the phase change points could be identified using the TC data as opposed to the three phase changes that occur during the solidification of this alloy. This is because, except for the first phase change, L precipitating α, which is accompanied by some supercooling, there is no abrupt change in the amount of material undergoing phase change at each of the remaining phase change points. Therefore, there is insufficient thermal emission to reveal these phase change points using the TC results. On the other hand, by inspecting the FBG measurements all three phase change points (Figure 51) were identified for this alloy composition. The temperatures in Figure 55b was obtained by finding the temperature from the TC at the time corresponding to the identified phase change using the FBG.

For the 70 % bismuth (sample 5, Figure 50c-d), inspection of the TC data revealed only the phase change at the eutectic reaction, which was accompanied by a large heat of crystallization. Evidently the undercooling of the β phase was insufficient to reveal the onset of β crystallization. Examining the FBG data, it was again possible to detect both phase change points (Figure 50c-d) for this sample. Similar cases were identified for other alloy compositions as well. Hence, it is safe to conclude that the FBG sensors are better equipped to detect phase changes than the TC sensors. Full results of the phase change temperatures using both techniques are presented in Table 14.

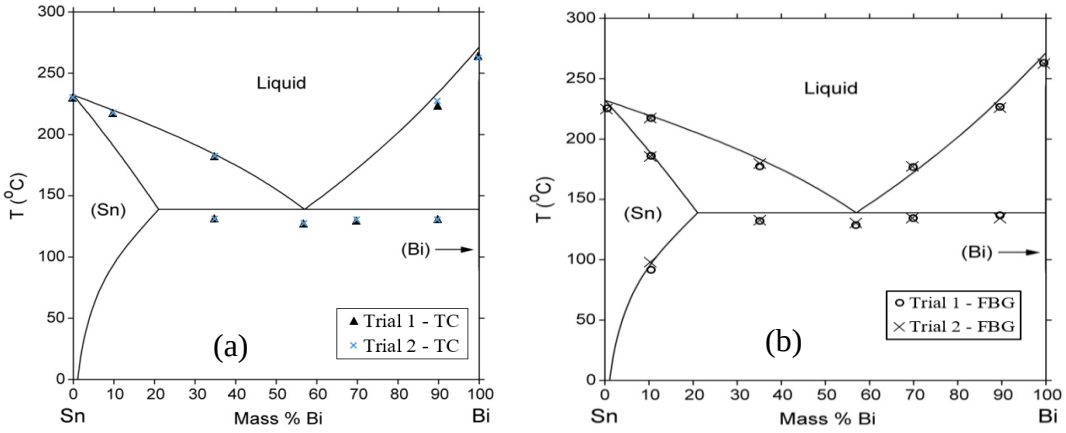

Figure 55: Comparison of the published [148] tin/bismuth phase diagram (solid lines) with that obtained from (a) the TC sensors (b) temperatures at the phase change points identified by the FBG sensors

A potential reason that all the phase changes in some of the samples are not easily identified with the TC is that with the phase change taking place over a range of temperatures, the amount of material crystallizing at these phase boundaries is insufficiently large for these transitions to be detected as a slope change in the TC temperature profile. The FBG sensors, on the other hand, have better temperature sensitivity. The changes of phases are thus more pronounced in the FBG wavelength profile as compared to the temperature profile.

9.4 Strain verification in tin/bismuth alloys

The axial strain in the FBG fiber was calculated from the FBG peak wavelengths and the temperature change by using equation 2 until the solidus line was reached and using equation 64 afterwards. However, prior to the solidus line, the pure thermal strain in the fiber ($\alpha_f * \Delta T$) was removed from equation 2 as it was not caused by the strain in the alloys

(it is caused only by the temperature impact on the fiber). Ideally, this should lead to an observation of zero strain before the solidus line, but in practice some small fluctuations were observed. Below the solidus line, the strains in the fiber are controlled by the strains in the metal. The axial portions of the final strains in the FBG fiber, once each sample is returned to RT, for various tin/bismuth alloys are between -0.17% and -0.52%. The evolutions of wavelength, temperature, and axial strains during the solidification process from two trials each of all the tin/bismuth samples studied in this research were presented in section 9.

As presented in Figure 49, Figure 50, and Figure 51, after the removal of the pure thermal strain in the fiber, the axial strain profile does not deviate much from zero until the solidus is reached. This means, that the FBG sensor is not affected much by the volumetric expansion/contraction during the solidification while liquid is present. One potential reason for this could be the inability of the FBG fiber to form a reliable bond with the alloy during the crystallization process. In that case, the FBG fiber would be surrounded by a mixture of melt and crystals forming during the phase change from liquid to solid. Since no reliable bonding has been established between the FBG fiber and the newly formed crystals, the FBG fiber would not detect the volumetric change of the alloy. As more and more of the melt is converted to the solid, the presence of crystals adhering to the FBG sensor would start affecting the measurement. Hence, some fluctuations in the strain profile at the beginning of the solidification phase were observed (see Figure 49, Figure 50, and Figure 51). Crystallization would first start on the outer surface of the sample and then move towards the middle (i.e., towards the sensor) since the temperature at the outer surface cools

faster than the middle. Hence, it is possible that by the time the melt surrounding the sensor is converted to solid, the outer portion of the sample has already solidified, resisting any volumetric change.

Table 15: Summary of axial strains for all samples and a comparison with estimated cooling strains

Bismuth %	Measured CTE (α_m) (e-6/K)	Solidification temperature (T_s) (° C)	Estimated cooling strains [$\varepsilon_c = \alpha_m * (T_r - T_s)$] (με)	Experimental axial strains (με)					
				Including radial strains			Excluding radial strains		
				Trial 1 (ε_1)	Trial 2 (ε_1)	Average	Trial 1 (ε_1)	Trial 2 (ε_1)	Average
0	23.74	230	-4748	-5146	-4719	-4933	-2426	-2233	-2330
10	22.00	182	-3344	-3321	-3346	-3334	-1620	-1627	-1624
35	18.70	131	-1889	-2147	-1980	-2064	-1092	-1007	-1050
57	17.49	127	-1697	-1652	-1715	-1684	-866	-908	-887
70	16.87	130	-1687	-1570	-1725	-1648	-854	-938	-896
90	15.01	130	-1501	-1692	-1675	-1684	-942	-929	-936
100	12.55	262	-2912	-3040	-2838	-2939	-1738	-1621	-1680

At the solidus line, the cooling of the fully solidified sample in the ambient air begins. Apart from sample 6, all other samples follow the trend as discussed above. Sample 6 however, shows a small contraction between the beginning and the end of crystallization. One potential reason for this could be that the temperature difference between the liquidus and the solidus for this alloy is large: ~ 100 °C. Therefore, there is more opportunity for larger fluctuations to occur in the bonding between the crystallizing β phase and the FBG fiber. In addition, on cooling, the outer surface of the high bismuth content sample has solidified and become rigid, this would exert compressive stresses on the solidifying interior of the sample and therefore on the FBG sensor since high bismuth alloys expand on solidification.

Table 15 provides a summary of the estimated and the experimental axial strains in the FBG fiber from the two trials for each sample, at the end of the solidification process. An estimation of the axial strains in the fiber is made based on the dilatometer measured CTE (α_m) of each sample and the difference between the average solidification temperature (T_s) and the room temperature (T_r=30 °C). i.e., the axial cooling strains were estimated as α_m* (T_r -T_s). Further, the average experimental axial strains including the radial strains (equation 64) and excluding the radial strains (equation 15) in the calculation are also listed in Table 15. The difference in the calculated axial strains including radial strains and excluding radial strains is significant. This validates the conclusion reached in Section 3 that for a matrix with large stiffness properties, exclusion of radial strain in the axial strain calculation leads to erroneous results. The FBG measured axial strains when the radial strain contribution was included in the calculation for all the samples were close to the estimated axial strains (ε_e). The slight difference could be because of the temperature difference between the FBG sensor and the TC, leading to an over or under estimation of the true temperature change of the alloy at the sensor location. Another possible reason could be because the CTE was measured only for the temperature range from 25 °C to 90 °C.

9.5 Stress estimation near the mold surface

In this section, a proof of concept of a new and simple approach using the FBG sensors to determine the residual stress in a sample subjected to traction from a mold during solidification is presented. The axial strains presented in Section 9.4 are the traction-free

strains as the alloys were solidified and cooled in a soft silicone rubber mold. However, the traction from a stiffer mold (for example aluminum, glass, steel, etc.) would likely affect the strain in the FBG fiber. As an example, if the solidification of pure tin (sample 1) were to be carried out in a stiffer cylindrical mold with a lower CTE, the mold would resist the shrinking of the tin during cooling. Hence, the compressive strain in the tin sample near the tin/mold interface would be less than the strain that would result from the traction free mold. Hence, the residual strains in the tin sample near the tin/mold interface would be the difference between the strain in the tin under constrained conditions and the stress-free strain in the tin, i.e., Residual strain = strain in the tin during the constrained condition - stress free strain in the tin. The residual stress would then simply be the product of the stiffness matrix and the residual strain. The following steps can be used to determine the residual stress at the sample/mold interface:

i) Numerical prediction of residual stress at the alloy/mold interface

In order to numerically predict the residual stress at the alloy/mold interface, the FE cooling analyses of sample (example: tin) with a glass mold and with a silicone mold can be conducted. The FE model can be cooled from the solidus temperature (example = 230 °C for tin) to RT (30 °C). By extracting the axial and radial strains from both the silicone and glass mold, the strain in the alloy near the alloy/mold interface, as a result of a temperature drop from solidus temperature to the RT can be determined for both mold systems. Let us assume the strains are ε^{SM} in the silicone mold and ε^{TM} in the glass test tube mold. Thus, the residual strain can be given as $\varepsilon^{TM} - \varepsilon^{SM}$. The residual strain can be

multiplied by the stiffness matrix to obtain the expected residual stress near the alloy/mold interface.

ii. Measurement of residual stress at the alloy/mold interface using FBG sensors

Stress free strain in the alloys have already been reported in Section 9.4. They were calculated using equation 64. In that equation, the ratio of the radial to axial strains in the FBG fiber, Z (to be denoted as Z_s in this section), for a silicone mold were found for all the alloys investigated in this research. This value of Z_s might not hold true for the constrained condition. Hence, in equation 64, the ratio of radial to axial strains (Z_{cf}) in the fiber for the constrained condition needs to be identified.

$$\frac{\Delta\lambda_{GM}}{\lambda_{GM}} = \varepsilon^1 - \frac{n^2}{2}\left[P_{12}\left(\varepsilon^1 + Z_{cf}\varepsilon^1\right) + P_{11}Z_{cf}\varepsilon^1 - \frac{2}{n^3}\frac{dn}{dT}\Delta T\right] \quad (67)$$

Here λ_{GM} is the wavelength shift from the glass mold experiment. Henceforth, following analyses could be performed to obtain the Z_{cf} value for the constrained condition.

a. FE analysis can be performed to find the ratio of the radial to axial strains in the alloy (Z_{cm}) near the alloy/glass mold interface

By carrying out the FE cooling analysis with glass mold for different temperature changes (let's say 50 °C, 100 °C, and 200 °C), the ratio Z_{cm} can be found.

b. *Using Z_{cm} and an Eshelby approach, fiber strains could be extracted*

The strains in the fiber can be extracted using an Eshelby approach, given an applied far-field strain to the alloy. Based on the Eshelby approach previously established in Section 3, for an applied strain (ε^a) on the matrix, the fiber strain (ε^f) during the constrained condition is given as

$$\varepsilon^{f} = \{S[\mathbf{C_f}S - \mathbf{C_m}(S - I)]^{-1}(\mathbf{C_m} - \mathbf{C_f}) + I\}\,\varepsilon^{a} \quad (68)$$

where all the variables are defined previously.

Let us assume, the far-field axial matrix strain to be ε^{1m}. Then ε^{a} is given as [ε^{1m} Z_{cm}*ε^{1m} Z_{cm}*ε^{1m} 0 0 0]. By substituting the value of ε^{a} in equation 68, the fiber strains (ε^{f}) can be estimated. The ratio of radial to the axial strain (Z_{cf})for the fiber during the constrained condition can be determined from the estimated fiber strains. Now, for a given wavelength change in glass mold, using the ratio (Z_{cf}) and equation 67, the strains in the fiber during the solidification of alloy during a constrained condition can be calculated. Multiplication of the measured strains by the stiffness matrix would provide the residual stress at the alloy/mold interface.

Summary Discussion and Concluding Remarks

The experimental and analytical results presented in this research demonstrate the application of FBG sensor in monitoring the solidification process using tin/bismuth alloys as an example. First, the effect of excluding the radial strain impact on the FBG fiber axial strain calculation was discussed. It was shown that unlike polymers, the impact of excluding the radial strain in the FBG fiber strain calculation for the tin/bismuth alloys is significant and thus should not be overlooked. Just like the temperature cooling curve during solidification, the FBG cooling wavelength curve could be used to visually establish the beginning of the solidification point, albeit more prominently in some of the alloys investigated. The solidification end point was challenging to establish for some of the alloys by reviewing the temperature or the wavelength profiles alone. However, the strain profile, which is the combination of both the wavelength and the temperature profiles were useful in determining the solidification end point. To determine the end of solidification more consistently, several approaches were used, namely: the regression approach, the strain method, and the heat balance approach. The results from these approaches had a very small scatter.

Further, FBG sensors could be used to determine all the phase transition points in the alloys. Since FBG sensors are very sensitive to temperature change and to stress state change, the FBG sensors were able to act in response to all the phase transitions that occur during the entire cooling history of all the alloys investigated in this study. The phase

diagram created from the FBG sensor data was compared with that from the TC, and with the literature. The discrepancy between the FBG phase diagram and the literature phase diagram was relatively small. Hence, it was recognized that the FBG sensors are better suited than thermocouple sensors for the construction of the phase diagrams. Moreover, the FBG sensor also provided valuable information about the strain state of the metals/alloys. The strains measured ranged from 0.17 to 0.52 %. The axial strains as measured by the FBG sensors are comparable to the expected cooling strains of the respective tin/bismuth alloys. The strain in the FBG fiber can be used to calculate the stress in the fiber and in the metal matrix.

In conclusion, in situ FBG sensor-based technology has significant advantages in monitoring the solidification of the alloys, and it can become a powerful technical means in the field of material science and engineering. For instance, this technology can be well applied in quantifying the residual stresses development during casting and additive manufacturing process. With a suitable sensor and an appropriate experiment, it can also be used to estimate the volumetric expansion/contraction during solidification of metals/alloys, which is impossible to achieve by conventional TC-based cooling curve analysis techniques.

Monitoring Ice Crystallization on High Voltage Transmission Lines Using FBG Sensors

10.0 Introduction

10.1 Background

Lightning, thunderstorms, and tornadoes are not the only threats to the electrical infrastructure [154], [155], [156], [157]. Frequent, long-duration and widespread ice accumulation in high voltage (HV) transmission lines is a common problem in parts of the world with cold climates. Ice accumulation on the surface of the conductor can be dangerous and destructive to power lines, leading to a disruption in service [158]. The icing on the transmission lines can cause additional severe static loads (abnormal tension increase and/or abnormal increase of sag not related to high electric loads), strong cable motions, and/or high/severe dynamic loads (galloping, oscillation, and ice-shedding), etc. Surfaces with poor hydrophobicity and high thermal conductivity, such as glass and metal, are especially prone to ice adhesion and buildup, including aluminum strand high voltage (HV) powerlines (Figure 56) [154], [155]. When overwhelmed with the weight of ice, the HV lines and/or towers can collapse. Half an inch of ice can add as much as 500 pounds to a power line (~1000 ft. long), and damage can begin when accumulations exceed a quarter of an inch. This results in severe economic losses and in extreme circumstances, even the loss of life [155], [156], [157], [158].

Figure 56: Ice accumulation on an HV transmission line [159]

Researchers in the past have developed numerous theoretical and experimental techniques such as non-contact infrared measurement, video surveillance, dip-sag monitoring, and temperature sensing at the line surface or core for the reliable estimation of the thickness of ice on the transmission lines [160]. These methods/models generally do not provide accurate icing thickness, and they are confronted with difficulty in power supply and electromagnetic interference. But very little or no work has been done to estimate the beginning and end of ice accumulation and to evaluate the amount of ice accumulated on the HV transmission lines. A real-time direct local measure/detection of ice accretion can be useful in several applications, and in particular for monitoring the transmission and distribution network since the accretion of ice, snow, wet snow, frost, etc. and their mixtures can lead to potential clearance violation, damage, and power outages due to important static and/or dynamic mechanical overloads. Hence, in this work, a novel FBG sensors-based monitoring system which can accurately and reliably measure the amount of ice on the HV transmission lines has been proposed.

11.0 Experimental setups

The first step towards developing a reliable FBG sensor-based ice accumulation measurement system would be to demonstrate that the FBG sensor can measure the formation of ice on the HV transmission lines. Hence, an experiment was developed to monitor the crystallization of ice on the transmission line. A stripped FBG sensor was epoxied to the surface of an Aluminum Composite Core Conductor (ACCC) along the strand using Devcon 14250 epoxy and cured for 1 hour at RT. The ACCC conductor with the epoxied FBG sensor was then placed in a polyethylene bag containing distilled water. A polyethylene bag was used as a mold as polyethylene would not exert any mechanical loads to the crystallizing ice or to the FBG sensor. A K-type thermocouple was also attached to the surface of the conductor. The entire setup (Figure 57a) was then placed in a freezer.

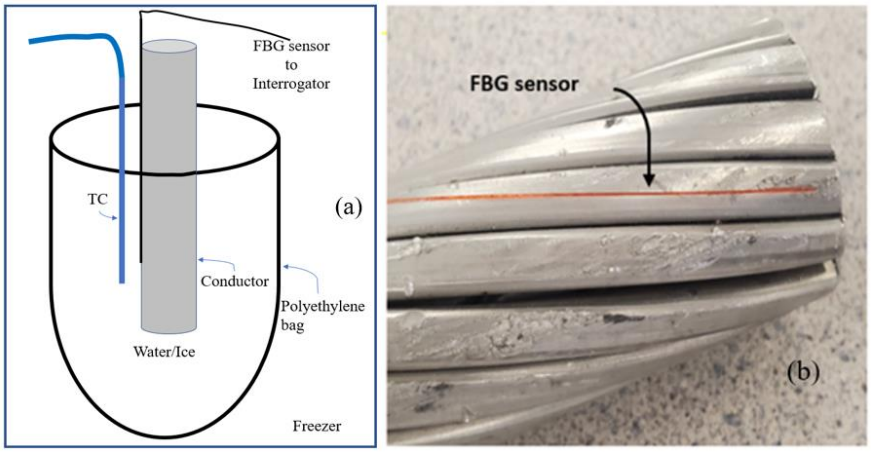

Figure 57: (a) Sketch of experimental setup (b) FBG sensor attached on the conductor

Figure 57b shows the close-up view of the FBG sensor epoxied along the strands of the ACCC. A free-hanging thermocouple inside the freezer measured the temperature of the freezer during the experimental process. The temperature of the freezer was reduced, and the wavelength and the temperature data were recorded every second.

The experimental setup described above is very helpful in understanding the ice accumulation process on the ACCC conductors. However, one major issue with this experimental approach is that this is not the most accurate representation of the real-world ice nucleation process on the conductors. In the real-world environment, ice accumulation on the transmission line is mostly because of freezing rain and the thickness of the ice could be negligible at times. So, the important question is whether the FBG sensor can observe such nuances.

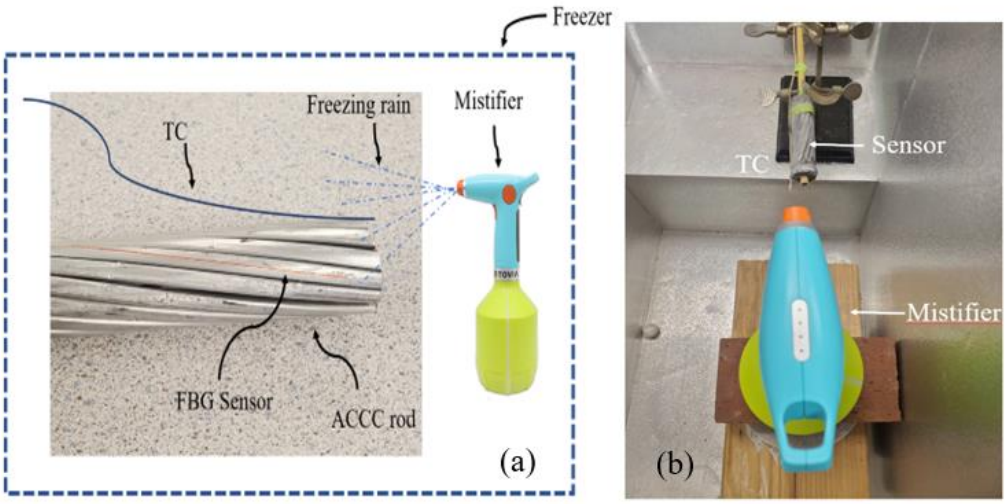

Figure 58: (a) A sketch of an experiment (b) Actual experimental setup of an ACCC conductor subjected to freezing rain

To obtain an answer to this question, another experiment was performed where the FBG sensor epoxied along the strands of the ACCC conductor was put into a freezer and

subjected to simulated freezing rain. The freezing rain environment was attained by spraying freezing water using a TOVIA Electric Mistifier. The sketch of an experiment and an actual experimental setup are shown in Figure 58a, and Figure 58b, respectively.

12.0 Results and Discussions

12.1 Ice crystallization monitoring on FBG sensor

Monitoring of ice crystallization using the FBG sensors was demonstrated already in section 9.1.1. The experimental setup is shown in Figure 46b. It was determined that the FBG sensor could identify the beginning and end of ice crystallization. In addition to crystallization monitoring, the embedded FBG sensor can also determine the axial cooling strain. The shapes of the cooling curves in both ice trials are very similar (Figure 59a, and Figure 59b).

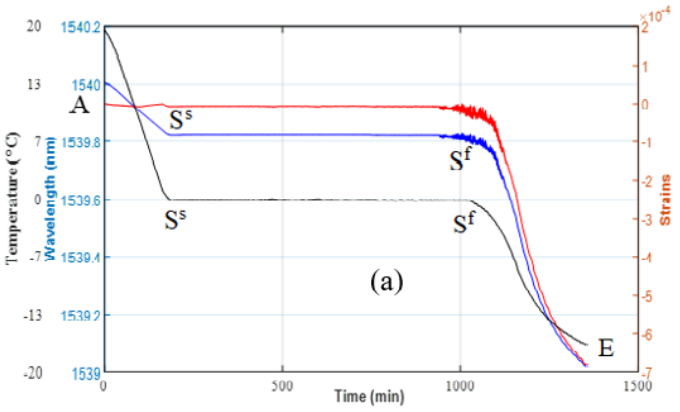

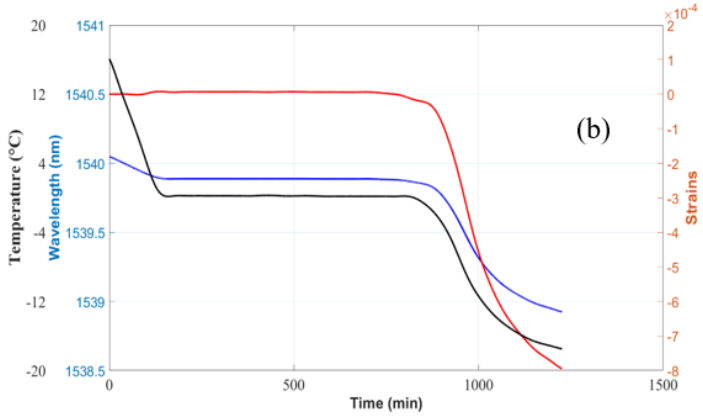

Figure 59: Wavelength, temperature, and axial strain during crystallization and cooling of ice (a) Trial 1, and (b) Trial 2

Table 16 provides a comparison between the experimental and the analytical cooling strains for ice. The measured CTE of ice, varied in the literature from 42e-6/K to 55e-6/K [161], [162], [163]. For the temperature range in this study, the value of 48e-6/K was selected. The estimated cooling strain (ε_e) is then compared with the axial strain calculated including and excluding the radial strain impact (as discussed in section 3.3). It was observed that the axial strain calculated including the radial strain impact is closer to the estimated axial strain ε_e.

Table 16: Comparison of experimental and estimated cooling strains for ice

CTE(e-6/K)	Temperature change (°C)	Estimated cooling strains ($\varepsilon_e=\alpha_m*\Delta T$) (με)	Experimental axial strains (με)	
			Including radial strains	Excluding radial strains
48	-16.0	-768.0	-689.2	-540.0
48	-17.5	-840.0	-794.4	-652.3

12.2 Ice crystallization monitoring on FBG sensor epoxied to the transmission lines

The wavelength and the temperature profiles obtained from the ice crystallization experiment are shown in Figure 60a, and Figure 60b, respectively. The experiment was conducted using the experimental setup shown in Figure 57. It is evident that the FBG sensor was able to measure the super-cooling (A), signifying the beginning of the ice accumulation process. The temperature of the sample increases slightly after A, because of the heat evolved during the freezing process, and then holds constant at 0 ºC as the rest of the water freezes. Point 'B' represents the end of the freezing process. Here, all the water has been converted to ice, and from that point forward the cooling of ice begins. As shown

in Figure 60a, the FBG sensor was able to detect the cooling of ice (B-C), heating of ice (C-D), and ice melting (D) as well.

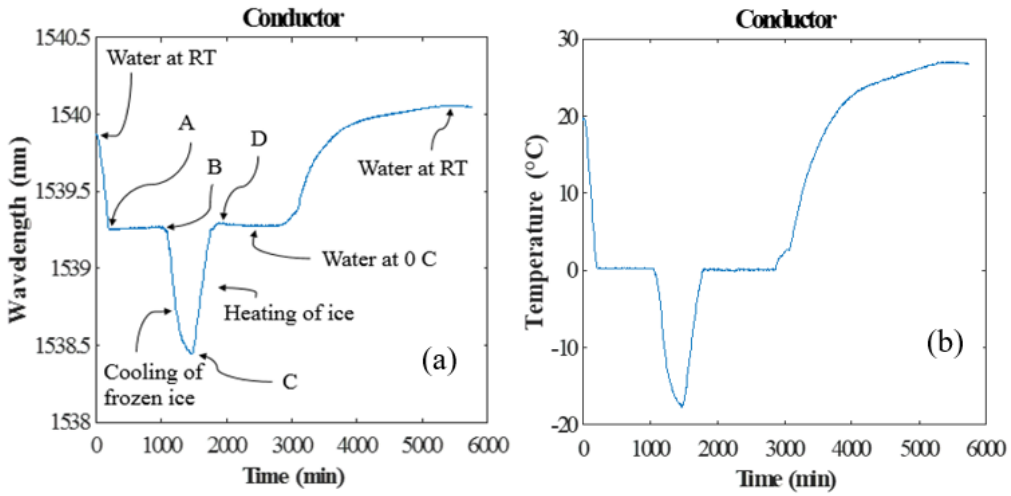

Figure 60: (a) Wavelength and (b) Temperature profile from the sensors (FBG and TC) attached to the conductor

This experiment proves that the FBG sensor epoxied to the surface of the ACCC conductor can identify the beginning and the end of ice formation and the beginning and the end of ice melting. While the thermocouple might also be able to demonstrate the beginning and the end of ice formation on the transmission lines, the use of the FBG sensor provides a further advantage as it can be used to determine the strains/strains on the fiber. Further, with the proper experimental approach, the FBG sensor could measure the volumetric expansion of ice during the crystallization process.

Figure 61 shows the total axial strain on the surface of the conductor obtained from the monitoring of the ice formation on the HV transmission lines. The axial strain profile can be determined as $\varepsilon_{total} = (\Delta\lambda/\lambda - \alpha_\partial \Delta T)/k$. As seen, until point A, the strain measured is

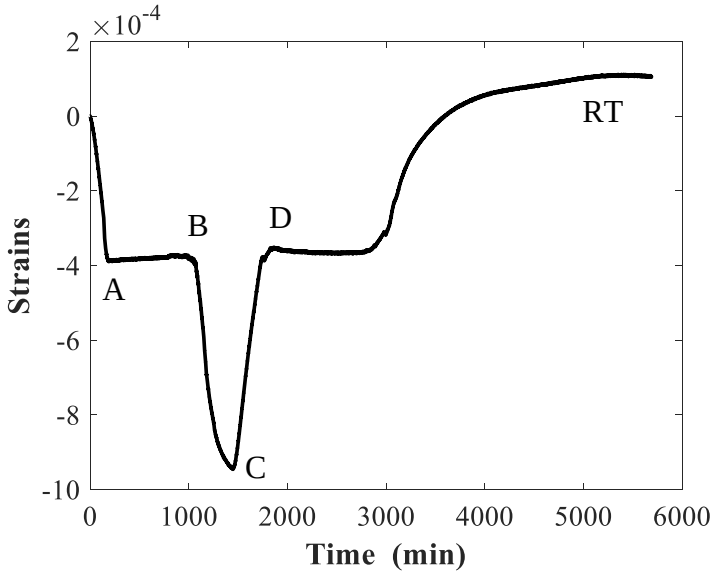

Figure 61: Total axial strain from the FBG monitoring of the ice formation on the ACCC HV transmission lines

due to the thermal contraction of the ACCC conductor. The FBG measured thermal contraction of conductor until point A is -0.000382 which is close to the expected thermal contraction of conductor for a temperature change of -19 ºC i.e., -19*22e-6 = -0.000418. From point B to C, the axial strain is mostly due to the thermal cooling of ice and the conductor rod. The total axial strain between points B and C is -0.000562. This strain is higher than the thermal contraction of the conductor alone (-19*22e-6=-0.000418) and smaller than the thermal contraction of solid ice (-19*48e-6=-0.000912) for the recorded temperature change. As the temperature of the system is increased from point C, the thermal contraction measured by the FBG sensor starts to decrease. Once all the ice is melted, the axial strain on the FBG fiber goes back to the initial thermal contraction (strain at point A) of the conductor before ice formation on it. The spikes observed during the heating portion of the strain curve might be related to the temperature difference between

the thermocouple gauge and the FBG sensor. It could also be due to the timing discrepancy between the FBG and the TC sensors leading to an exaggeration of the compensation issue and resulting in the spikes as seen in the axial strain profile.

12.3 Ice crystallization monitoring on transmission line during freezing rain environment

While the results shown in Figure 60 and Figure 61 proves that the FBG sensor can be used to monitor ice crystallization, however, it is not how ice accumulates on HV transmission lines in the real world. Hence, the freezing rain environment was created using the mistifier. It is a more realistic experimental simulation of the ice accumulation process on the transmission lines. The wavelength and temperature measurements from the freezing rain experiment are shown in Figure 62a, and Figure 62b, respectively. As seen in the figure below, initially, the conductor surface temperature decreases from RT to well below 0 ºC. As the freezing rain begins (A'), the conductor temperature rises a little bit (from A' to A) as the temperature of freezing rain is higher than that of the conductor. The freezing water on the surface of the conductor starts to nucleate at around 0 ºC (A). The nucleation process continues until B. The freezing rain stops at B and the cooling of ice begins. Similar to the previous ice experiment, the FBG sensor was able to detect all the characteristic points associated with ice crystallization including the beginning (A) and the end (B) of the ice nucleation, cooling of ice (B-C), heating of ice (C-D) and melting of ice (D).

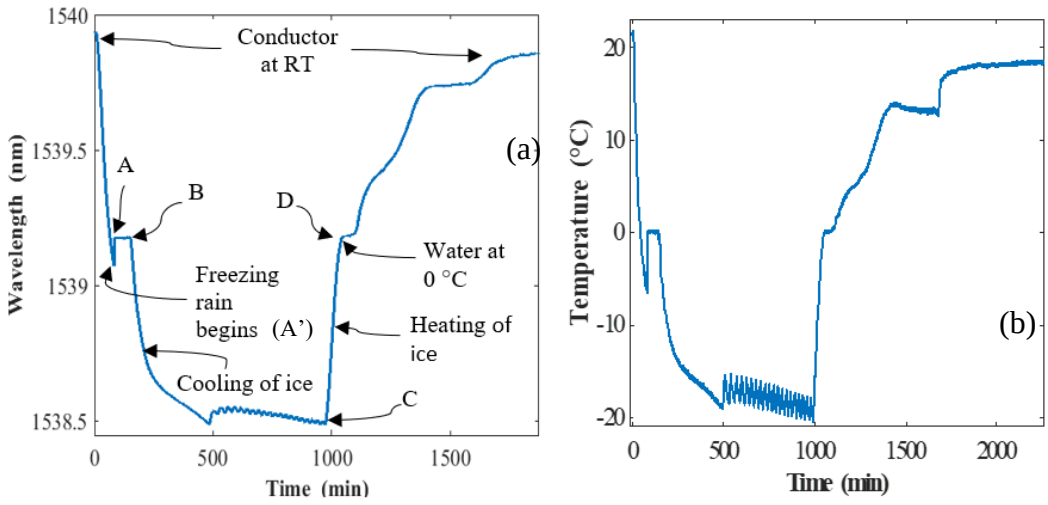

Figure 62: (a) Wavelength and (b) Temperature profile from the sensors (FBG and TC) attached to the conductor subjected to a simulated freezing rain environment

In this section, it was demonstrated that the FBG sensor can monitor the ice crystallization process. By adhering an FBG sensor on the surface of HV conductors, utility companies may be able to identify whether the HV transmission line conductor is still under the ice load or not.

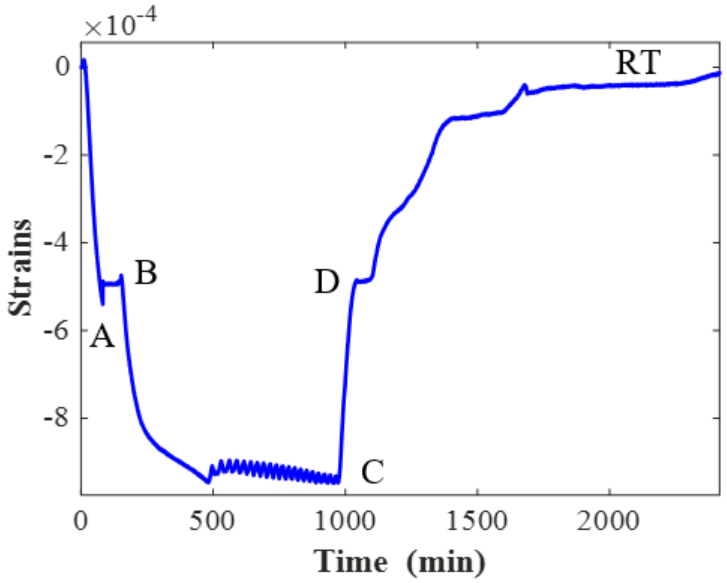

Figure 63: Total axial strain from the FBG monitoring of the ice formation during freezing rain environment on the ACCC conductor

Figure 63 shows the total axial strain on the surface of the conductor subjected to the ice formation due to the freezing rain environment. Similar to Figure 61, the local thermal contraction of the conductor was measured by the FBG sensor until point A. There was no significant change in the strain from point A to point B as the ice was crystallizing on the conductor. From point B to C, the thermal contraction measured in this case is largely due to the conductor itself as the thickness of the ice formed on the surface of the conductor was very small and had negligible influence on the FBG sensor both thermally and mechanically. The thermal contraction measured from the start of the experiment to point A and from point B to point C is comparable to the expected thermal contraction of the ACCC conductor for the given temperature change.

13.0 Proposed Method for Ice Accumulation Measurements (Future Work)

Liang et al [164] proposed an overhead conductor tension sensor based on a fiber Bragg grating sensor. They connected the FBG sensor to an insulator with metallic clamps and treated the FBG sensor as a weighing sensor. The ice accumulation on the transmission line would cause the center FBG wavelength change, and the corresponding strain was calculated.

Li and Zhang [165] proposed a similar system to measure ice thickness. In contrary to connecting the FBG sensor to the insulators [164], they developed a cantilever beam and at the end of the cantilever beam, a simulation transmission line with the same specification of the power line was suspended. By using the cylindrical shape ice model, icing thickness was calculated by the weight sensor wavelength shift. Various other techniques, that rely on a combination of FBG strain sensors and temperature sensors have been developed [166], [167]. In this dissertation, one more potential approach to monitoring the ice accumulation (quantity and thickness of ice) on the transmission lines has been proposed.

13.1 Sensor module definition

As previously discussed in section 2 and section 6, an FBG sensor responds to strain and temperature simultaneously, i.e., the strain measured by the sensor is the sum of mechanical and thermal strains. But to measure the strain on the FBG fiber due to the mass of ice only, the following setup of FBGs (Figure 64) is proposed. In this design, FBG 1

measures the total strain (mechanical + thermal) while FBG 2, encapsulated in a ceramic capillary tube that is not subjected to the mechanical load measures the temperature. So, the peak wavelength shift of FBG 2 is purely due to the thermal effect ($\varepsilon_m = 0$). The wavelength shift of encapsulated (FBG 2) sensor can be subtracted from the strain sensor (FBG 1) to get the temperature compensated local strain on the transmission line caused just by the mass of the ice. This sensor setup is called a module for the purpose of this dissertation.

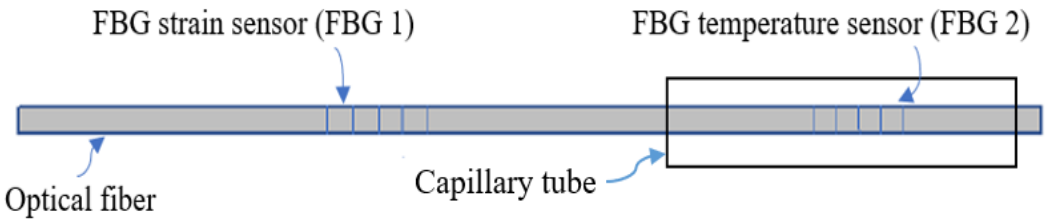

Figure 64: Schematic of an FBG sensor module

The configuration shown in Figure 64 can be embedded or epoxied on the surface of a transmission line to measure the actual axial strain and the temperature during the freezing of ice. The change in the temperature during the freezing process of ice on the structures can be calculated using the reflected wavelength of FBG 2. The equation for determination of temperature change based on the FBG wavelength shift has been previously established in Section 6 (equation 30).

13.2 Calculation of tension in the cable

We know from equation 15:

$$\varepsilon_{res} = \left(\frac{\Delta\lambda}{\lambda} - k\alpha_f \Delta T - \alpha_\partial \Delta T\right)\frac{1}{k} \quad (69)$$

where ε_{res} is the residual strain in the fiber and all the other variables are as defined previously. Therefore, the total strain (ε_m) on the surface of the transmission line measured by an FBG sensor can be given as:

$$\varepsilon_m = \left(\frac{\Delta\lambda}{\lambda} - \alpha_\partial \Delta T\right)\frac{1}{k}$$

Now, from the Hooke's law:

$$\sigma = E\,\varepsilon$$

$$\frac{F}{A} = E\,\varepsilon_m$$

$$F = AE\left(\frac{\Delta\lambda}{\lambda} - \alpha_\partial \Delta T\right)\frac{1}{k} \quad (70)$$

where A is the cross-sectional area, F is the force along the cross-section, and E is the stiffness of the material under consideration. Therefore, the tensions (S_1, S_2, and S_3) measured by the strain sensors of modules 1, 2, and 3 respectively can be given as:

$$S_1 = AE\left(\frac{\Delta\lambda_1}{\lambda_1} - \alpha_\partial \Delta T_1\right)\frac{1}{k} \quad (71)$$

$$S_2 = AE\left(\frac{\Delta\lambda_2}{\lambda_2} - \alpha_\partial \Delta T_2\right)\frac{1}{k} \quad (72)$$

$$S_3 = AE\left(\frac{\Delta\lambda_3}{\lambda_3} - \alpha_\partial \Delta T_3\right)\frac{1}{k} \quad (73)$$

where, λ_1, λ_2, and λ_3 are the base wavelengths of strain sensor in modules 1, 2, and 3, respectively. Similarly, $\Delta\lambda_1$, $\Delta\lambda_2$, and $\Delta\lambda_3$ are the change in associated FBG reflected wavelength because of incremental change in ice accumulation/removal on the surface of the transmission line. Further, ΔT_1, ΔT_2, and ΔT_3 are the changes in the temperature as

measured by the temperature sensors of modules 1, 2, and 3, respectively during the freezing and melting of ice, and the rest of the variables are as defined previously. The tensions represented by S_1, S_2, and S_3 are not to be confused with sag.

13.3 Determination of mass and thickness of ice

For the catenary cable shown below in Figure 65, the tension at the lowest point of the sag will be horizontal. Let us assume the tension at that point be S_2. Similarly, let us assume the tensions near the top of the two support towers be S_1 and S_3 (see Figure 65). Now, the force balance at the location where tension S_1 is acting can be given as:

$$2S_1 = S_2 + m_c g \tag{74}$$

where m_c is the mass of the conductor/unit length and g is the acceleration due to gravity. We know that the horizontal tension component in the catenary cable is always constant, hence: $S_{1x} = S_{3x} = S_2$.

Also, we know that the tensions S_1 and S_3 can be resolved and given as their respective X and Y components. Hence:

$$S_{1x}^2 + S_{1y}^2 = S_1^2$$

$$S_{1y} = (S_1^2 - S_{1x}^2)^{\frac{1}{2}} \tag{75}$$

Similarly,

$$S_{3x}^2 + S_{3y}^2 = S_3^2$$

$$S_{3y} = (S_3^2 - S_{3x}^2)^{\frac{1}{2}} \tag{76}$$

and the force balance in vertical direction gives: $S_{1y} + S_{3y} = Mg$

$$S_{1y} + S_{3y} = Mg \tag{77}$$

where M is the total mass per unit length. i.e., mass of conductor/unit length (m_c) + mass of ice/unit length (m_i).

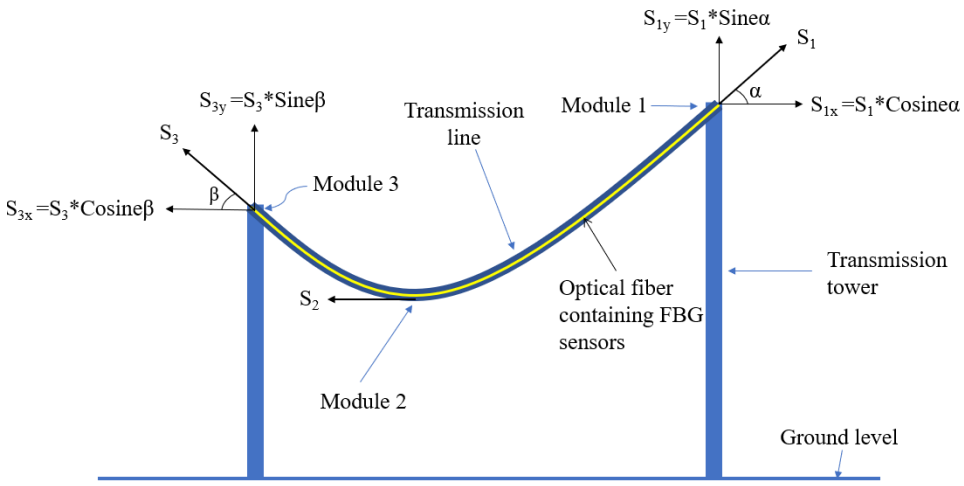

Figure 65: Free body diagram of catenary cable with sensor module setup

Substituting values of S_{1y} and S_{3y} from equation 75 and 76 to 77 we get:

$$(S_1^2 - S_{1x}^2)^{\frac{1}{2}} + (S_3^2 - S_{3x}^2)^{\frac{1}{2}} = (m_c + m_i)g$$

$$(S_1^2 - S_{1x}^2)^{\frac{1}{2}} + (S_3^2 - S_{3x}^2)^{\frac{1}{2}} = [\rho_c \pi r^2 L + \rho_i \pi L\{(r+h)^2 - r^2\}]\, g$$

$$(S_1^2 - S_{1x}^2)^{\frac{1}{2}} + (S_3^2 - S_{3x}^2)^{\frac{1}{2}} = [\rho_c \pi r^2 L + \rho_i \pi L(2rh + h^2)]g \qquad (78)$$

Here, ρ_i and ρ_c are the densities of ice and conductor respectively, h is the thickness of the ice, r is the radius and L is the length of the conductor in consideration. It is assumed that the ice accumulates homogenously along the length and equally all around the conductor.

That means that by adhering three FBG sensor configurations (two near the tower and one at the bottom of the catenary), the axial strains on the transmission lines can be determined, which can be transformed into the tension at that location. Equation 78 tells us

that if we know the tensions near the towers and at the bottom of the catenary then the mass, as well as the thickness of the ice on transmission lines, can be calculated. The approach can be further improved by considering the wind loads that act horizontally and would have an impact on the force acting on the right-hand side of equation 77 and the resultant force between the weight of ice and wind load should be taken into consideration. Further, because of various loads (ice, wind, vibration, etc.) on the transmission line, the lowest point of the sag might move. In that case, the provided mathematical model needs to be modified. Another way to tackles this issue would be by attaching multiple sensor modules near the bottom of the catenary and taking the measurements from the sensor module with the lowest tension.

Conclusions

In this section, a novel monitoring technique to identify the state transition of ice crystallization was proposed. The FBG sensor system was able to identify the beginning and the end of the ice crystallization process. Further, the FBG sensor was also able to measure the cooling strain caused by the ice cooling process. The FBG measured cooling strains were compared with the estimated cooling strains and were found to be nearly equal, demonstrating the accuracy of the experiment and the FBG sensor. The FBG sensors were proved to be effective in monitoring the ice formation and melting on HV transmission lines. Further, an ice accumulation monitoring technique using three FBG sensor modules was also proposed. The mathematical analysis presented above clearly advocates the validity of the design. However, the experimental work was not done for this dissertation and was left for future researchers to pursue. The developed experimental and analytical ice monitoring model can identify the initiation and end of crystallization of ice. This system can measure the temperature, contraction of ice, thickness as well as quantity of ice.

Overall Concluding Remarks

In this dissertation, the application of FBG sensors for monitoring the manufacturing cycle of extreme environment application materials such as epoxies, tin/bismuth alloys, and ice, has been successfully demonstrated. Embedding a single FBG sensor and a thermocouple inside the materials under investigation allowed to measure the strain and temperature simultaneously while the temperature reading was useful to back out the temperature effect on the embedded FBG sensor. Considerable understanding and observation were made about the formation of single fiber composites with various matrix materials.

The analytical, numerical, and experimental results presented in this research demonstrate the need for careful consideration of experimental design when using FBG sensors to monitor extreme environment application materials. The effect of the aspect ratio of the fiber, the Young's modulus and Poisson's ratio of the matrix, and the size (diameter) of the matrix on the Bragg shift, along with the importance of understanding the radial strain impact were evaluated. It was established that the FBG measurements are dependent on the aspect ratio of the fiber. For small aspect ratios, the apparent strains in the FBG fibers do not provide an accurate representation of strain in the materials. It was observed that the aspect ratio should be at least 150 for epoxy, 120 for ice, and 100 for tin/bismuth before the effect of aspect ratio on the FBG measurement starts to converge to an asymptotic value. Similarly, it was demonstrated that, for materials with large stiffnesses

(such as tin/bismuth alloys), the FBG fiber radial strain has a substantial impact on the FBG wavelength shift and, hence, should not be ignored during the axial strain calculation. Therefore, for ice, tin/bismuth alloys, or any other matrix materials with large stiffnesses, the use of the complete formula (equation 2) to estimate the axial strain evolution is strongly recommended. Further, it was demonstrated that the FBG measurement is dependent on the Poisson's ratio of the matrix especially for materials with high stiffnesses. The impact of the ratio of the diameter of the matrix to that of the fiber on the FBG measurements was also investigated. It was observed that the fiber axial strain when using a small matrix diameter might not provide an accurate representation of the strain state of the single fiber composite.

Concluding remarks for epoxy monitoring:

Utilizing the novel heat balance algorithms, other theoretical and experimental techniques developed in this research, significant characteristic points can be determined for the investigated RT and HT epoxies by the embedded thermocouple and the readings of the internal and external FBG sensors. This novel monitoring technique was able to identify many distinctive points related to the curing characteristics of the epoxies. Some of the characteristic points identified were: (i) the gel point, (ii) the start of cure, (iii) the end of cure, (iv) the end of the manufacturing cycle, (v) the start and end of interface degradation, etc. for the epoxies. The convenient approach of using the combined thermocouple/FBG setup with the iterative calculations of the conductivity factors resulted in an extremely accurate estimation of the curing time independently verified by the Flory-

Stockmayer theorem. Without the proper estimation of the heat balance at the end of cure and the heat conductivity factor, the gel point would not be precisely determined and then successfully compared with the Flory-Stockmayer theorem.

The axial strain evolution in the composite during the curing and manufacturing cycle was also monitored for both RT and HT epoxies. Significant scatter in curing and manufacturing strains was observed. This is a very important finding on its own, as the chaotic nature of the curing behavior results in a significant scatter in the temperature distribution within and between the samples leading to the scattering in the curing and the manufacturing strains. Other potential causes for the scatter on the final manufacturing strains during the curing of composites were also presented. An evaluation of the manufacturing strain was also made which is significant in determining the quality and life of the composite parts.

Further, a novel approach to determine residual stresses in the matrix of a single FBG fiber/matrix composite at the end of the manufacturing cycle using the FBG strain measurements was also presented. Using the corresponding residual strains in the fibers and their stiffness properties, the residual axial stresses in the FBG fibers at the end of curing and the end of manufacturing for the RT and HT epoxies were measured. However, determining the matrix stresses is not straightforward as during the manufacturing process of a single fiber composite, the matrix undergoes many complex and often nonlinear transformations. However, the glass FBG fiber responds linear elastically to all the stresses imparted on it during the curing and cooling processes. Using the residual strains in the fiber as the input, the calculation of the residual stresses in the matrix was performed using

an approach that solved for the matrix stresses using equivalent fully linear elastic transformations. The residual total stresses in the matrix of both composite types were found to be close to what could be expected for the epoxy systems investigated in this research, in particular, if compared with their strength values. This validates the theoretical model developed and used in this research.

Moreover, the FBG sensor can be used to monitor not only the manufacturing but also the in-service condition of polymer composites. Aging as well as life cycle monitoring of the epoxies at high temperature was successfully demonstrated. The embedded FBG sensor in a single fiber composite allowed to determine the start and end of the interface degradation between the fiber and the matrix. The early knowledge of the initiation of fiber/matrix degradation could potentially avoid the significant damage that could have occurred by the sudden collapse of a composite part or an entire structure.

Concluding remarks for tin/bismuth monitoring:

The experimental and analytical approach was also presented in this dissertation to demonstrate the application of FBG sensors in monitoring the solidification processes using tin/bismuth alloys as an example. The beginning and the end of the solidification were established either visually using the FBG wavelength curve or by using one of the Heat Balance, Strain, or Linear Regression approaches.

Further, FBG sensors were able to determine all the phase transitions in the alloys. Since FBG sensors are very sensitive to temperature changes and to any small stress state changes, they were able to act in response to all the phase transitions that occur during the

solidification of all the metal alloys investigated in this study. The phase diagram created from the FBG sensor data was compared with that from the TC measurements, and with the literature. The discrepancy between the FBG phase diagram and the TC and literature phase diagrams was small. Hence, it was recognized that under the conditions of these experiments, the FBG sensors are better suited than the thermocouple sensors for the construction of phase diagrams.

Moreover, the FBG sensor also provided valuable information about the strain state of the metals/alloys. The FBG sensor was not significantly impacted by the volumetric expansion and contraction of tin/bismuth during the actual solidification process. The cooling axial strains measured by the FBG sensors during the solidification processes were compared to the numerical cooling strains of the respective alloys starting from the solidus line. The discrepancy between them is very small (<3 %). The strain in the FBG fiber can also be used to calculate the stress in the fiber and the metal matrix. In conclusion, the in situ FBG sensor-based technology could have significant advantages in monitoring the solidification of metal alloys and could become a powerful technique in the field of Materials Science and Engineering.

Concluding remarks for ice monitoring:

Following the experimental approach developed for polymers and alloys in sections 6 through 9, water crystallization was also monitored as it is one of the simplest material systems and enabled a comparison with the alloys that go through a constant temperature phase transformation. It was demonstrated that the FBG based technique was able to

monitor the crystallization process of ice. The axial strain evolution during the crystallization and cooling of ice was also monitored. The cooling strain measured during the ice formation is close to the expected analytical cooling strain. Moreover, the FBG sensors were demonstrated to be effective in monitoring the beginning and end of icing on a certain type of transmission lines. This information could be utilized by the utility companies to take appropriate action to melt the deposited ice from the power lines. Further, a theoretical approach to determine the mass, as well as the thickness of ice on the HV transmission line, was presented in this work.

Critical Final Comment

The proposed FBG-based monitoring technique greatly improves the current capability to (i) measure the DOC of polymers, (ii) determine the residual strains and stresses in the single fiber composites (iii) monitor the in-service composite for the beginning of the degradation, (iv) monitor the strain evolution during solidification, (v) recreate the phase diagram of the alloys, (vi) estimate the stresses in the solidified parts, (vii) monitor the ice crystallization process and potentially use FBG sensors in the ice accumulation in transmission lines, etc. Since the specimen preparation is very straightforward, the proposed method can be routinely practiced, and the measurement can be completely automated. It will provide a much-needed tool for rapid but accurate assessment of extreme environment application materials.

Future work

This dissertation provides a proof of concept that the FBG sensor can be used to monitor the manufacturing of single fiber composites. The knowledge gained from this research can be extended to measure the residual strains and stresses during the manufacturing of multifiber unidirectional or laminated composites. The work can be further refined by embedding the FBG sensor between the plies of the laminate composites to monitor the debonding/crack between the plies during the in-service condition of the composites.

All the measurements in this research were performed in a near constraint-free environment by using a very flexible/non-tractioned mold. Efforts could be made to modify and extend this research to measure the residual stress formation in various manufacturing processes involving different materials, mold shapes, etc., using the difference in strains between a tractioned case and a geometrically simple non-tractioned case. For example: in an additive manufacturing process, a layer-by-layer deposition of materials takes place to form a part, where previously deposited layers have already been solidified and can act as a constraint to the fresh new layer, resulting in residual strains/stresses. Likewise, the approach could be used in casting or extrusion processes. In the case of tin/bismuth alloys and water crystallization, the experimental suggested in this dissertation could only measure the phase change and the axial cooling strains. The experiment could be modified perhaps by adhering the FBG sensor to the surface of the concave mold and monitoring the solidification/crystallization process. This experiment could potentially measure the expansion or contraction of the material during the phase transformation process, thereby

making the FBG sensor more useful in solidification/crystallization monitoring of materials.

References

[1] J. Hoffman, S. Khadka and M. Kumosa, "Determination of Gel Point and Completion of Curing in a Single Fiber/Polymer Composite," *Comp Sci & Tech*, vol. 188, 2020.

[2] S. Khadka, J. Hoffman. and M. Kumosa, "FBG Monitoring of Curing in Single Fiber Polymer Composites," *Comp Sci & Tech.*, vol. 198, 2020.

[3] S. Khadka, J. Hoffman and M. Kumosa, "Residual Stress Measurement in Single Fiber Composite Using FBG Sensor," *Comp Sci & Tech*, 2021.

[4] S. Khadka, J. Hoffman, P. Predecki and M. Kumosa, "Monitoring Solidification of Tin-Bismuth Alloys Using FBG Sensors," *Mat*, vol. 21, 2022.

[5] K. Weraneck, Heilmeier, F., M. Lindner, M. Graf, M. Jakobi, W. Volk, J. Roths and A. Koch, "Strain Measurement in Aluminum Alloy during the Solidification Process Using Embedded Fiber Bragg Gratings," *Sensors (Basel, Switzerland)*, vol. 16, no. 11, p. 1853, 2016.

[6] W. Egner, "Simulation of the Creation of Residual Stresses in Cast Parts," Shaker Verlag Aachen, Germany, 1998.

[7] P. Withers and H. Bhadeshia, "Residual Stress, Part 1 - Measurement Techniques," *Mater. Sci. Tech*, vol. 17, p. 355–365, 2001.

[8] T. M. Hutchings, P. Withers, T. M. Holden and T. Lorentzen, "Introduction to the Characterization of Residual Stress by Neutron Diffraction," *Mater. Characterize.*, vol. 58, pp. 492-499, 2007.

[9] P. Hofer, E. Kaschnitz and P. Schumacher, "Measurement and Simulation of Warpage and Residual Stresses in Die-Cast Parts," *Foundry*, vol. 99, p. 30–41, 2012.

[10] C. Ohms, "Residual Stresses in Thick Bi-metallic Fusion Welds: A Neutron Diffraction Study. Ph.D. Thesis," Delft University of Technology, The Netherlands, 2013.

[11] Z. Zhi and O. Jinping, "Techniques of Temperature Compensation for FBG Strain Sensors Used in Long - Term Structural Monitoring," in *Proceed of Asian Pacific Fndmentl Problm of Opto & Microelectro*, Russia, 2005.

[12] M. Kreuzer, "Strain Measurement with Fiber Bragg Grating Sensors," HBM, Darmstadt, Germany, 2011.

[13] Z. Boming, Y. Zhong and S. Xinyang, "Measurement and Analysis of Residual Stresses in Single Fiber Composite," *Mat & Dsgn*, vol. 31, no. 3, pp. 1237-1241, 2010.

[14] K. Hill, Y. Fujii, D. Johnson and B. Kawasaki, "Photosensitivity in Optical Fiber Waveguides: Application to Reflection Fiber Fabrication," *Appl. Phys. Lett.*, vol. 32, no. 10, p. 647, 1978.

[15] K. Hill and G. Meltz, "Fiber Bragg Grating Technology Fundamentals and Overview," *J. Lightwave Technol.*, vol. 15, no. 8, p. 1263–1267, 1997.

[16] R. Kashyap, Fiber Bragg Gratings, Academic Press, Elsevier, 2009.

[17] Y. Rao, "In-fiber Bragg Grating Sensors," *Mea Sci Tech*, vol. 8, p. 355–375, 1997.

[18] Y. Liu, "Advanced Fiber Gratings and Their Application, Ph.D. Thesis," Aston University, Birmingham, England, 2001.

[19] A. Kersey, M. Davis, H. Patrick, M. LeBlanc and K. Koo, "Fiber Grating Sensors," *J of Lightwave Technology*, vol. 15, no. 8, pp. 1442-1463, 1997.

[20] H. Alemohammad, "Opto Mechanical Modelling of Fiber Bragg Grating Sensors," in *Opto-mechanical Fiber Optic Sensors: Research, Technology, and Applications in Mechanical Sensing*, oxford, United Kingdom, Butterworth-Heinemann: 1st Edition, 2018, p. 358.

[21] D. Waters, J. Hoffman and M. Kumosa, "Monitoring of Overhead Transmission Conductors Subjected to Static and Impact Loads Using FBG Sensors," *IEEE Trans. Instrum. Meas.*, vol. 68, no. 2, pp. 595 - 605, 2018.

[22] J. Hoffman, D. Waters, S. Khadka and M. Kumosa, "Shape Sensing of Polymer Core Composite Electrical Transmission Lines Using FBG Sensors," *IEEE Trans. Instrum. Meas.*, vol. 69, no. 1, p. 249–257, 2019.

[23] H. Kang, D. Kang, C. Hong and C. Kim, "Simultaneous Monitoring of Strain and Temperature During and After Cure of Unsymmetric Composite Laminate Using Fiber Optic Sensors," *Smart Mat Struc,* vol. 12, no. 1, pp. 12-29, 2003.

[24] J. Chen, S. Hoa, C. Jen and H. Wang, "Fiber-Optic and Ultrasonic Measurements for In-Situ Cure Monitoring of Graphite/Epoxy Composite," *J. Compos. Mater.*, vol. 33, no. 1, p. 860–881, 1999.

[25] H. L. Cox, "The Elasticity and Strength of Paper and Other Fibrous Materials," *British Journal of Applied Physics,* vol. 3, no. 1, pp. 72-79, 1952.

[26] J. A. Nairn, "On The Use of Shear-Lag Methods For Analysis of Stress Transfer in Unidirectional Composites," *Mechanics of Materials,* vol. 26, no. 2, pp. 63-80, 1997.

[27] D. Hull and W. Clyne, An Introduction to Composite Materials. Second Edition, London: Cambridge University Press, 1996.

[28] J. Botsis, L. Humbert, F. Colpo and P. Giaccari, "Embedded Fiber Bragg Grating Sensor for Internal Strain Measurements in Polymeric Materials," *Opt & Lasers in Eng.*, vol. 43, no. 3, pp. 491-510, 2005.

[29] D. Karalekas, J. Cugnoni and J. Botsis, "Monitoring of Process Induced Strains in a Single Fibre Composite Using FBG Sensor: A Methodological Study," *Comp A: Appl Sci & Manuf.*, vol. 39, no. 7, pp. 1118-1127, 2008.

[30] P. Parlevliet, H. Bersee and A. Beukers, "Measurement of Post Curing Strain Development With Fibre Bragg Gratings," *Poly Test,* vol. 29, no. 3, p. 291–301, 2010.

[31] X. Shen, "Cure Monitoring of Composites Based on Embedded Fiber Bragg Gratings," *Adv. Mater. Res.*, vol. 211, p. 585–589, 2011.

[32] M. M. Harsch, J. Kocsis and F. Herzog, "Monitoring of Cure-Induced Strain of An Epoxy Resin by Fiber Bragg Grating Sensor," *J. Appl. Poly. Sci.,* vol. 107, pp. 719-725, 2008.

[33] M. Lai, D. Karalekas and J. Botsis, "On the Effect of the Lateral Strains on the FBG Response," *Sensors,* vol. 13, no. 2, pp. 2631-2624, 2013.

[34] J. Eshelby, "The Determination of The Elastic Field of an Ellipsoidal Inclusion, and Related Problems," *Proc. R. Soc. Lond. A,* vol. 241, no. 1226, p. 376–396, 1957.

[35] Z. Hashin and S. Shtrikman, "A Variational Approach to the Theory of the Elastic Behaviour of Multiphase Materials," *J of Mech & Phy of Soli,* vol. 11, no. 2, pp. 127-140, 1963.

[36] J. Barber, Intermediate Mechanics of Materials, Springer, 2010.

[37] D. T. Lawrence, The Interphase in Epoxy Composites, in “Advances in Polymer Science 75-Epoxy Resins and Composites II, Berlin: Springer, 1986, pp. 1-32.

[38] S. R. Bauer, Epoxy Resins, International Encyclopedia of Composites, Vol. 2, New York: VCH Publishers, 1990.

[39] M. Clayton, Epoxy Resins: Chemistry and Technology (Second ed.), CRC Press, p. 65. ISBN 978-1-351-44995-3, 2018.

[40] Curing kinetics of epoxy resins/amine system and epoxy/episulfide resin/amine system.

[41] D. Puglia and M. J. Kenny, Cure Kinetics of Epoxy/Rubber Polymer Blends. In: Parameswaranpillai J., Hameed N., Pionteck J., Woo E. (eds) Handbook of Epoxy Blends., Cham: Springer, 2017.

[42] K. Dušek, "Network formation in curing of epoxy resins. In: Dušek K. (eds) Epoxy Resins and Composites III.," *Advances in Polymer Science,* Vols. 78, Springer, Berlin, Heidelberg., pp. 1-59, 1986.

[43] U. T. Kreibich and R. Schmid, "Inhomogeneities in epoxy resin networks," *J of Poly Sci: Poly Symposia,* vol. 53, no. 1, pp. 177-185, 1975.

[44] J. Gillham, "Characterization of Thermosetting Materials by Torsional Braid Analysis," *Poly Engg & Sci,* vol. 16, no. 5, pp. 353-356, 1976.

[45] "Influence of Crosslinking on the Mechanical Properties of High Tg Polymers," Air Force Materials Laboratory - Materials Research Center, Lehigh University, Bethlehem, Pennsylvania, 1976.

[46] S. S. Hwang, S. Y. Park, G. C. Kwon and W. J. Choi, "Cure Kinetics and Viscosity Modeling for the Optimization of Cure Cycles in A Vacuum-Bag-Only Prepreg Process," *Int J Adv Manuf Tech,* vol. 99, p. 2743–2753, 2018.

[47] D. Dolkun, W. Zhu, Q. Xu and Y. Ke, "Optimization of Cure Profile for Thick Composite Parts Based on Finite Element Analysis and Genetic Algorithm," *J. Compos. Mater,* vol. 52, p. 3885–3894, 2018.

[48] J. L. Massingill and R. S. Baur, Epoxy Resins, App Poly Sci: 21st Century, Elsevier Science, 2000.

[49] P. Parlevliet, H. Bersee and A. Beukers, "Residual Stresses in Thermoplastic Composites – A Study of The Literature - Part III: Effect of Thermal Residual Stresses," *Comp Part A:,* vol. 38, no. 6, pp. 1581-1596, 2007.

[50] H. Sarrazin, B. Kim, S. H. Ahn and G. S. Springer, "Effects of Processing Temperature and Lay-Up on Springback," *J of Comp Mat,* vol. 29, no. 10, pp. 1278-1294, 1995.

[51] T. Kamon and H. Furukawa, "Curing Mechanisms and Mechanical Properties of Cured Epoxy Resins. In: Dušek K. Epoxy Resins & Composites IV.," in *Adv in Poly Sci,* vol. 80, Berlin, Springer, 1986, pp. 173-202.

[52] D. Kevin and P. Beaumont, "The Measurement and Prediction of Residual Stresses in Carbon-Fibre/Polymer Composites," *Composite Science and Technology,* vol. 57, no. 11, pp. 1445-1455, 1997.

[53] K. L. Powell, P. A. Smith and J. A. Yeomans, "Aspects of Residual Thermal Stresses in Continuous Fiber Reinforced Ceramic Matrix Composites," *Comp Sci and Tech,* vol. 47, no. 4, pp. 359-367, 1993.

[54] P. R. Wilson, A. F. Cinar, M. Mostafavi and &. J. Meredith, "Temperature Driven Failure of Carbon Epoxy Composites - A Quantitative Full-Field Study," *Comp Sci & Tech,* vol. 155, pp. 33-40, 2018.

[55] A. Pizzi and K. Mittal, Principles of Polymer Networking and Gel Theory in Thermosetting Adhesive Formulations, in: Handb. Adhes. Technol. Revis. Expand, CRC Press, 2010.

[56] A. Patel, O. Kravchenko and Z. I. Manas, "Effect of Curing Rate on the Microstructure and Macroscopic Properties of Epoxy Fiberglass Composites," *Polymers (Basel),* vol. 10, no. 2, p. 125, 2018.

[57] A. J. García-Manrique, B. Marí, G. A. Ribes, L. Monreal, R. Teruel, L. Gascón, J. Sans and &. M. J. Guaita, "Study of the Degree of Cure through Thermal Analysis and Raman Spectroscopy in Composite-Forming Processes," *Materials (Basel),* vol. 12, no. 23, pp. 3991-3999, 2019.

[58] G. K. Bang, W. J. Kwon, G. D. Lee and W. J. Lee, "Measurement of The Degree of Cure f Glass Fiber-Epoxy Composites Using Dielectrometry," *J of Mat Proces Tech,* vol. 113, no. 1, pp. 209-214, 2001.

[59] M. Rudolph, M. Stockmann, R. Landgraf and J. Ihlemann, "Experimental Determination and Modelling of Volume Shrinkage in Curing Thermosets," *Condensed Matter – Material Science,* 2014.

[60] C. K. Short, "Characterization of Epoxy Resins for use in the Resin Transfer Molding Process, Dissertations, Theses, and Master's Projects," College of William & Mary - Arts & Sciences, Williamsburg, Virginia, 1993.

[61] Composite Knowledge Network, "Degree of cure - A104," [Online]. Available: https://compositeskn.org/KPC/A104. [Accessed 10 12 2021].

[62] P. J. Flory, "Molecular Size Distribution in Three Dimensional Polymers. I. Gelation," *J of the Am Chem Soc*, vol. 63, no. 11, pp. 3083-3090, 1941.

[63] W. H. Stockmayer, "Theory of Molecular Size Distribution and Gel Formation in Branched Polymers II. General Cross Linking," *J. Chem. Phys.*, vol. 12, pp. 125-131, 1944.

[64] N. Sbirrazzuoli, S. Vyazovkin, A. Mititelu, C. Sladic and L. Vincent, "A Study of Epoxy-Amine Cure Kinetics by Combining Isoconversional Analysis with Temperature Modulated DSC and Dynamic Rheometry," *Macro Molec Chem and Phy*, vol. 204, no. 15, pp. 1815-1821, 2003.

[65] N. Sbirrazzuoli and S. V. S, "Learning About Epoxy Cure Mechanisms From Isoconversional Analysis of DSC Data," *Therm Acta*, vol. 388, pp. 289-298, 2002.

[66] H. Flammersheim and J. R. Opfermann, "Investigation of Epoxide Curing Reactions by Differential Scanning Calorimetry – Formal Kinetic Evaluation," *Macromolecular Chem & Phy*, vol. 286, no. 3, pp. 143-150,, 2001.

[67] P. Badrinarayanan, Y. Lu, R. C. Larock and M. R. Kessler, "Cure Characterization of Soybean Oil-Styrene-Divinylbenzene Thermosetting Copolymers," *J of Appl Poly Sci*, vol. 113, pp. 1042-1049, 2009.

[68] D. Abraham and R. McIlhagger, "Glass Fiber Epoxy Composite Cure Monitoring Using Parallel Plate Dielectric Analysis in Comparison with Thermal and Mechanical Testing Techniques," *Comp Part A: App Sci and Manuf*, vol. 29, pp. 811-819, 1998.

[69] A. McIlhagger, D. Brown and B. Hill, "The Development of a Dielectric System for the On-line Cure Monitoring of the Resin Transfer Molding Process," *Comp Part A*, vol. 31, no. 12, pp. 1373-1381, 2000.

[70] H. G. Kim and D. G. Lee, " Dielectric cure monitoring for glass/polyester prepreg composites," *Composite Structures*, vol. 57, no. 1-4, pp. 91-99, 2002.

[71] K. G. Bang, J. W. Kwon, D. G. Lee and J. W. Lee, "Measurement of The Degree of Cure of Glass Fiber-Epoxy Composites Using Dielectrometry," *J of Mat Proces Tech,* vol. 113, no. 1-3, pp. 209-214, 2001.

[72] X. Sheng, M. Akinc and M. R. Kessler, "Cure Kinetics of Thermosetting Bisphenol E Cyanate Ester," *J. Therm Anal & Calori,* vol. 93, pp. 77-85, 2008.

[73] "System 1000 Laminating Epoxy Resin," Fiber Glast Developments Corp, 2018.

[74] "Duralco 4460-600 °F Low Viscosity Epoxy," Cotronics Corp, 2019.

[75] S. R. White and H. T. Hahn, "Process Modeling of Composite Materials: Residual Stress Development During Cure. Part II. Experimental Validation," *J. of Comp Mat.,* vol. 26, pp. 2423-2432, 1992.

[76] Y. K. Kim and S. R. White, "Stress Relaxation Behavior of 3501-6 Epoxy Resin During Cure," *Polymer Eng. Sci.,* vol. 36, no. 23, pp. 2852-2862, 1996.

[77] N. K. Asamoah and W. G. Wood, "Thermal Self-Straining of Fiber Reinforced Materials," *J of Strain Analy,* vol. 5, no. 2, pp. 88-97, 1970.

[78] D. Landro and M. Pegoraro, "Evaluation of Residual Stresses and Adhesion in Polymer Composites," *Comp Part A: App Sci & Manuf,* vol. 27, no. 9, pp. 847-853, 1996.

[79] G. S. Bennett, "PhD Thesis," University of Massachusetts, Amherst, 1992.

[80] M. Shokrieh, Residual Stresses in Composite Materials, Second Edition, Woodhead Publishing, 2021.

[81] M. Mehdikhani, L. Gorbatikh, I. Verpoest and S. Lomov, "Voids in Fiber-Reinforced Polymer Composites: A Review on Their Formation, Characteristics, And Effects on Mechanical Performance," *J of Comp Mat,* vol. 53, no. 12, pp. 1579-1669, 2019.

[82] H. Deve and M. Maloney, "On the Toughening of Inter-Metallics With Ductile Fibers-Role of Interfaces," *Acta Mat,* vol. 39, no. 10, pp. 2275-2284, 1991.

[83] T. Nakamura and S. Suresh, "Effects of Thermal Residual Stresses and Fiber Packing on Deformation of Metal Matrix Composites," *Acta Metall Mat,* vol. 41, no. 6, pp. 1665-1681, 1993.

[84] R. Nath, D. Fenner and C. Galiotis, "The Progressional Approach to Interfacial Failure in Carbon Reinforced Composites: Elasto-plastic Finite Element Modeling of Interface Cracks," *Comp: Part A,* vol. 31, no. 9, pp. 929 - 943, 2000.

[85] P. Parlevliet, E. Bersee and A. Beukers, "Residual Stresses in Thermoplastic Composites – A Study of the Literature, Part I: Formation of Residual Stresses," *Comp Part A,* vol. 37, no. 11, p. 1847 – 1857, 2006.

[86] P. Parlevliet, E. Bersee and A. Beukers, "Residual Stresses in Thermoplastic Composites - A Study of the Literature, Part III: Effects of Thermal Residual Stresses," *Comp Part A,* vol. 38, no. 6, p. 1581 – 1596, 2007.

[87] W. Cheng and I. Finnie, Residual Stress Measurement and the Slitting Method, New York: Springer, 2007.

[88] F. Colpo, "Residual Stress Characterization in a Single Fiber Composite Specimen by Using FBG Sensor and the OLCR Technique, PhD Thesis," École Polytechnique Fédérale De Lausanne, Lausanne, 2006.

[89] R. Gibson, Principles of Composite Material Mechanics, New York: McGraw-Hill, 1994.

[90] M. Prime, "Residual Stress Measurement by Successive Extension of A Slot: The Crack Compliance Method," *App Mech Rev,* vol. 52, no. 2, p. 75 – 96, 1999.

[91] R. Reid, "The Measurement of Longitudinal Residual Stresses in Unidirectional Glass Fiber Reinforced Plastic, PhD Thesis," University of the Witwatersrand, Johannesburg, 2009.

[92] R. Reid and R. Paskaramoorthy, "A Novel Method to Measure Residual Stresses in Unidirectional GFRP," *Com Struc,* vol. 88, no. 3, pp. 388-93, 2009.

[93] P. Kulkarni, D. Mali and S. Singh, "An Overview of The Formation of Fiber Waviness and Its Effect on The Mechanical Performance of Fiber Reinforced Polymer Composites," *Comp Part A: App Sci & Manuf,* vol. 137, pp. 106-113, 2020.

[94] K. Stamatopoulos, "Measurement of Residual Stresses on Composite Materials with the Incremental Hole Drilling Method, Diploma Thesis," National Technical University of Athens, School of Naval Architecture and Marine Engineering, Athens, 2011.

[95] H. Y. Liu, X. Zhang, Y. Mai and X. Diao, "On Steady- State Fiber Pull Out, Part II: Computer Simulation," *Comp Sci & Tech,* vol. 59, no. 15, pp. 2191 - 2199, 1999.

[96] D. Lu, Handbook of Measurement of Residual Stresses, Lilburn, GA: The Fairmont Press Inc. , 1996.

[97] M. Seif and S. Short, "Determination of Residual Stresses in Thin-Walled Composite Cylinders," *Exp Tech,* vol. 26, no. 2, pp. 43-46, 2002.

[98] G. Schajer, "Measurement of Non- uniform Residual - Stresses Using the Hole Drilling Method. Part I: Stress Calculation Procedures," *J of Eng Mat & Techn, Trans ASME,* vol. 110, no. 4, pp. 338 - 343, 1988.

[99] G. Schajer and L. Yang, "Residual- Stress Measurement in Orthotropic Materials Using the Hole- Drilling Method," *Exp Mech,* vol. 34, no. 4, p. 324 – 333, 1994.

[100] J. Lee, R. Czarnek and Y. Guo, "Interferometric Study of Residual Strains in Thick Composites," in *Proceedings of the 1989 SEM Conference on Experimental Mechanics*, Cambridge, MA, 1989.

[101] S. Lee and R. Schile, "Investigation of Material Variables of Epoxy Resins Controlling Transverse Cracking in Composites," *J of Mat Sci,* vol. 17, no. 7, p. 2095 – 2106, 1982.

[102] H. Gascoigne, "Residual Surface Stresses in Laminated Cross-Ply Fiber - Epoxy Composite Materials," *Exp Mech*, vol. 34, no. 1, p. 27 – 36, 1994.

[103] P. Sunderland, W. Yu and J. Manson, "A Technique for The Measurement of Process- Induced Internal Stresses in Polymers and Polymer Composites," *Proceedings of ICCM-10, Whistler, BC, Canada,* vol. 3, pp. 125 - 132, 1995.

[104] J. Manson and J. Seferis, "Process Simulated Laminate (PSL), A Methodology to Internal Stress Characterization in Advanced Composite Materials," *J Comp Mat,* vol. 26, no. 3, pp. 405 - 31, 1992.

[105] A. Kalton, S. Howard, R. Janczak and T. Clyne, "Measurement of Interfacial Fracture Energy by Single Fiber Push- Out Testing and Its Application to The Titanium- Silicon Carbide System," *Acta Materialia,* vol. 46, no. 9, pp. 3175 - 31 89, 1998.

[106] J. Lu and D. Retraint, "Review of Recent Developments and Applications in the Field of X-ray Diffraction for Residual Stress Studies," *J of Strain Analysis for Eng Dsgn,* vol. 33, no. 2, pp. 127 - 136, 1998.

[107] B.N.Cox, M. James, D. Marshall and R. Addison, "Determination of Residual Stresses in Thin Sheet Titanium Aluminide Composites," *Metall Trans A (Phy Metall and Mat Sci),,* vol. 21, no. A, p. 2701 – 2707, 2019.

[108] B. Benedikt, M. Kumosa, P. Predecki, L. Kumosa and J. Sutter, "An Analysis of Residual Stresses in a Unidirectional Graphite/PMR-15 Composite Based on the X-ray Diffraction Measurements," *Comp Sci & Tech*, vol. 61, no. 14, pp. 1977-1994, 2001.

[109] B. Benedikt, M. Gentz, L. Kumosa, P. Rupnowski, J. Sutter and M. Kumosa, "X-ray Diffraction Experiments on Aged Graphite Fiber/Polyimide Composites with Embedded Aluminum Inclusions," *Comp Part A,* vol. 35, no. 6, pp. 667-681, 2004.

[110] B. Benedikt, M. K. M and P. Predecki, "An Evaluation of Residual Stresses in Graphite/PMR-15 Composites by X-ray Diffraction," *Acta Mat,* vol. 53, no. 17, pp. 4531-4543, 2005.

[111] P. Rangaswamy, M. Prime, M. Daymond, M. Bourke and B. Clausen, "Comparison of Residual Strains Measured by X-ray, and Neutron Diffraction in a Titanium (Ti–6Al–4V) Matrix Composite," *Mat Sci & Engg,* vol. A, no. 259, pp. 209 - 219, 1999.

[112] D. Kevin and P. Beaumont, "The Measurement and Prediction of Residual Stresses in Carbon-Fibre/Polymer Composites," *Comp Sci & Tech.,* vol. 57, no. 11, pp. 1445-1455, 1997.

[113] S. White and Y. Kim, "Process-Induced Residual Stress Analysis of As4/3501-6 Composite Material," *Mech of Comp Mat & Struct,* vol. 5, no. 2, pp. 153-186, 1998.

[114] P. Parlevliet, H. Bersee and A. Beukers, "Residual Stresses in Thermoplastic Composites - A Study of The Literature - Part III: Effect of Thermal Residual Stresses," *Comp Part A,* vol. 38, no. 6, pp. 1581-1596, 2007.

[115] C. Lawrence, D. Nelson, T. Bennett and J. Spingarn, "An Embedded Fiber Optic Sensor Method for Determining Residual Stresses in Fiber-Reinforced Composite Materials," *J Intel Mat Sys Struc,* vol. 9, no. 10, p. 788–799, 1998.

[116] Y. Wang, B. Han, D. Kim and A. Bar-Cohen, "Joseph P., Integrated Measurement Technique for Curing Process-Dependent Mechanical Properties of Polymeric Materials Using Fiber Bragg Grating," *Exp Mech,* vol. 48, no. 1, p. 107–117, 2008.

[117] Y. Wang and B. Han, "Simultaneous Measurement of Effective Chemical Shrinkage and Modulus Evolutions During Polymerization," *Exp Mech,* vol. 51, no. 7, p. 1155–1169, 2011.

[118] Y. Sun, H. Lee and B. Han, "Measurement of Elastic Properties of Epoxy Molding Compound by Single Cylindrical Configuration with Embedded Fiber Bragg Grating Sensor," *Exp Mech,* vol. 57, no. 2, p. 313–324, 2017.

[119] H. Kishan, Differential Calculus, New Delhi: Atlantic Publishers & Distributors, 2007.

[120] J. Middleton, J. Hoffman, B. Burks, P. Predecki and M. Kumosa, "Aging of a Polymer Core Composite Conductor: Mechanical Properties and Residual Stresses," *Comp Part A,* vol. 69, pp. 159-167, 2015.

[121] J. Middleton, "Aging of a Polymer Core Composite Conductor Under Combined Ozone and Temperature Conditions, PhD Dissertation," University of Denver, Denver, 2015.

[122] J. Hoffman, J. Middleton and M. Kumosa, "Effect of a Surface Coating on Flexural Performance of Thermally Aged Hybrid Glass/Carbon Epoxy Composite Rods," *Comp Sci & Tech,* vol. 106, pp. 141-148, 2014.

[123] R. Jones, N. Yeow and J. McClelland, "Monitoring Ambient-Temperature Aging of A Carbon-Fiber/Epoxy Composite Prepreg with Photoacoustic Spectroscopy," *Composites Part A: App Sci and Manuf,* vol. 39, no. 6, pp. 965-971, 2008.

[124] G. B. A. Odegard, "Physical Aging of Epoxy Polymers and Their Composites," *Polymer Physics,* vol. 49, no. 24, pp. 1695-1716, 2011.

[125] M. M. Hansen and K. Anderko, Constitution of Binary Alloys, New York: McGraw-Hill, 1959.

[126] B. Chalmers, Principles of Solidification, New York: Wiley, 1970.

[127] E. Drits, Properties of Elements, Moscow: Metallurgiya, 1985.

[128] I. Minkoff, Solidification/Liquid State Processes. In: Materials Processes, Berlin, Heidelberg: Springer, 1992.

[129] L. Chatelier, *Phys. Chem. 1,* p. 396, 1887.

[130] F. Giamei and G. Tschinkel, "Liquid Metal Cooling: A New Solidification Technique," *Metall Trans A,* vol. 7A, 1976.

[131] E. Chidiac, K. Brimacombe and V. Samarasekera, "A New Transient Method for Analysis of Solidification in the Continuous Casting of Metals," *App Sci Rsrch.,* vol. 51, pp. 573-597, 1993, 1993.

[132] D. Stefanescu, "Thermal Analysis - Theory and Applications in Metal Casting," *Int. J. of Metal Cast.,* vol. 9, pp. 7-22, 2015.

[133] P. René, P. Miroslav and C. Maria, "Monitoring of Solidification in the Continuous Casting Mold by Temperature Sensors," in *AIP Conference Proceedings 1745, 020048,* 2016.

[134] J. Barlow and D. Stefanescu, "Computer-Aided Cooling Curve Analysis Revisited," *Trans of Amer Foundrymen's Soc,* vol. 106, pp. 349-354, 1998.

[135] H. Cruz, "Quantification of the Microconstituents Formed During Solidification by the Newton Thermal Analysis Method," *J of Mat Process Tech.,* vol. 178, pp. 128-134, 2006.

[136] J. Gibbs and F. Patricio, "Solid Fraction Measurement Using Equation Based Cooling Curve Analysis," *Scrip Mat,* vol. 58, no. 8, pp. 699-702, 2008.

[137] J. Xu, "Comparison of Baseline Method and DSC Measurement for Determining Phase Fractions," *Mat Sci Tech,* vol. 28, no. 12, pp. 1420-1425, 2012.

[138] A. Kamyabi and F. Patricio, "The Evolution of the Fraction of Individual Phases During a Simultaneous Multiphase Transformation from Time-Temperature Data," *Metall & Mat Trans A,* vol. 46, no. 2, pp. 622-638, 2015.

[139] E. Fras, "A New Concept in Thermal Analysis of Castings," *Trans of Ameri Foundrymen's Soc,* vol. 101, pp. 505-511, 1993.

[140] L. Ma, S. Spagnul and M. Soleimani, "Metal Solidification Imaging Process by Magnetic Induction Tomography," *Sci Rep,* vol. 7, p. 14502, 2017.

[141] Z. Fengfeng, T. Ting, J. Seunghwan, K. Garam, C. Patrick and B. Martin, "In-Situ Monitoring of Solidification Process of PVA Solution by Fiber Optic Sensor Technique," *IEEE Sensors,* vol. 21, no. 5, pp. 6170 - 6178, 2021.

[142] "Application of Phase Diagrams in Metallurgy and Ceramics," US Bureau of Standards, 1977.

[143] V. Aleksandrov and A. Barannikov, "Construction of Bi-Sb and Sn-Bi Phase Diagrams with Pre-solidification Supercooling," *Russ. Metall.,* vol. 5, pp. 485-491, 2002.

[144] J. Zhao, Methods for Phase Diagram Determination, Elsevier, 2007.

[145] W. W. Oelsen and K. F. Golucke, "Thermodynamic Analysis - Calorimetry and Thermodynamics of Bismuth-Tin Alloys," *Arch. Eisenhüttenw,* vol. 29, no. 11, pp. 689-698, 1958.

[146] T. Osmo, N. Jaana and T. Pekka, "An Assessment of the Thermodynamic Properties and Phase Diagram of the System Bi-Cu," *Thermochimica Acta*, vol. 173, pp. 137-150, 1990.

[147] H. Okamoto, "Bismuth-Tin," *J Phase Equi Diff,* vol. 31, no. 205, 2010.

[148] V. Aleksandrov, S. Frolova and A. P. A.P. Zozulya, "Solidification of the Eutectic Sn-43 mol % Bi Alloy," *Russ. Metall.,* vol. 7, pp. 612-616, 2017.

[149] E. Mura and Y. Ding, "Nucleation of Melt: From Fundamentals to Dispersed Systems," *Adv in Colloid & Interface Sci,* vol. 289, 2021.

[150] Y. Dutchak, P. Osipenko and V. Panasyuk, "Thermal Conductivity Of Sn-Bi Alloys In The Solid And Liquid States," *Izvestiya vuz, Fizika,* vol. 11, no. 10, pp. 154-156, 1968.

[151] C. Rivera, A. Villeda and M. Argáez, "Cooling Curve Analysis Method using a Simplified Energy Balance," in *ESTEC Conference Proceedings, 6th Engineering, Science and Technology Conference* , Panama, 2017.

[152] E. Fras, W. Kapturkiewicz, A. Burbielko and H. Lopez, "A New Concept in Thermal Analysis of Castings," *AFS Transction,* vol. 4, pp. 505-511, 1993.

[153] Z. Hashin and S. Shtrikman, "A Variational Approach to the Theory of the Elastic Behaviour of Multiphase Materials," *Journal of Mechanics and Physics of Solids,* , vol. 11, no. 2, pp. 127-140, 1963.

[154] D. Ehrenburg, "Transmission Line Catenary Calculations," in *AIEE Paper, Committee on Power Trans & Distribution,* July 1935.

[155] "Graphic Method for Sag Tension Calculations for ACSR and Other Conductors," Aluminum Company of America, 1961.

[156] A. Window, "Strain Gauge Technology," Measurements Group UK Ltd, Elsevier Science Publishers Ltd, 1998.

[157] D. Fink and H. Beaty, Standard Handbook for Electrical Engineers, 13th ed., McGraw-Hill.

[158] A. Sutton, J. J. Orteu and W. Hubert, "Image Correlation for Shape, Motion and Deformation Measurements," Springer, New York, 2009.

[159] A. R. Solangi, "Icing Effects on Power Lines and Anti-icing and," Department of Safety and Engineering, The Artic University of Norway, Norway, 2018.

[160] "Engineers, IEEE Standard for Calculating the Current-Temperature Relationship of Bare Overhead Conductors," Institute of Electrical and Electronics; Transmission and Distribution Committee of the IEEE Power and Energy Society, New York, 2013.

[161] R. Powell, "Preliminary Measurements of the Thermal Conductivity and Expansion of Ice," *Proc. R. Soc. Lond.,* vol. A247, pp. 464-466, 1958.

[162] J. Johnson and R. Metzner, "Thermal Expansion Coefficients For Sea Ice," *Journal of Glaciology,* vol. 36, no. 124, pp. 343-349, 1990.

[163] A. Marchenko, B. Lishman, D. Wrangborg and T. Thiel, "Thermal Expansion Measurements In Fresh And Saline Ice Using Fiber Optic Strain Gauges And Multi-Point Temperature Sensors Based On Bragg Gratings," *J of Sensors,* vol. p. 5678193, 2016.

[164] S. Liang, H. Yang and X. Miao, "An Overhead Conductor Weighing Sensor Based on Fiber Bragg Grating," *Applied Mechanics and Materials* , vol. 462, no. 3, pp. 32-38, 2014.

[165] Z. Li, Z. Zhang and L. Li, "A Novel FBG-Based Sensor System for the Transmission Line Icing On-line Monitor," in *Asia Communications and Photonics Conferene (ACP)*, Wuhan, 2016.

[166] M. Gouming and C. Li, "Ice Monitoring on Overhead Transmission Lines with FBG Tension Sensor," in *Asia-Pacific Power and Energy Engineering Conference*, 2010.

[167] M. Gouming, C. Li and J. Quan, "A Fiber Bragg Grating Tension and Tilt SensorApplied to Icing Monitoring on OverheadTransmission Lines," *IEEE Transactions on Power Delivery*, vol. 26, no. 4, pp. 2163-2170, 2011.

[168] M. Gouming, C. Li and J. Quan, "A Fiber Bragg Grating Tension and Tilt Sensor Applied to Icing Monitoring on Overhead Transmission Lines," *IEEE Transactions on Power Delivery*, vol. 26, no. 4, pp. 2163-2170, 2011.